

UNCLASSIFIED

SECURITY CLASSIFICATION OF THIS PAGE

REPORT DOCUMENTATION PAGE

Form Approved
OMB No. 0704-0188

1a. REPORT SECURITY CLASSIFICATION UNCLASSIFIED			1b. RESTRICTIVE MARKINGS			
2a. SECURITY CLASSIFICATION AUTHORITY			3. DISTRIBUTION/AVAILABILITY OF REPORT Approved for Public Release; Distribution Unlimited			
2b. DECLASSIFICATION/DOWNGRADING SCHEDULE			4. PERFORMING ORGANIZATION REPORT NUMBER(S)			
4. PERFORMING ORGANIZATION REPORT NUMBER(S)			5. MONITORING ORGANIZATION REPORT NUMBER(S) AFOSR-TR. 89-0097			
6a. NAME OF PERFORMING ORGANIZATION Univ. of Calif., Los Angeles Civil Engineering Department		6b. OFFICE SYMBOL (if applicable)		7a. NAME OF MONITORING ORGANIZATION AFOSR/NA		
6c. ADDRESS (City, State, and ZIP Code) 405 Hilgard Avenue Los Angeles, CA 90024-1593			7b. ADDRESS (City, State, and ZIP Code) Bldg. 410 Bolling AFB, DC 20332-6448			
8a. NAME OF FUNDING/SPONSORING ORGANIZATION AFOSR		8b. OFFICE SYMBOL (if applicable) NA		9. PROCUREMENT INSTRUMENT IDENTIFICATION NUMBER AFOSR-86-0290		
8c. ADDRESS (City, State, and ZIP Code) Bldg. 410 Bolling AFB, DC 20332-6448			10. SOURCE OF FUNDING NUMBERS			
			PROGRAM ELEMENT NO. 6.1102F	PROJECT NO. 2302	TASK NO. C1	WORK UNIT ACCESSION NO.
11. TITLE (Include Security Classification) (U) "Micromechanical Behavior of Frictional Geologic Materials"						
12. PERSONAL AUTHOR(S) Nelson, R.B., Lade, P.V., Issa, J., Chamieh, N., and Yamamuro, J.						
13a. TYPE OF REPORT Final		13b. TIME COVERED FROM 8/15/86 TO 8/14/88		14. DATE OF REPORT (Year, Month, Day) November 1988		15. PAGE COUNT 116
16. SUPPLEMENTARY NOTATION						
17. COSATI CODES			18. SUBJECT TERMS (Continue on reverse if necessary and identify by block number)			
FIELD	GROUP	SUB-GROUP	Micromechanical Behavior			
			Frictional Materials			
			Discrete Element Method			
19. ABSTRACT (Continue on reverse if necessary and identify by block number)						
<p>This report presents the results of a two-year research program entitled, "Combined Experimental and Numerical Investigation of Inelastic Behavior of Frictional Geologic Materials," sponsored by AFOSR on Grant #86-0290. Section II of this report summarizes the results of a micromechanical analysis of frictional granular materials using a new discrete element program MASOM developed during the course of the research. The program is used to investigate the behavior of frictional materials in laboratory tests, such as the uniaxial compression and triaxial compression tests.</p> <p>The computer simulation MASOM is shown to realistically capture (macroscopic) behavior observed in physical tests. The effects of several important processes are revealed by the numerical simulation, namely (1) the effect of granular movement and rotation, (2) elasticity and fracture of the grains, (3) inhomogenous behavior of the particle assembly during loading, including the buildup of</p>						
20. DISTRIBUTION/AVAILABILITY OF ABSTRACT <input checked="" type="checkbox"/> UNCLASSIFIED/UNLIMITED <input type="checkbox"/> SAME AS RPT <input type="checkbox"/> DTIC USERS				21. ABSTRACT SECURITY CLASSIFICATION UNCLASSIFIED		
22a. NAME OF RESPONSIBLE INDIVIDUAL Major Steven C. Boyce			22b. TELEPHONE (Include Area Code) (202) 767-6963		22c. OFFICE SYMBOL AFOSR/NA	

DD Form 1473, JUN 86

Previous editions are obsolete.

SECURITY CLASSIFICATION OF THIS PAGE

UNCLASSIFIED

19. ABSTRACT (continued)....

loading chains and islands of quasistatic subassemblies, and (4) the relationship between the number of intergranular contacts and macroscopic strain.

The behavior of the frictional material is shown to be very complex, involving a number of different physical processes. To gain a better understanding of the micromechanical behavior a (VHS compatible) video tape was generated of the response of the particle assembly throughout the numerical simulation. A review of the response of the frictional material during the test shows the development of inhomogeneities associated with the accretion of particles to quasistatic islands of particles in the sample.

The experimental portion of the research, described in Section III of this report, has been directed toward developing a high pressure/high precision test facility capable of exercising a moderately large cylindrical specimen (3.0 in. diameter by 7.0 in. height) to stresses of the order of 1.0 kbar (15 ksi) in a conventional triaxial test. The objective of this effort was to build a device with sufficient sensitivity to permit an experimental examination of inelastic material behavior over a wide range of conditions where a number of important theoretical stability/instability issues have been raised.

While it was not possible to construct the facility, conduct a comprehensive test program, and coordinate the test results with the numerical analyses within the two-year grant period, the facility has been completed and tested at a range of 0.1 kbar where results can be compared with existing test data. Based on such comparisons, the test apparatus appears to be quite sensitive and able to track specified load or strain inputs at the level of approximately 0.1% of maximum values. The machine is designed to investigate quasistatic stress-strain behavior; however, the machine is driven by a high speed micro-computer driven control system and is limited only by the response times of the stepper motors which drive the hydraulic loading system. It is believed that the experimental test facility is capable of exercising moderately large samples of a frictional material over a wide range of triaxial loading conditions where theoretical issues regarding material stability can be explored experimentally.

The results of the experimental study will be forthcoming as addendums to the final report as they become available.

TABLE OF CONTENTS

	Page
I. INTRODUCTION	1
II. NUMERICAL ANALYSIS OF MICROMECHANICAL BEHAVIOR OF GRANULAR MATERIALS	3
II.1 Introduction	3
II.2 Technical Approach	10
II.2.1 Development of Consistent Internal Stress Strain Behavior for the Particles	11
II.2.2 Evaluation of Force-Displacement Relations at the Contacts	14
II.2.3 Numerical Integration of the Equations of Motion	17
II.2.4 Rotation Effects on Stress Calculations in Each Grain	18
II.2.5 Fracture of the Elements in MASOM	20
II.3 Analysis of Material Behavior Using MASOM	21
II.3.1 Introduction	21
II.3.2 Uniaxial Test Without Fracture	22
II.3.3 Uniaxial Test With Fracture	23
II.3.4 Qualitative Comparison of MASOM Results With Laboratory Tests	24
II.3.5 Triaxial Compression Test	24
II.3.6 Observed Behavior from the Numerical Test	25
II.3.7 Evolution of Particulate Mass During Loading	26
II.4 Concluding Remarks	26
III. DEVELOPMENT OF THE EXPERIMENTAL EQUIPMENT	71
III.1 Introduction	71
III.2 Details of Experimental Setup	73
III.2.1 Description of the Loading Frame	73
III.3 Description of the High Pressure Triaxial Apparatus (HPTA)	74
III.3.1 Upper Cap Plate and Loading Piston	74
III.3.2 The Cylinder Wall	75
III.3.3 The Base Plate	75
III.3.4 Pressure Sources	76
III.3.5 Pressure Source for Vertical Loading	76
III.3.6 Cell Pressure Sources	76
III.3.7 Control Panel and Pressure Lines	77
III.4 Computerized Datalogging and Test Control Systems	77
III.4.1 Typical Process Flow for Controlling a Test	77

III.5 System Performance and Control Capabilities	81
III.6 System Safety	83
III.6.1 Hardware Safety Features	83
III.6.2 Software Safety Features	84
III.7 Equipment Description	85
III.8 Software Description	87
III.9 Results of Two Experiments	95
III.10 Microphysical Characteristics of Granular Materials	96
III.11 Summary and Conclusions	97
IV. REFERENCES	108

Accession For		
NTIS	CRA&I	<input checked="" type="checkbox"/>
DTIC	TAB	<input type="checkbox"/>
Unannounced		<input type="checkbox"/>
Journal		<input type="checkbox"/>
A-1		



I. INTRODUCTION

The research presented in this report is the result of a two-year "Combined Experimental and Numerical Investigation of Inelastic Behavior of Frictional Geologic Material," supported by AFOSR Grant #86-0290. The objective of this research was to develop a coordinated experimental/analytical capability for investigating the basic physics of granular geologic materials emphasizing their microphysical behavior. The research is motivated by the fact that the inelastic behavior of geologic materials, except for very simple and thoroughly examined loading conditions, has been difficult to predict using classical continuum mechanical theories. A major conflict between theoretical and experimental results arises where laboratory tests demonstrate material behavior which cannot be captured using existing theoretical models for geologic materials. The primary issues have been centered around nonassociated flow, where inelastic flow is observed to differ significantly from theoretically accepted associated flow (perpendicular to material yield surfaces.) According to conventional continuum mechanical theory such materials will be unstable when exercised along certain strain or stress paths. Yet in laboratory tests the materials may or may not be stable.

Recognizing that continuum mechanical "stress-strain" models are fundamentally phenomenological in nature the current research is directed toward investigating geologic material behavior at the micromechanical level using both numerical and experimental methods. The results of a numerical analysis of micromechanical behavior of granular materials are contained in Section II of this report, which is a condensed version of a Ph.D dissertation of one of the co-authors (Issa). Section III is a description of a high pressure, high precision test facility constructed during the contract period. The facility is intended to be used for high precision triaxial tests of granular materials over a wide range of stress levels where many issues regarding nonassociated flow and the related issues regarding stability of geologic materials can be resolved experimentally.

As will be seen both the numerical and experimental programs are still under way and the two activities are not completely merged at present. The numerical analysis provides very interesting and realistic simulations but has been restricted to small assemblies of (200-300) grains due to computer budget limitations. This restriction has also prevented a full examination of a number of questions regarding parametric sensitivities (geometry of grains, contact friction, grain elasticity and fracture strength, etc.) The experimental test facility required a longer time to complete than initially estimated. However, the facility is now completed and high pressure testing is in progress. The device appears to have met all the high pressure/high sensitivity requirements set at the beginning of the project. Given these new capabilities for conducting numerical and experimental analyses of frictional granular materials, it is expected a number of new findings regarding the fundamental behavior of geologic materials will be produced as research continues. These results will appear as Addendums to this Final Report.

II. NUMERICAL ANALYSIS OF MICROMECHANICAL BEHAVIOR OF GRANULAR MATERIALS

II.1. Introduction

Perhaps the most striking characteristic of granular matter is its dual nature which lies between a disjoint, discrete material and a continuum. For, although the individual particles of the medium are solid, the particles are only partly connected. Thus the basic structure of the material varies greatly with loading and material behavior can range from solid to fluid with or without localized secondary physical processes, such as fracture, and shear slip band formation.

A granular medium may be defined as an aggregate of discrete, solid grains which occupy a nominal volume. The grains are free to displace with respect to their neighbors and the space between the particles may contain fluid, interstitial particles or be empty. The mechanical behavior of an assembly of granular materials is a complex integrated effect defined by the geometry of the structure and physics of contact, and in particular on the number and strength of the contact bonds which are themselves a consequence of the size, shape, roughness and strength of the particles. All these factors are incorporated into the concept of structure. The constraint on the motion of the individual particles can be either negligibly small or complete i.e., ranging from a suspension of particles to multicontacted particles forming a material with continuous force-deformation characteristics, i.e., a continuum. Perhaps the most significant feature of granular materials is that inelastic deformation is brought about by mutual sliding of the particles (intergranular deformation), in contrast to the deformation of the individual particles (intragranular deformation) or dislocation transport typical of a continuous medium. The ability of the body to maintain its shape to continue in the anisotropic state of stress, is a consequence of internal friction.

The differences in the behavior of granular materials when compared with the behavior of continuous materials are large enough to consider the mechanics of granular materials to be an autonomous branch of mechanics which is not directly related to the mechanics of solid continuous materials. Granular materials exist in a wide variety of technological fields. The oldest is soil mechanics with its problems of foundations, retaining walls, hill side stability and excavation. Such problems have been treated on a more or less scientific level for at least two centuries. The dynamical response of granular material has been investigated in connection with the propagation of seismic waves, petroleum prospecting, and in the past 25 years, with response of geological materials to blast and ground shock. The internal configuration of granular matter is found to be important in a variety of fields such as in the manufacture of ceramics, cement and mortar products, grinding wheels, powder metallurgy forming processes and composite materials.

The behavior of granular matter has attracted the attention of researchers since the 19th century, yet there still remain many unanswered questions especially concerning inelastic deformation and flow. Many theories have been developed on the macroscopic level by treating the granular assembly as a continuum. Today large finite element and finite difference computer programs use such material representations or models to simulate the behavior of granular matter. The credibility of these simulations resides directly on the complex mathematical models of granular materials designed to predict material behavior in realistic (arbitrary) loading conditions.

Nearly all of the mathematical models of frictional materials are based on nonlinear mathematical continuum mechanics theories ranging from simple curve following incremental elasticity models to complex hybrid incremental hypoelasticity nonassociated flow plasticity models [1,2,3,4,5,7]. Current state of the art continuum models for frictional materials are phenomenological in nature, that is, constructed to reproduce macroscopic behavior observed

in experiments, with little attention paid in their development to the physics of the microscopic behavior of granular interaction.

This approach has been successful in predicting the behavior of metals where continuum models are based on incremental plasticity theory. It is not surprising therefore that the historical development of continuum models for granular materials followed the same approach, nor that as a first step the successful metal plasticity models were extended to account for pressure sensitive frictional behavior.

Unfortunately the extension of metal plasticity based models to granular media has led to difficult problems which have yet to be solved. Generally, phenomenologically based continuum models are able to reproduce most test data reasonably well, especially for tests where the material is subjected to (nearly) monotonically increasing loads to the point of failure. For tests involving cyclic loadings, even the best of today's models have difficulty in capturing qualitative effects reliably or in loading regions different than those used in the model development. In other words, the capability of current models to predict behavior of frictional materials to arbitrary loads is a major problem.

To make matters worse, the development of modern continuum models capable of accurately simulating test data has introduced a number of perplexing issues of a theoretical nature [1]. Certainly, any mathematical model should not violate the laws of thermodynamics (for example, by generating energy in closed loadings cycles) nor should the model predict discontinuous behavior, where two arbitrarily close finite stress paths produce finite differences in strains, unless such a process occurs physically as by say a material failure. A third requirement is that the mathematical relationships should be unique in the sense of predicting a one to one correspondence between incremental changes in stress and strain. Finally, the model should not indicate unstable material behavior if in fact the behavior of physical material is stable, and vice versa.

In an effort to account for realistic material behavior, complex, but theoretically "safe" models based on associated flow incremental plasticity have been developed [4,5,6]. These material models can be made to obey all the basic thermodynamic and continuity requirements imposed. Unfortunately, such models do not give a realistic representation of ordinary materials because inelastic strain increments developed when the material is exercised in shear are not perpendicular to the yield surface, a characteristic phenomenon known as nonassociated plastic flow for frictional granular materials [35].

A different attempt to treat the observed behavior of granular materials has evolved from high pressure physics, where the basic information describing material behavior is in the form of a pressure/volume relationship [1]. For problems in the low pressure region shear strength becomes important. To accommodate this effect, shear strength was appended to the pressure/volume relationship using Prandtl/Reuss (volume constant) plasticity relations to describe shear induced inelastic behavior. These models are hybrid in the sense that the pressure/volume effect is partially decoupled with the pressure dependent shear behavior. These material models can be made to fit test data significantly better than the associated flow models. Unfortunately these models can be shown to violate some of the theoretical requirements from basic physics, namely the requirement against energy generation and sometimes the continuity requirement as well.

In summary, it can be said that while associated flow, hybrid elasto-plastic and non-associated flow plasticity type models may give reasonable fits to test data and adhere reasonably well to basic principles, no single model is able to capture all observed behavior of granular materials and at the same time meet all theoretical requirements. This is in spite of more than thirty years of research on the problem of developing a satisfactory mathematical representation for granular materials.

Therefore, this research is directed towards attempting to better understand the basic physical processes which are dominating the behavior of granular matter. These processes are all believed to be at a localized interparticle level. That is, macroscale "stress-strain" material behavior is a consequence of the physics of contact and friction between particles of granular materials. If this behavior can be clearly understood then it is believed that it will be much easier to establish a theoretically sound and accurate continuum model.

Most of the early analytical work, in an attempt to refine the traditional continuum models, took a natural step in the direction of replacing a continuous medium by one in which account is taken of forces transmitted between individual particles. Initial work along these lines approximated the particles by rigid spheres.

Hara [8] seeking to predict the behavior of the carbon microphone, studied the propagation of compressional waves through an aggregate of like elastic spheres arranged in simple cubic and face-centered cubic arrays, replacing the granules by a series of mass-spring systems in series, and computing the stiffness of each spring on the basis of Hertz's theory of contact.

Proceeding in a similar vein, Gassman [9] approximated the earth's crust by an array of like spheres in a hexagonal close packing. When subjected only to its own weight, and when the stiffness at the individual contacts was computed on the basis of Hertz theory, this array was shown to have elastic constants appropriate for a continuum with transverse isotropy. The abandonment of the regular lattice served as the starting point for a study by Brandt [10] who considered a model consisting of several sets of like spheres, the spheres in a given set fitting in the interstices of the preceding set.

The inclusion of tangential contact forces by Mindlin and Deresiewicz [12] in the solutions of elasticity equations produced significant corrections, since the stiffness of a contact in

a tangential direction is of the same order of magnitude as its stiffness in the direction of its normal. Duffy and Mindlin [11,12] also computed the incremental contact forces and incremental stress-strain relations for the face centered cubic array under initial isotropic and uniaxial compressive stress.

Using similar static analyses, Verruijt and De Josselin De Jong [13], Oda and Konishi [14] have revealed the existence of chains of stresses in the material, but, due to experimental difficulties, they were unable to bring out clearly the evolution of the contact forces under overall stresses.

Kinematical approaches for analyzing the displacements of the particles were based on the study of the geometrical evolution of a two-dimensional granular structure. Studies by Biarez [15], Wiendieck [16], Matsuoka [17], Oda, et al. [18], and Chapuis [19] reveal the existence of a structural anisotropy which evolves with deformation and which is a kinematical demonstration of the memory of the material. Another recent interesting approach by Christofferson and Nemat Nasser [18], and Oda [18], proposes to define stresses in terms of the fabric and other microstructural characteristics of granular mass. Cambou [21] proposed a description of the state of a granular material based on statical analysis. He constructed a numerical model to show that this kind of description is able to take into account the loading history of the material. He concluded that the so-called hardening of granular material is neither isotropic nor kinematic. Matsuoka [22] proposed a stress-strain model for granular materials by consideration of the mechanism of fabric change under shear. He derived a relationship between strains and fabric change of granular materials by considering two particles and the mechanism of disappearance and generation of interparticle contacts with a third particle.

On an entirely different line of approach, the mechanics of granular materials can be investigated using stochastic techniques and modeling. Attempts in this direction were made by Massal [23], Kitamura [24] and Chikwendu [25]. Recently progress was made by exploring the kinetic theory for rapid flow of rough inelastic particles. Ogawa [26], and Savage [27] have been partially successful in applying such formulation to the flow of granular materials.

Serrano and Rodriguez-Ortiz [28] developed a numerical model for assemblies of discs and spheres. Contact forces and displacements are calculated for equilibrium conditions assuming that increments of contact forces are determined by incremental displacements of the centers of the particles. A major draw-back of the method used to solve the equations is that only a relatively small number of particles can be processed.

A separate type of approach is based on the Distinct Element Method (DEM), a numerical method that is capable of handling disconnected particles of any shape developed by Cundall [29] for the analysis of rock mechanics problems. In the distinct element method, the interaction of the particles is viewed as a transient problem with states of equilibrium developing whenever the internal forces balance. Cundall and Strack [30] used a version of discrete element method named Ball to investigate two-dimensional behavior of arbitrarily sized circular grains subjected to a variety of strain paths.

Bazant [31] recently used a simplified numerical method to study the microstructure and crack-growth in geomaterials. This method is somewhat related to the discrete element method as the frictional interaction is replaced by a force-displacement relation with a tensile strength limit. However block motion and the on-off nature of contacts were incompletely treated.

The discrete element method serves as a starting point to developing an understanding of the primary physical processes which govern the behavior of granular materials. As with

earlier research using DEM the level of modeling will be two-dimensional and at the micro-physical level where assemblies of arbitrarily shaped and oriented material particles will be analysed to simulate the behavior of a real granular material. For this purpose a new program MASOM (Micromechanical Analysis and Simulation of Materials) has been written during the current research program. This program is based on an earlier program for the response of block systems named PROBS [32,33,34,35], which in turn evolved from Cundall's early RBM (Rigid Block Mechanics) program [29]. Although based on PROBS the program has a re-worked solution strategy and completely new physics of intraelement and interelement behavior. In its current form, the computer program is capable of analysing frictional contact forces damping and granular deformation, and includes an ability to represent grain crushing at high pressure. The program has well been developed to optimize computational efficiency.

The program is used to investigate microphysical behavior of geologic materials by simulating conventional laboratory tests such as uniaxial strain, triaxial compression and simple shear. A number of interesting results were obtained as will be seen in the following. One development which proved very helpful in understanding micro-mechanical behavior is that of a graphics software capability for creating a metafile consisting of video frames for animation, i.e., producing movies of the test simulation. This simulation revealed several processes which cannot be shown with conventional time history plotting or graphical displays of the computer models at specified times.

II.2 Technical Approach

In this section, several major features of a computer code named MASOM (Micro Analysis Simulation of Materials) developed during the course of the research are described. The program provides a foundation for investigating the microphysics of geological materials.

As noted above MASOM is based on PROBS [32-35] and follows the same general methodology for analysing discrete element systems. As with PROBS, the MASOM program tracks the behavior of an assembly of arbitrarily shaped two dimensional polygons by means of an explicit time integration scheme. There is no restriction other than computational expense (and computer memory) on the size of the problem which can be analysed.

As with PROBS a number of different groups of elements can be defined, each with its own intraelement and interelement contact relationships with other element groups. However, the PROBS computer program, which was used to investigate high velocity impact problems, contains a number of approximations which made it impossible to use the program to investigate low velocity-to-quasistatic processes and, in particular, the basic micromechanical behavior of granular materials subjected to quasistatic loads typical of most conventional laboratory tests.

The new features in MASOM which distinguish this program from PROBS, and which make it possible to analyse microphysical behavior of frictional, granular materials are described next.

II.2.1 Development of Consistent Internal Stress Strain Behavior for the Particles

A consistent methodology for updating the strain rate in each particle is a basic requirement for representing the response of individual grains. In PROBS this was accomplished using mathematical techniques which could not be justified on a rational physical basis. Thus, a number of major changes were requested. In the current procedure three independent constant strain rate modes exist in each particle and their behavior is based on an application of the Betti-Rayleigh theorem from classical linear elasticity theory.

The reciprocal identity or the Betti-Rayleigh theorem represents a relation between two different static elastic states on the same body. Consider two states, both in a state of static equilibrium, (σ_{ij}^I, u_i^I) and $(\sigma_{ij}^{II}, u_i^{II})$ with surface tractions $t_i^I = \sigma_{ij}^I n_j$ and $t_i^{II} = \sigma_{ij}^{II} n_j$, respectively. Then the Betti-Rayleigh theorem states that

$$\int_V \rho f_i^I u_i^{II} dv + \int_S t_i^I u_i^{II} ds = \int_V \rho f_i^{II} u_i^I dv + \int_S t_i^{II} u_i^I ds \quad (II.1)$$

where v denotes the volume of the body and S its surface.

Now, from virtual work

$$\int_V \sigma_{ij}^I \epsilon_{ij}^{II} dv = \int_V \rho f_i^I u_i^{II} dv + \int_S t_i^I u_i^{II} ds \quad (II.2)$$

where σ_{ij}^I is a stress state in equilibrium and u_i^{II} is a displacement field and $\epsilon_{ij}^{II} = \frac{1}{2} (u_{i,j}^{II} + u_{j,i}^{II})$. Note that type I information is unrelated to type II information.

Now let the stress state I be of the form

$$\sigma_{ij}^I = \delta_{i1} \delta_{1j} \quad (II.3)$$

The corresponding strains are

$$\epsilon_{ij}^I = \frac{1}{2\mu} \sigma_{ij}^I - \frac{\lambda}{2\mu(3\lambda + 2\mu)} \sigma_{kk}^I \delta_{ij} \quad (II.4)$$

Substitution of (II.3) into (II.4)

$$\epsilon_{ij}^I = \frac{1}{2\mu} \delta_{i1} \delta_{1j} - \frac{\lambda}{2\mu(3\lambda + 2\mu)} \delta_{k1} \delta_{1k} \delta_{ij} \quad (II.5)$$

One displacement field which satisfies Eq. (II.5) is

$$u_i^I = \frac{1}{2\mu} \delta_{i1} x_i - \frac{\lambda}{2\mu(3\lambda + 2\mu)} \delta_{ij} x_j \quad (II.6)$$

Now by using Betti-Rayleigh reciprocity theorem without any body force terms f_i^I or f_i^{II} ,

$$\int_v \sigma_{ij}^I \epsilon_{ij}^{II} dv = \int_S t_i^{II} u_i^I ds \quad (II.7)$$

Using the stress state in Eq. (II.3)

$$\int_v \delta_{i1} \delta_{1j} \epsilon_{ij}^{II} dv = \int_S t_i^{II} u_i^I ds \quad (II.8)$$

substitution of the expression of u_i^I in Eq. (II.6) gives

$$\int_v \delta_{i1} \delta_{1j} \epsilon_{ij}^{II} dv = \int_S t_i^{II} \left[\frac{1}{2\mu} \delta_{i1} x_i - \frac{\lambda}{2\mu(3\lambda + 2\mu)} \delta_{ij} x_j \right] ds \quad (II.9)$$

Taking type II information to be the change in the actual first strain rate mode

$$\int_v \dot{\epsilon}_{i1} dv = \int_S \dot{t}_i \left[\frac{1}{2\mu} \delta_{i1} x_i - \frac{\lambda}{2\mu(3\lambda + 2\mu)} \delta_{ij} x_j \right] ds \quad (II.10)$$

where the $(\dot{\cdot})$ denotes the rate of change.

Using the stress state

$$\sigma_{ij}^I = \delta_{i2} \delta_{2j} \quad (II.11)$$

a similar expression holds for the second strain rate mode

$$\int_v \dot{\epsilon}_{22} dv = \int_S \dot{t}_i \left[\frac{1}{2\mu} \delta_{i2} x_i - \frac{\lambda}{2\mu(3\lambda + 2\mu)} \delta_{ij} x_j \right] ds \quad (II.12)$$

The stress state

$$\sigma_{ij}^I = \delta_{i1} \delta_{2j} \quad (II.13)$$

gives

$$\epsilon_{ij}^I = \frac{1}{2\mu} \delta_{i1} \delta_{2j} - \frac{\lambda}{2\mu(3\lambda + 2\mu)} \delta_{k1} \delta_{2k} \delta_{ij} \quad (II.14)$$

The second term in the right hand side expression is identically equal to zero, therefore

$$\epsilon_{ij}^I = \frac{1}{2\mu} \delta_{i1} \delta_{2j} \quad (\text{II.15})$$

Using a displacement associated with ϵ_{ij}^I of the form

$$u_i^I = \frac{1}{2\mu} (\delta_{i1} \delta_{2j} x_j + \delta_{j1} \delta_{2i} x_j) \quad (\text{II.16})$$

the third strain rate mode follows using the same argument

$$\int_V \dot{\epsilon}_{12} dv = \int_S \dot{t}_i (\delta_{i1} \delta_{2j} x_j + \delta_{i2} \delta_{1j} x_j) ds \quad (\text{II.17})$$

The three expressions for the strain rate modes all may be written in a single expression

$$\int_V \dot{\epsilon}_{ij} dv = \int_S \left[\frac{1}{2\mu} (\dot{t}_i x_j + \dot{t}_j x_i) - \frac{\lambda}{2\mu(3\lambda + 4\mu)} \dot{t}_k x_k \delta_{ij} \right] ds \quad (\text{II.18})$$

For the particular case of concentrated (contact) forces applied on the boundary

$$\dot{t}_i = F_i \delta(x - \rho) \delta(y - \eta) \delta(z - \gamma) \quad (\text{II.19})$$

Then the surface integral is reduced to a summation over the contact points and

$$\int_V \dot{\epsilon}_{ij} dv = \sum_{\text{Contacts}} \left[\frac{1}{4\mu} (\dot{F}_i x_j + \dot{F}_j x_i) + \right. \\ \left. - \frac{\lambda}{2\mu(3\lambda + 2\mu)} \dot{F}_k x_k \delta_{ij} \right] \quad (\text{II.20})$$

Equations (II.20) represent three constant strain rate modes in each grain. These constant strain modes will be used to update the corners positions as well as the internal stresses using Hooke's law.

II.2.2 Evaluation of Force-Displacement Relations at the Contacts

Local deformations are assumed to occur at contacts between corners and edges, see Fig. II.1. The force-displacement laws are evaluated in incremental form, that is to say, changes in displacements for a given contact are evaluated given changes in horizontal, and

vertical displacements and rotations, as well as the deformations within the two elements in contact. The new shear and normal forces are then calculated by summing the old forces and the new force increments. These contact forces are then resolved into equivalent horizontal and vertical forces and moments, and added to the other forces and moments acting on the element. In the original PROBS program only simplistic linear normal contact forces were employed, a serious limitation. In the present work all contact forces are based on Mindlin's theory of contact [12].

As a first step the relative velocities of the corner relative to an edge at a contact must be obtained. Thus,

$$\begin{aligned} \dot{X}_\alpha^c = & \dot{X}_\alpha^i - \dot{X}_\alpha^j + (\dot{\epsilon}_{\alpha\beta}^i + \dot{R}_{\alpha\beta}) (X_\alpha^c - X_\alpha^i) - (\dot{\epsilon}_{\alpha\beta}^j \\ & + \dot{R}_{\alpha\beta}^j) (X_\alpha^c - X_\alpha^j) \quad \alpha, \beta = 1, 2 \end{aligned} \quad (\text{II.21})$$

where

$$[\dot{R}_{\alpha\beta}] = \begin{bmatrix} 0 & \dot{\theta} \\ -\dot{\theta} & 0 \end{bmatrix} \quad \dot{\theta} : \text{angular velocity.}$$

- $\dot{\epsilon}_{\alpha\beta}$: strain rate
- X_α^i : global centroid coordinate of element i
- X_α^j : global centroid coordinate of element j
- X_α^c : global coordinate of contact point

The incremental shear and normal displacements are therefore

$$\Delta X_\alpha = J_{\alpha\beta} \dot{X}_\beta^c \Delta t \quad (\text{II.22})$$

where

$$[J_{\alpha\beta}] = \begin{bmatrix} \cos\gamma & \sin\gamma \\ -\sin\gamma & \cos\gamma \end{bmatrix} \quad (\text{II.23})$$

and γ is the angle of the edge with the global X coordinate axis.

The contact shear T and normal force N at the contact are based on Mindlin's theory [12] and are evaluated assuming rounded contact surfaces

$$N = \left[\frac{4 R_i R_j}{9 \pi^2 \left(\frac{1 - \nu^2}{\pi E} \right)^2 (R_i + R_j)} \right]^{1/2} \delta_N^{3/2} \quad (\text{II.24a})$$

$$T = \left[1 - \left[1 - \frac{\delta_T}{KfN^{2/3}} \right]^{3/2} \right] f N \quad (|T| \leq f N) \quad (\text{II.24b})$$

or

$$|T| = f N \quad (|T| > f N) \quad (\text{II.24c})$$

In these formulas K, R_i and R_j are given by the expressions

$$K = \frac{3(2 - \nu)}{16\mu \left[\frac{6\pi^2 E R_i R_j}{8(1 - \nu^2)(R_i + R_j)} \right]^{1/3}} \quad (\text{II.25a})$$

$$R_i = \left[\frac{A_i}{\pi} \right]^{1/2} = \text{Average Radius of Element } i \quad (\text{II.25b})$$

$$R_j = \left[\frac{A_j}{\pi} \right]^{1/2} = \text{Average Radius of Element } j \quad (\text{II.25c})$$

and A_i, A_j are the areas of elements i and j , respectively. Also, f denotes the friction coefficient between the contacting bodies.

II.2.3 Numerical Integration of the Equations of Motion

The force and moments generated on each element are used to compute horizontal, vertical and rotational accelerations. The accelerations are then integrated to give velocities, and integrated again to give displacements.

Each grain, with mass m_i and moment of inertia I_i , is assigned three independent degrees of freedom at the element centroid, namely X_1 , X_2 and θ , the displacements in the 1 and 2 directions and rotation, respectively. The grain must obey the following equations of motion

$$m_i \frac{d^2 X_\alpha}{dt^2} + C_i \frac{dX_\alpha}{dt} + F_{i\alpha} = 0 \quad \alpha=1,2 \quad (\text{II.26})$$

$$I_i \frac{d^2 \theta}{dt^2} + D_i \frac{d\theta}{dt} + M_i = 0$$

where $F_{i\alpha}$ is the sum of forces in the 1 or 2 direction, and M_i is the sum of all moments of force (about the centroid) for the particle. The constants C_i and D_i denote damping coefficients.

Consider the nonlinear second order differential equation a special case of which is any of Eq. (II.26),

$$\ddot{X} + a \dot{X} = \frac{1}{m} F(X, \dot{X}) \quad (\text{II.27})$$

In Eq. (II.27) X , \dot{X} , \ddot{X} are displacement, velocity and acceleration, respectively, and m is the mass of the element. The quantity $F(X, \dot{X})$ is the force generated from contacts and other applied (body) forces.

In order to integrate the equations the derivatives at time t may be written

$$\ddot{X} = \frac{\dot{X}^{t+\Delta t} - \dot{X}^t}{\Delta t} \quad (\text{II.28a})$$

$$\dot{X} = \frac{\dot{X}^{t+\Delta t} + \dot{X}^t}{2} \quad (\text{II.28b})$$

Substitution of Eqs. (II.28a) into Eq. (II.28b) gives the following

$$\frac{\dot{X}^{t+\Delta t} - \dot{X}^t}{\Delta t} + a \left[\frac{\dot{X}^{t+\Delta t} + \dot{X}^t}{2} \right] = \frac{1}{m} F(X, \dot{X}) \quad (\text{II.29})$$

which is solved for the velocity at $t + \Delta t$:

$$\dot{X}^{t+\Delta t} = \left[\frac{1 - a \Delta t/2}{1 + a \Delta t/2} \right] \dot{X}^t + \left[\frac{\Delta t}{1 + a \Delta t/2} \right] \frac{F(X, \dot{X})}{m} \quad (\text{II.30})$$

The new values for velocities are used to update the displacements and rotations of the elements by a further numerical integration

$$X^{t+\Delta t} = X^t + \dot{X} \Delta t \quad (\text{II.31})$$

This integration scheme is unconditionally stable if F is independent of X or \dot{X} . If the force is a linear function of X , i.e., linear elastic behavior is present ($F = KX$), then the procedure is conditionally stable provided $\Delta t < 2\sqrt{m/K}$. But the presence of the nonlinear force term $F(X, \dot{X})$, which depends strongly on the number of contacts for each grain, may produce numerical instability in the solution. Under numerically unstable conditions the contact forces will be very large, and fluctuate wildly from iteration to iteration. (The results generated by the program are meaningless under such a situation; the problem must be re-run with a smaller time step.)

II.2.4 Rotation Effects on Stress Calculations in Each Grain

If a grain, together with the forces acting on it, is rotated, the internal stresses, referred to local axes, are unaffected. However, the stresses, as expressed in global coordinates will

change. It is common in Lagrangian finite-difference codes to apply stress correction terms to the stresses at each time step in order to allow for this apparent stress change due to rotation. The correction terms are derived from the tensor transformation equations used to determine stresses in a new coordinate system when they are known in an old system.

Denote the old coordinates system by X_i ($i=1,2,3$) and the new coordinates system by \bar{X}_i ($i=1,2,3$). The tensorial relations that relate the stresses $\bar{\sigma}_{ij}$ in the new coordinate and the stresses σ_{ij} in the old coordinate system are as follows.

$$\bar{\sigma}_{ij} = \sigma_{\alpha\beta} \frac{\partial \bar{X}_i}{\partial X_\alpha} \frac{\partial \bar{X}_j}{\partial X_\beta} \quad (\text{II.32})$$

Let

$$[J_{ij}] = \left[\frac{\partial \bar{X}_i}{\partial X_j} \right] = \begin{bmatrix} \cos\theta & \sin\theta \\ -\sin\theta & \cos\theta \end{bmatrix} \quad (\text{II.33})$$

where θ is the angle of rotation between the two coordinate systems. If θ is a small change, say $\Delta\theta$ occurring over a single time step Δt , $[J_{ij}]$ can be approximated by

$$[J_{ij}] = \begin{bmatrix} 1 & \Delta\theta \\ -\Delta\theta & 1 \end{bmatrix} \quad (\text{II.34})$$

Noting that $\Delta\theta = \dot{\theta} \Delta t$, then

$$J_{ij} = \delta_{ij} + \dot{R}_{ij} \Delta t \quad (\text{II.35})$$

where

$$[R_{ij}] = \begin{bmatrix} 0 & \dot{\theta} \\ -\dot{\theta} & 0 \end{bmatrix} \quad (\text{II.36})$$

Using this expression for J_{ij} in (II.35)

$$\begin{aligned}\bar{\sigma}_{ij} &= \sigma_{\alpha\beta} (\delta_{i\alpha} + \dot{R}_{i\alpha} \Delta t)(\delta_{j\beta} + \dot{R}_{j\beta} \Delta t) \\ &= \sigma_{ij} + (\sigma_{\alpha j} \dot{R}_{i\alpha} + \sigma_{i\beta} \dot{R}_{j\beta}) \Delta t\end{aligned}\quad (\text{II.37})$$

These new stresses correspond to a change in coordinate axes. However, in the case of a particle rotating and the coordinate axes remain fixed, and the correction term is opposite

$$\Delta\sigma_{ij} = -(\sigma_{\alpha j} \dot{R}_{j\alpha} + \sigma_{i\beta} \dot{R}_{j\beta}) \Delta t \quad (\text{II.38})$$

In MASOM the internal stresses are updated in each element using the strain rate and stress correction as follows

$$\sigma_{ij}^{t+\Delta t} = \sigma_{ij}^t + (\lambda \dot{\epsilon}_{kk} \delta_{ij} + 2\mu \dot{\epsilon}_{ij} - \sigma_{kj}^t \dot{R}_{iK} - \sigma_{iK}^t \dot{R}_{iK}) \Delta t \quad (\text{II.39})$$

II.2.5 Fracture of the Elements in MASOM

The fracture of grains under multiaxial loading conditions can be an important aspect of the micro-mechanics of frictional materials. The grain fracture criterion incorporated in MASOM is based on the assumption that cracking occurs when point loads are applied on opposite sides of a grain. In its ideal form, this type of approach constitutes the "Brazilian test" and is performed with a disc loaded between flat plates. More generally, many point load tests have been performed in which irregular shapes are loaded between two indentors that may have small radii of curvature. These tests are characterized by a failure load that is related to the distance between the points of application of the loads, and a strength that is supposed to be constant for a given material.

In the MASOM program the relationship for fracture is taken to be the simple form $S = K F/d^2$, where F is the average of co-linear compressive forces applied on opposite sides of the grain, d is the distance between applied loads, k is a factor that depends on the shape of the grain, and S is the material strength, taken to be constant.

During each cycle of the solution, each grain is scanned for the sum of the largest co-linear forces, say F_1 and F_2 applied to the grain by corners from other grains. The average of these forces $\frac{1}{2}(F_1 + F_2)$ is then taken, divided by their separation distance (squared), and compared to the specified strength S . If $\frac{1}{2}(F_1 + F_2)/d^2 > S$ crack is formed; if $\frac{1}{2}(F_1 + F_2)/d^2 \leq S$ no crack is formed. Once the crack has been formed; the element is separated into two pieces along the line of the crack. The coordinates of the new elements are reset and the new grains are created. Internal stress and strains are set equal zero in the new grains.

II.3 Analysis of Material Behavior Using MASOM

II.3.1 Introduction

The computer program MASOM models the movement and interaction of the many particles which make up the material, during simulations of material response. The sample of the material is generated from a microphotograph of a real granular material; each particle is modeled as a polygon of a shape and size resembling a particle in the photograph. A digitizer is used to generate the data file to be used by the computer program.

During such numerical experiments, a variety of boundary conditions and loading as well as unloading sequences may be specified, and measurements made of contact force orientation and magnitude, as well as average stress and strain, or other variables of interest.

In this section the physical tests which simulated using MASOM are the uniaxial strain and triaxial compression and simple shear tests.

II.3.2 Uniaxial Test Without Fracture

The uniaxial test simulation was based on data for Cambria beach sand. The computer model in Fig. II.2 consists of 227 particles with maximum dimension varying between 0.5 and 2.0 mm. The elastic properties for the grains are [37], $E = 4.5 \times 10^7 \text{ Kg/mm} \cdot \text{s}^2$, Young's modulus, and $G = 1.8 \times 10^7 \text{ Kg/mm} \cdot \text{s}^2$, the Shear modulus. Three additional elements are fixed to simulate the fixed uniaxial strain test chamber and two carry the loads which are applied gradually over time. Figure II.3 shows the sample with a gravity field acting on it but without any load applied by the apparatus. The intensity of the shading gives an indication on the magnitude of the different stresses inside each grain. (Vertical shading correspond to the vertical stress σ_y , horizontal shading correspond to σ_x , and the oblique shading correspond to the shear stress σ_{xy} .) Note the build up of stress with depth, i.e., the lithostatic effect. Figure II.3 shows concentrations of stiff chains of particles that carry the applied load (in this case is the weight of the particles), which is very non uniform. Figure II.4a and II.4b show small dots on some of the corners, the dots indicating that the corresponding corners are sliding along their contacting edges. Evidently lithostatic behavior is highly inhomogeneous.

The uniaxial strain test was simulated by integrating the system for 10,000 cycles. Contact force magnitudes and directions as well as displacements and velocities were collected every 100 cycles to construct the stress strain relation for the test. Vertical stress versus vertical strain curve is shown in Fig. II.5. The maximum strain reached about 11% and the residual strain obtained after unloading was around 3.5%. Figure II.6 shows the stress path which is the stress difference or deviatoric stress $\sigma_x - \sigma_y$ versus "pressure" $\frac{\sigma_x + 2 \sigma_y}{3}$. Since the program is 2D there is a tacit assumption that $\sigma_y = \sigma_z$, and this assumption is used whenever pressure effects are quantified.

Figure II.7 shows the variation of the number of contacts as a function of the vertical stress. The relationship between stress and the number of the contacts is, with the exception of early redistributions, remarkably close to that between stress and strain.

II.3.3 Uniaxial Test With Fracture

The uniaxial test simulation with fracture allowed was re-analysed using the same Cambria beach sand material properties as in II.3.2. In addition to these elastic properties, the material strength constant was set $S = 10^8 \text{ Kg/mm s}^2$. Recognizing that the cracking limit is inversely proportional to the square of the distance between the application of the contact forces, this criterion results in fracture of the smaller particles first. For this uniaxial test 47 particles have fractured out of 227 particles for the model. The maximum cracking line was 1.15 mm (this model the maximum dimension for the particles size varies between 0.5 mm and 2.0 mm).

The plots shown in Figs. II.9 through II.14 display results for the uniaxial test. Fracture occurs around the cycle 1400 when the material fracture strength is reached. Initiation of cracking occurs first on the smaller particles, which because of their small dimension are unable to resist intense loads as effectively larger grains with equal strength properties. As cracking occurs some re-distribution of forces develop but the general patterns of contact force and force direction are disturbed only slightly. The unloading phase begins after cycle 1600.

The plots in Figs. II.15 through II.17 displays transmission of the contact forces inside each element. The thickness of these lines are proportional to the magnitudes of the contact forces. A remarkable feature here is the preponderance of vertically oriented contact forces, i.e., the low material confinement forces.

Contact force magnitudes and directions as well as displacements and velocities were collected for all particles of the sample and at the boundaries. These forces and displacements are used to construct an overall stress strain relation for the material. Vertical stress versus vertical strain is shown in Fig. II.18. The curve shows a sudden drop of the stress level near the peak, i.e., when the particles are allowed to fracture. After rearrangement of the particles due to fracture, the sample will regain some strength before the unloading phase. The maximum strain reached was about 18% and the residual strain obtained after unloading was about 14%. Figure II.19 shows the stress path taken, i.e., the stress difference or deviatoric stress $(\sigma_x - \sigma_y)$ versus pressure $(\frac{\sigma_x + 2\sigma_y}{3})$.

II.3.4 Qualitative Comparison of MASOM Results With Laboratory Tests

Figure II.20 shows the stress strain relation obtained in the UCLA soils laboratory for the uniaxial strain test on Cambria Sand. The test was performed using a triaxial cell and by applying gradually increasing lateral stresses in order to maintain zero lateral strain. In spite of differences between the void ratio in the laboratory sample and the computer model and in applied stress levels (150 bar maximum stress in the computer simulation compared to 25 bar in the laboratory test), the numerical simulation appears to have captured the general behavior of the material for the loading phase as well as the unloading phase, see Fig. II.18 and Fig. II.20.

II.3.5 Triaxial Compression Test

The triaxial compression test using a sample of Cambria sand was analysed using MASOM but without fracture. The computer model in Fig. II.21 illustrates the boundary conditions used for the numerical test. The horizontal plates carry the vertical loads, both top and bottom are allowed to move. Confining loads are carried by the vertical elements.

In the first phase of loading, that of isotropic compression, vertical and horizontal loads are increased gradually and at the same rate up to 50 bar. In the second phase, termed triaxial compression, the vertical force is increased up to 150 bar while maintaining the same confining pressure of 50 bar in the horizontal direction. The increasing vertical load produces a downward motion of the top plate, but variable behavior of the vertical confinement.

The plots shown in Fig. II.22 through II.32 displays results for both phases of the triaxial compression test with the stress level reached in both the vertical and horizontal directions. Figures II.33 through II.39 show the contact forces transmission displayed inside each particle. The thicknesses of these lines are proportional to the magnitudes of the contact forces.

The element data and contact forces information were collected during the numerical analysis. Contact forces and boundary displacements were used to construct the curve in Fig. II.40 which represents the deviatoric stress ($\sigma_1 - \sigma_2$) versus the vertical strain ϵ_1 . Figure II.41 shows the stress path σ_1 versus $\sqrt{2} \cdot \sigma_2$. Clearly the first section of the curve represents the isotropic compression phase and the second section represents the vertical loading phase.

II.3.6 Observed Behavior from the Numerical Test

The computer simulation using MASOM is shown to realistically capture macroscopic behavior observed in physical tests. The effects of several important processes are revealed by the numerical simulation, namely

1. The effect of particle movement (displacement and rotation).
2. The particles elastic behavior and subsequent fracture at high stress levels.
3. Inhomogenous behavior of the system of particles during loading.
4. Build up of loading chains and islands of quasistatic subassemblies.

5. Relationship between intergranular contact numbers and strain resembles the stress strain relationship.

II.3.7 Evolution of Particulate Mass During Loading

The behavior of the frictional material is very complex, involving a number of different physical processes as may be seen from the computer generated field plots of the particulate assembly at various phases of loading. To gain a better understanding of the evolution of particle interaction, a video tape was generated of the response of the system throughout the duration of the load-unload cycle. The evolution of physics observed during the numerical experiment shows that the applied loads are carried by chains of grains in the direction of maximum compressive strain rate. The distortion of these chains resembles the buckling of a curved beam or arch, and neighboring particles exhibit large motion and mainly rotation without the appearance of large stresses.

The structural behavior of the granular material considered appears to consist of two structures behaving differently. The first is made up of stiff chains and behaves like a complex elastic truss. The deformation patterns of this truss imposes local deformation on the particles of a second type of structure confined by the chains of the first structure whose behavior is similar to a perfectly plastic material due to the relatively small compressive stress acting on it. As the applied load increases the elements of the first structure become progressively more kinked, and therefore less able to carry load. The load is then transferred to neighboring elements of the secondary structure as increasing deformation brings more grains into contact.

II.4 Concluding Remarks

The micromechanical analysis conducted using the MASOM computer program reveals an intricate, and continually changing microphysics at the intra- and interparticle level. The

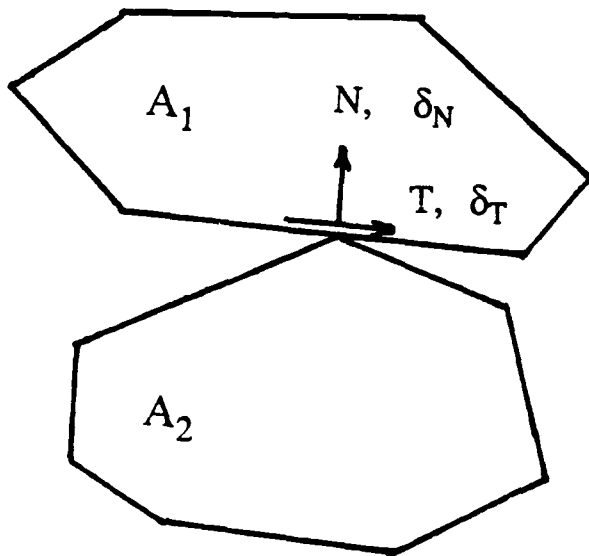
program permits a careful examination of granular displacement and rotation, deformation and possible fracture at high stress levels. Given the results of the numerical simulation, which includes contact force distribution and displacements along the boundaries, it is possible to construct the stress strain relations for overall behavior of finite samples of the frictional material. In particular, two standard laboratory tests, the uniaxial strain test and the triaxial compression test were analysed numerically for loadings well into the inelastic range. The numerical analysis has captured the general behavior of the material during both loading and unloading phases.

However, it is clear that the present analysis could be improved in future work. Several areas of research should be mentioned where real progress could be made to better understand the micro-mechanical behavior of granular materials. First and simplest, the current sample used in both the uniaxial strain test and the triaxial compression test, consisting of 227 particles, is too small to permit the investigation of stability issues. In the current research, the size of the computer model was restricted due to limited computational resources and the numerically intensive calculations involved for the type of simulation using MASOM. It is hoped that more computational support will be available in the future to permit more finely resolved models with more grains, so that stability issues can be explored numerically.

Another important computer resource constraint pertains to the modeling of individual grains. In the present model the polygonal shapes were restricted to a maximum of 10 edges per particle. A smoother representation of the boundary of the particle may significantly affect the response of the system especially at high stress levels and for cases involving angular particles with relatively low fracture strengths.

Other more advanced physics can also be implemented in MASOM which will be helpful to better understanding material behavior. For example:

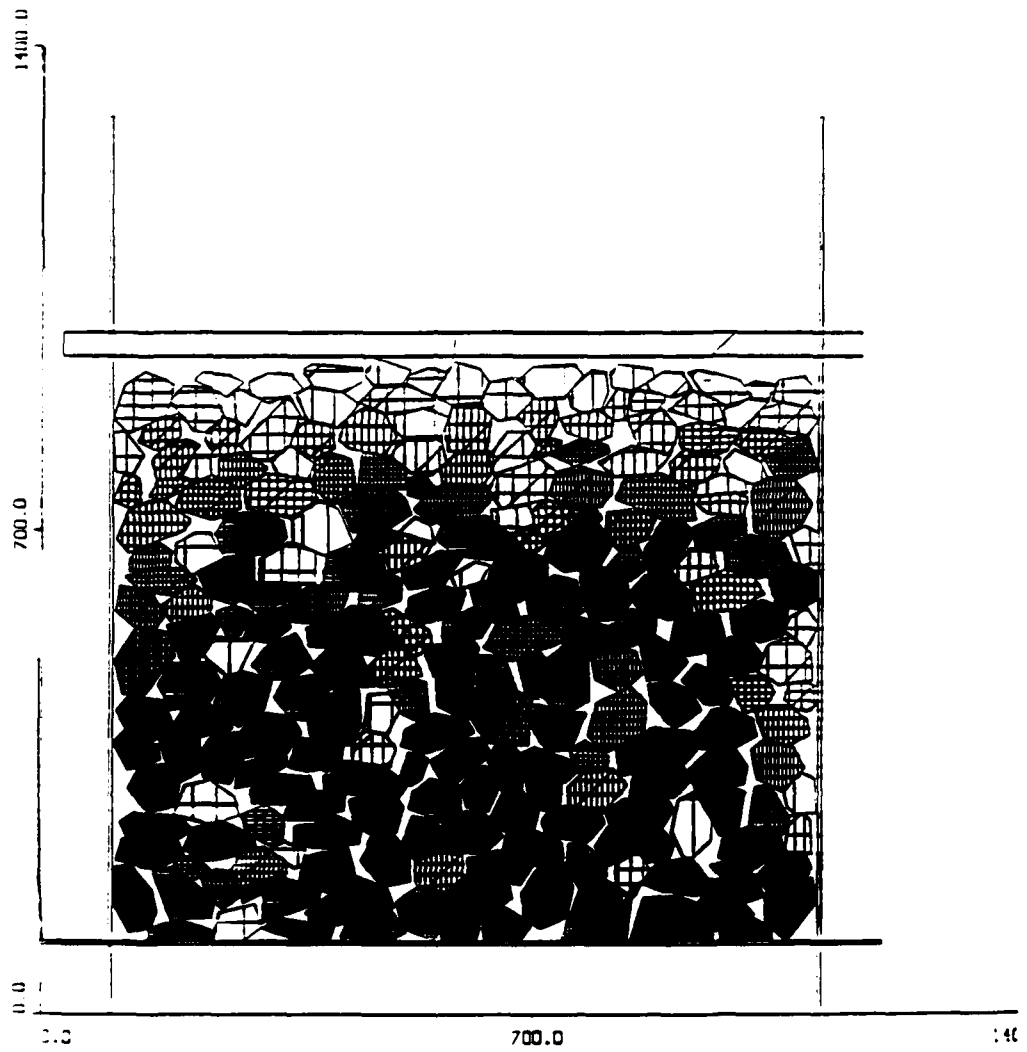
1. *Specification of pressure profile for the boundary conditions.* At this time only point loads can be applied to the boundaries. This limits the shape and form of boundary support, a serious restriction, especially with regard to types of failures where fracture planes or zones extend to the boundaries of the sample, i.e., interact with the boundary conditions.
2. *Motion of fluid flow through the joints and voids.* Two phase flow can be modelled by combining pressure-flow calculation with force-displacements calculation. This research has already begun.
3. *Extension of MASOM from 2D to 3D.* Of course, the real world is three dimensional and it would be very helpful if a discrete element program could be developed for investigating real particles, and more important, 3D particulate assemblies where interstitial behavior (filing from crushed particles, flow to fluids, etc.) is probably significantly different from a 2D model. The primary difficulty is simply managing (i.e., minimizing) the computational burden as polygons become polyhedrons and the contact problem becomes extraordinarily complex.



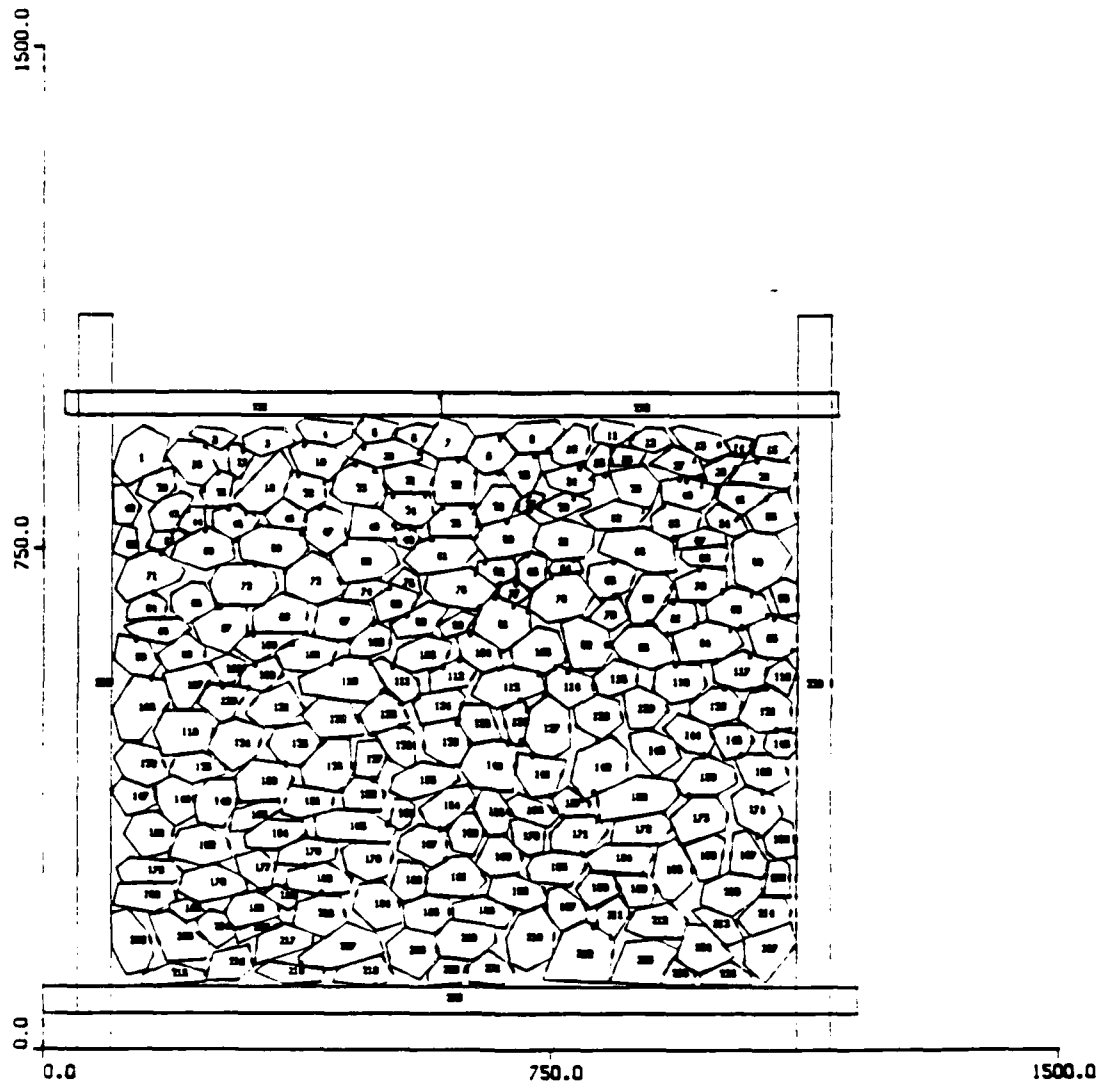
$$R_1 = \left[\frac{A_1}{\pi} \right]^{1/2}$$

$$R_2 = \left[\frac{A_2}{\pi} \right]^{1/2}$$

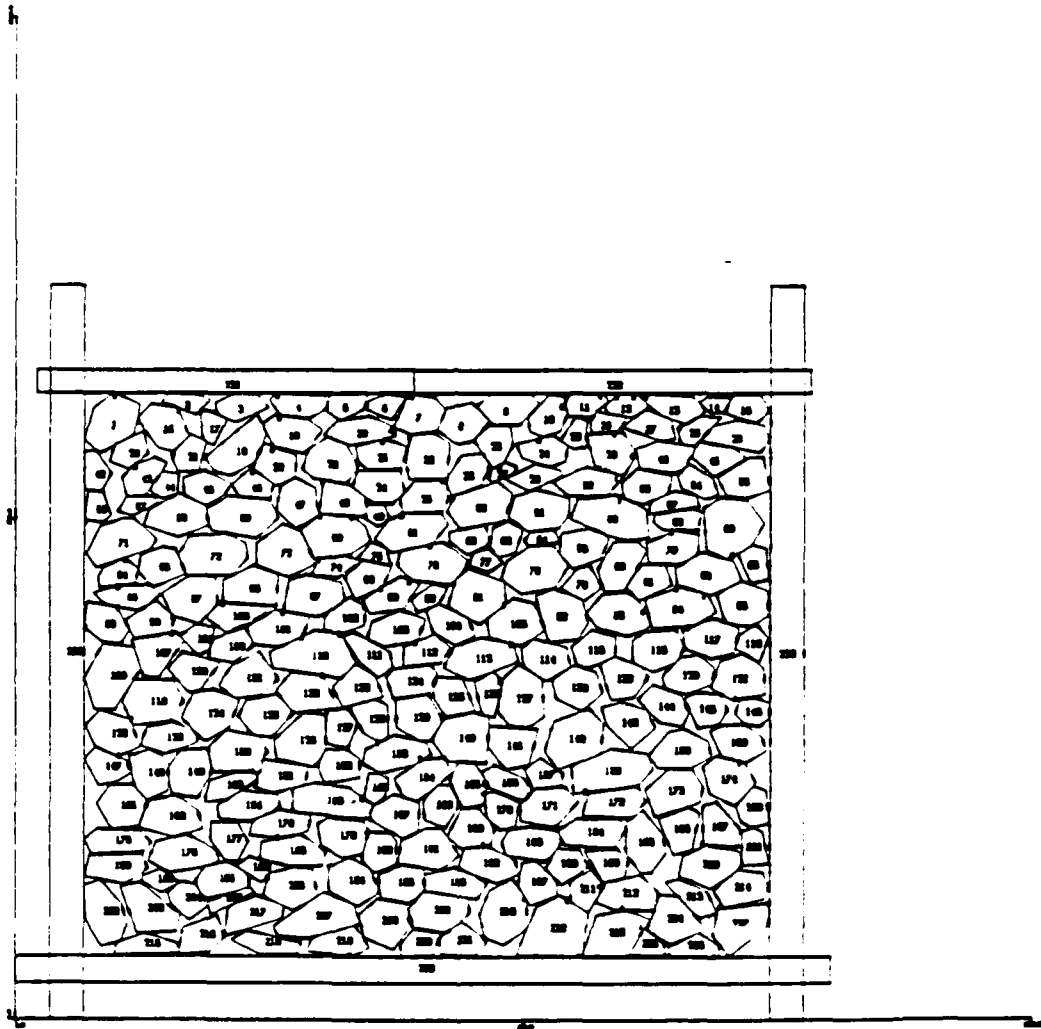
II.1 Grains in Contact



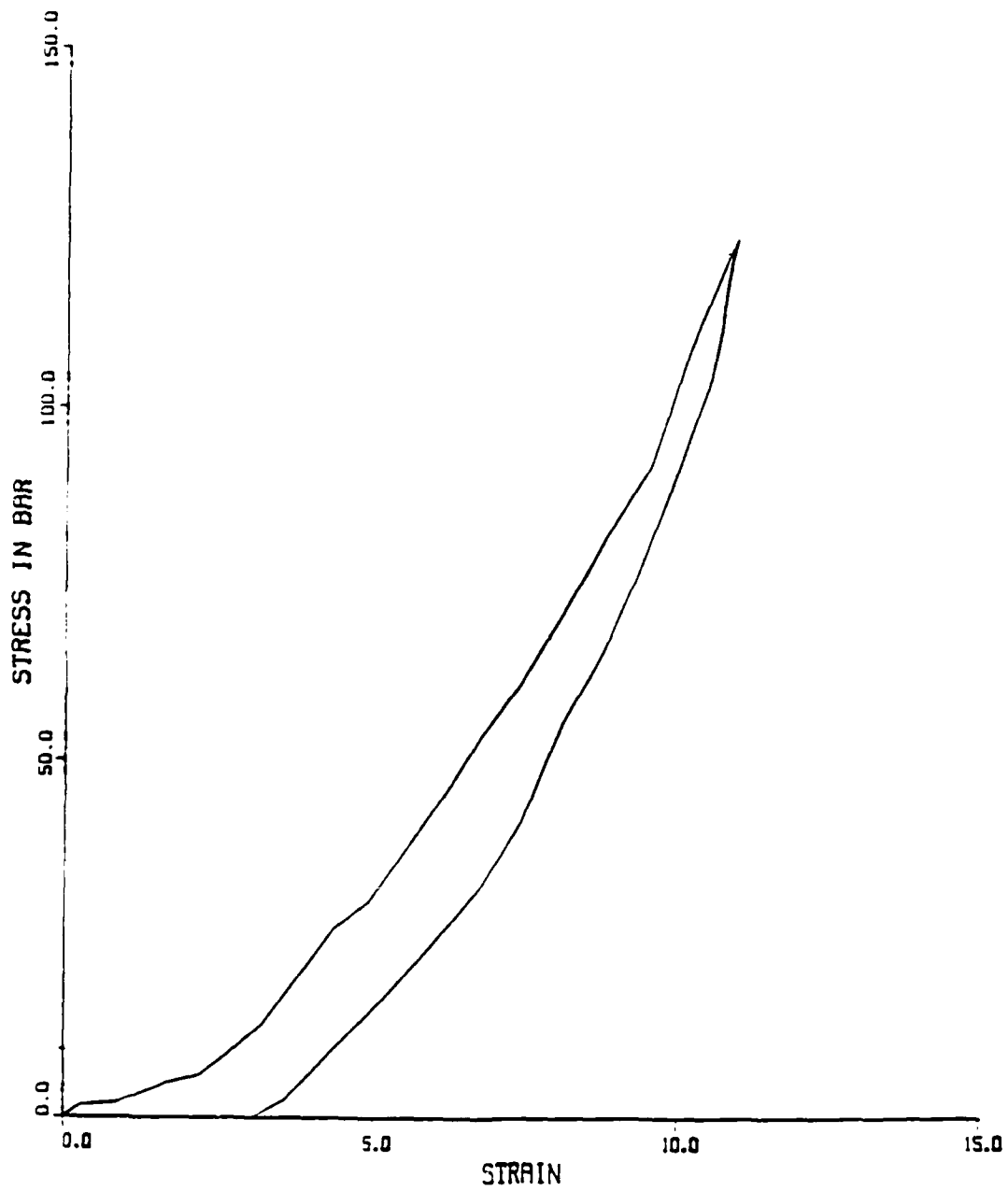
II.3 Stress display inside particle in gravity field.



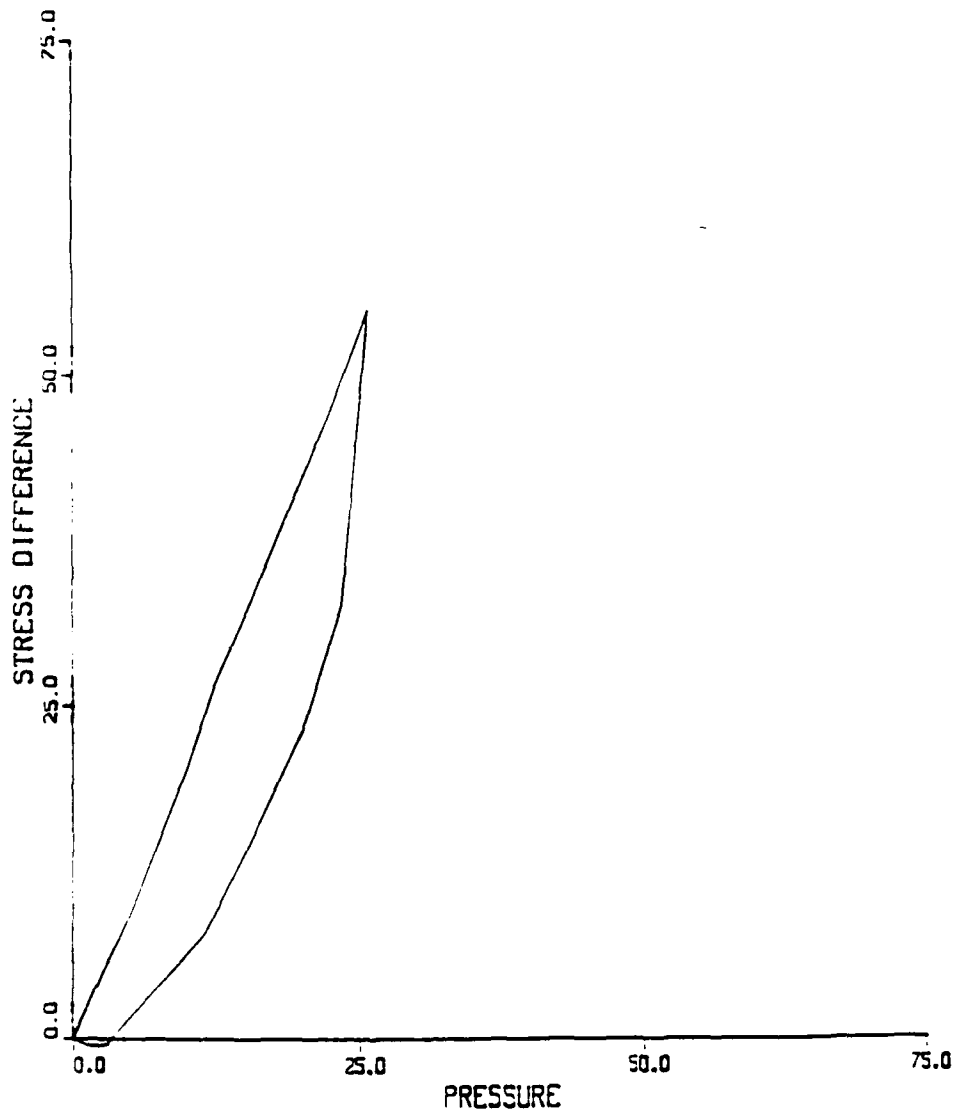
II.4a Uniaxial strain test. Sliding of particles, cycle 800



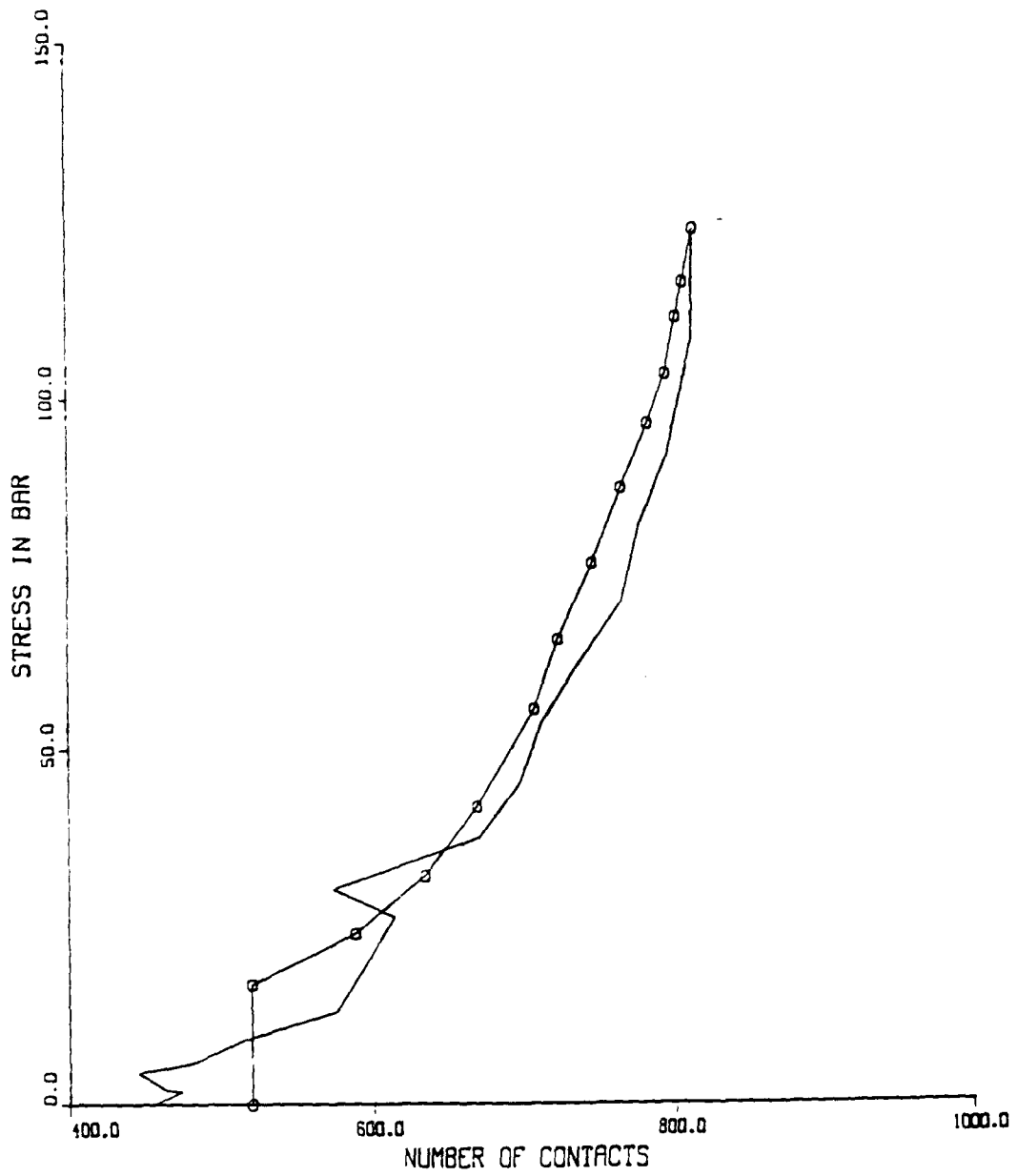
II.4b Uniaxial strain test. Sliding of particles, cycle 1200



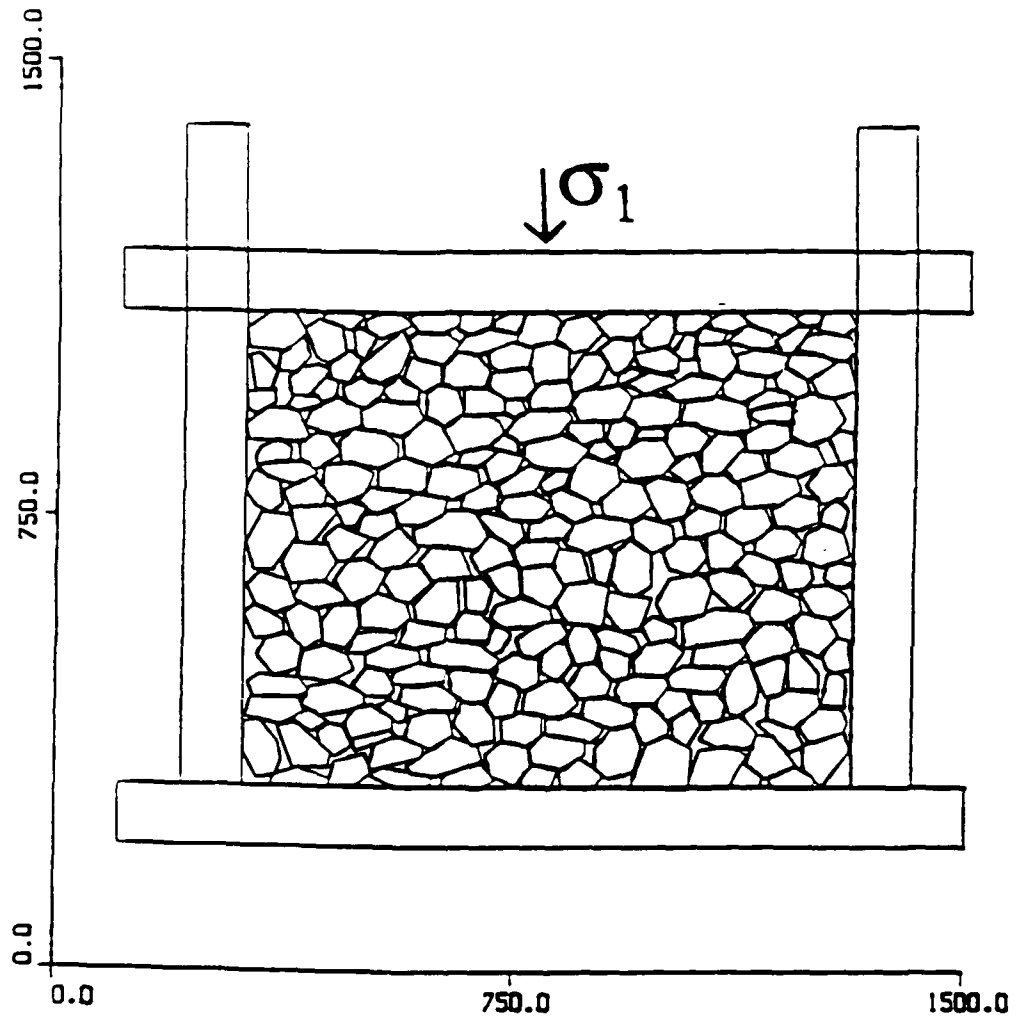
II.5a Uniaxial test without fracture vertical stress versus vertical strain.



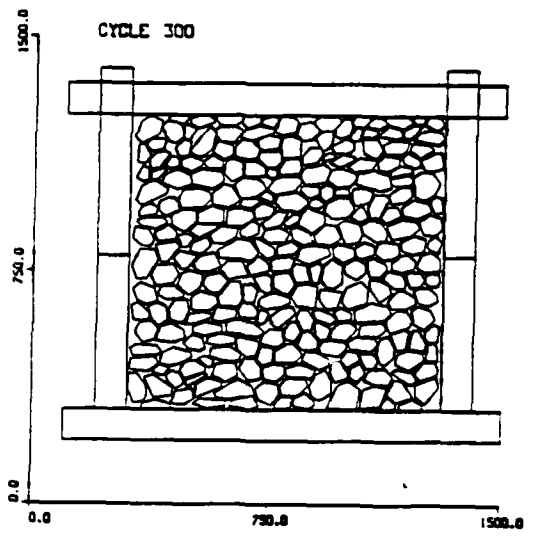
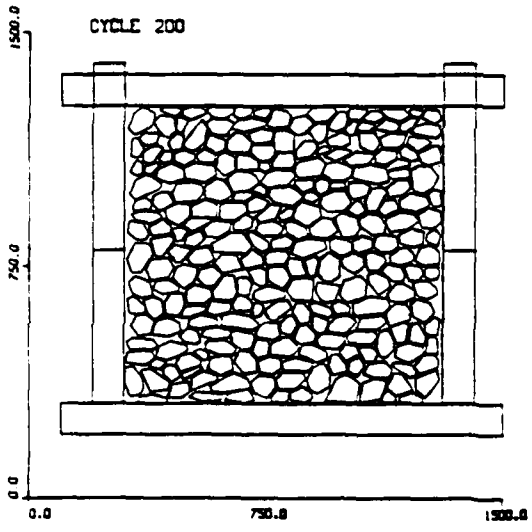
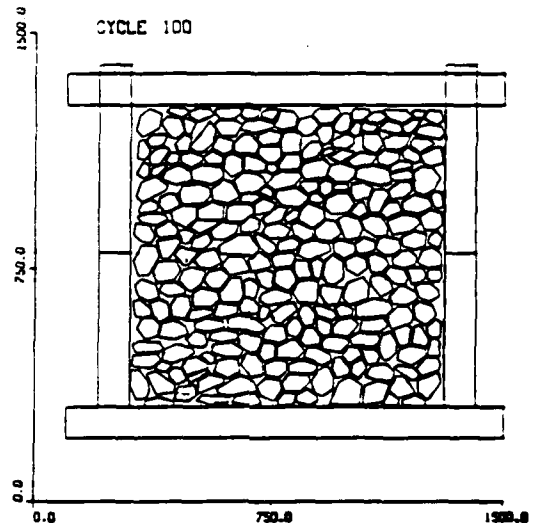
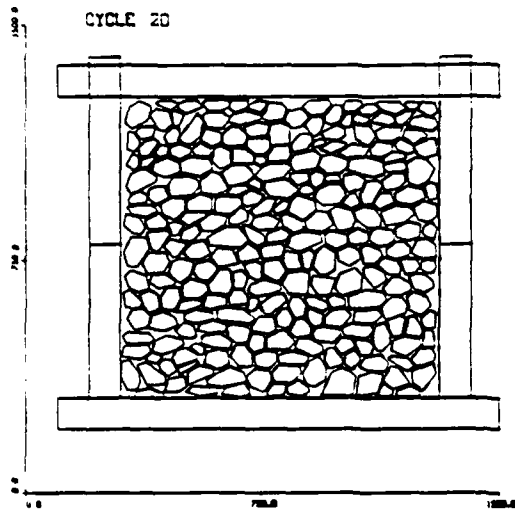
II.6 Uniaxial test: Stress path, deviatoric stress versus pressure.



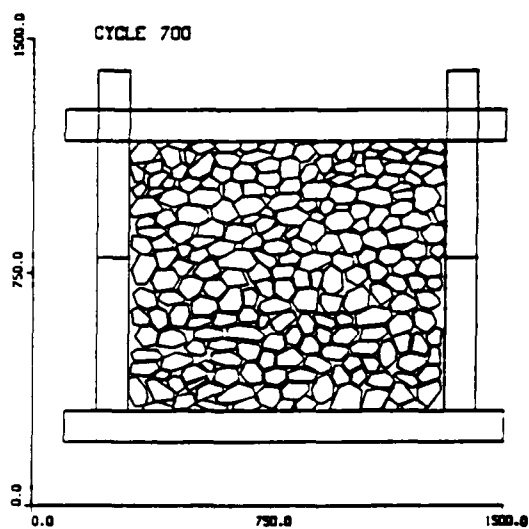
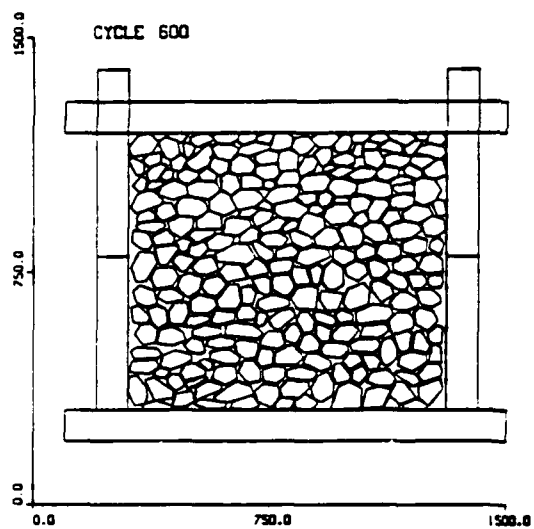
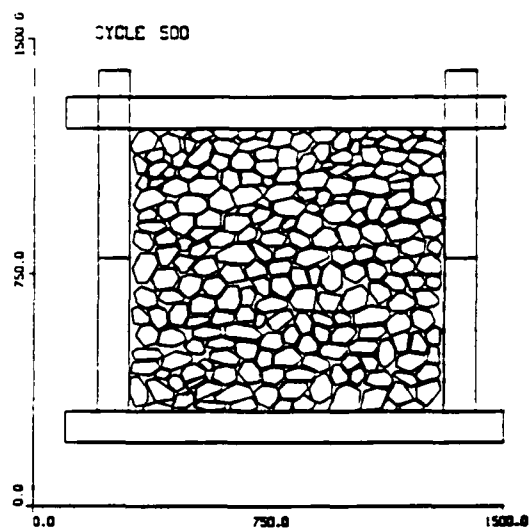
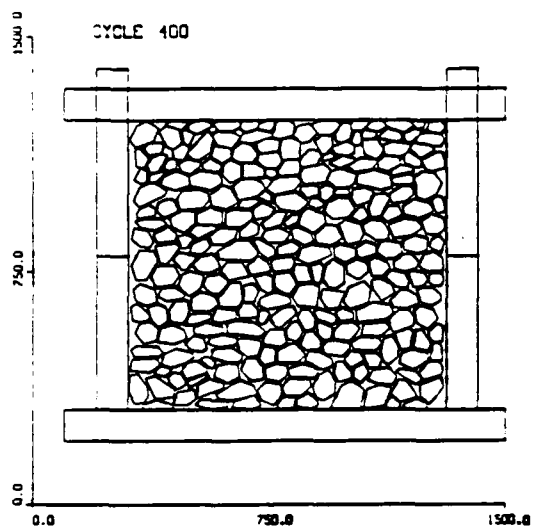
II.7 Uniaxial test. Vertical stress versus total number of contacts.



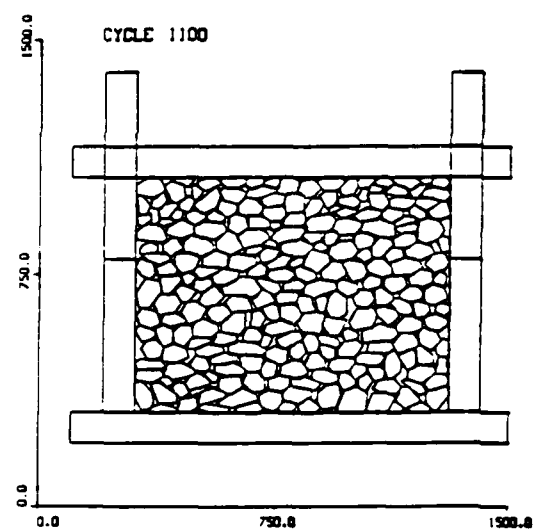
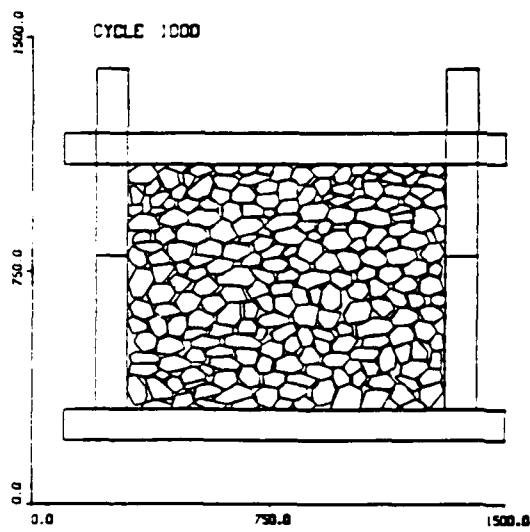
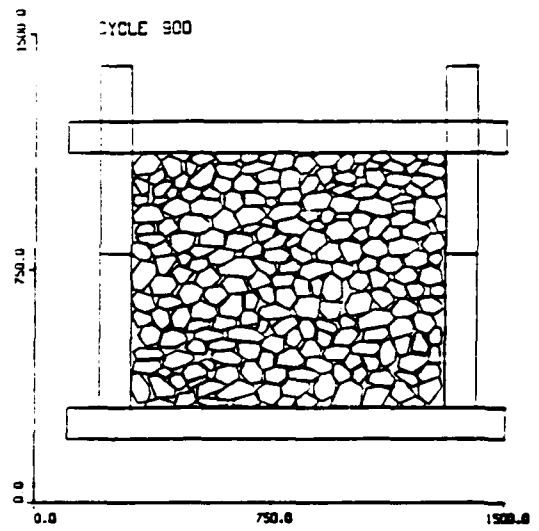
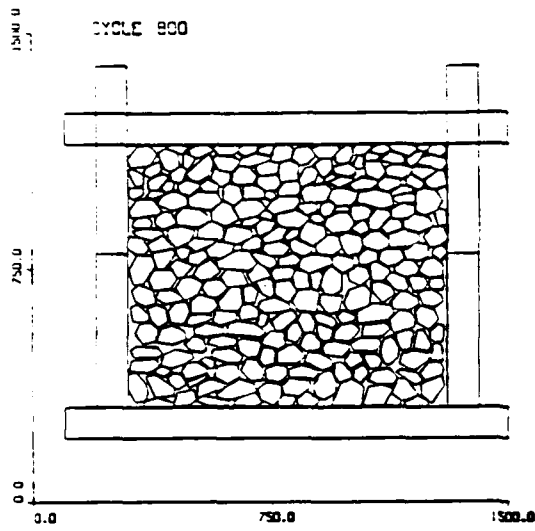
II.8 Uniaxial test with fracture. Computer model.



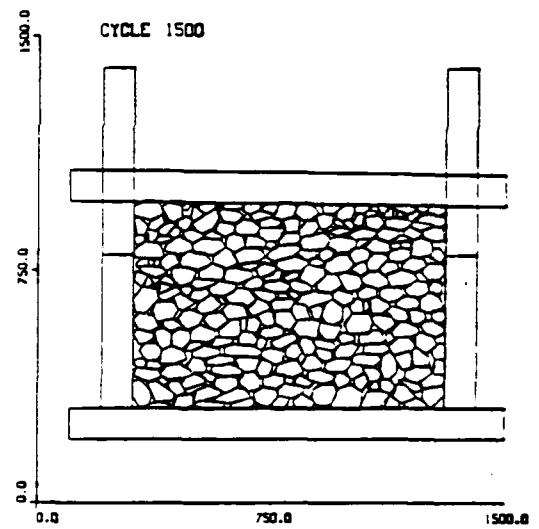
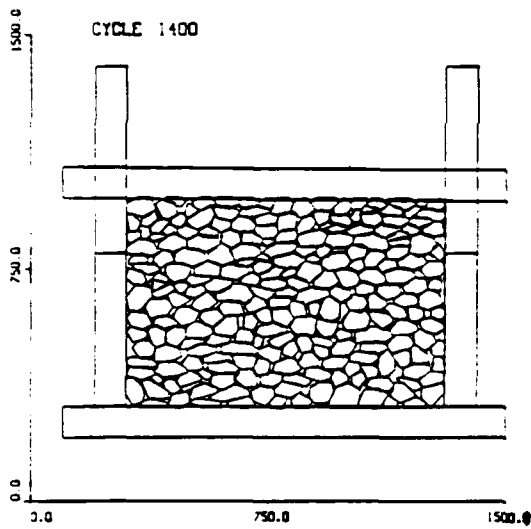
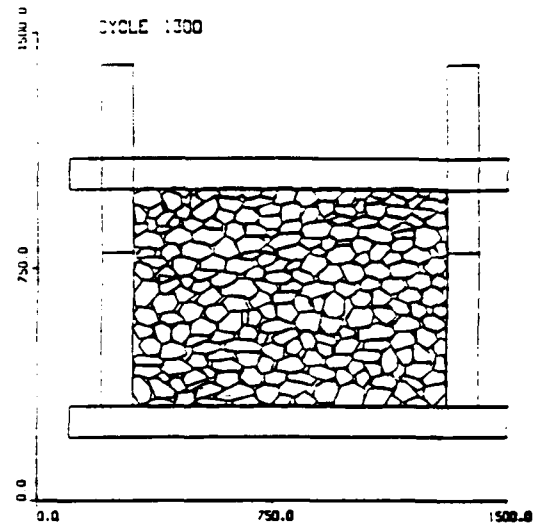
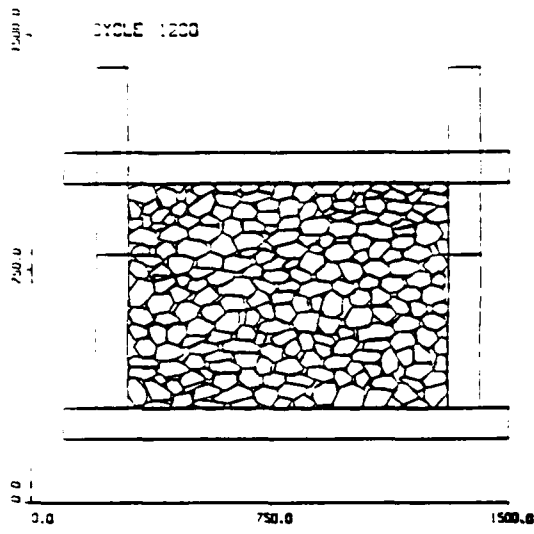
II.9 Uniaxial test simulation, $0 \text{ bar} < \sigma_1 < 1 \text{ bar}$



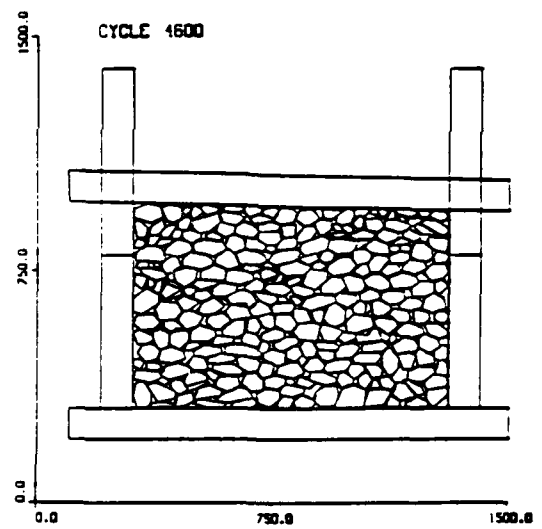
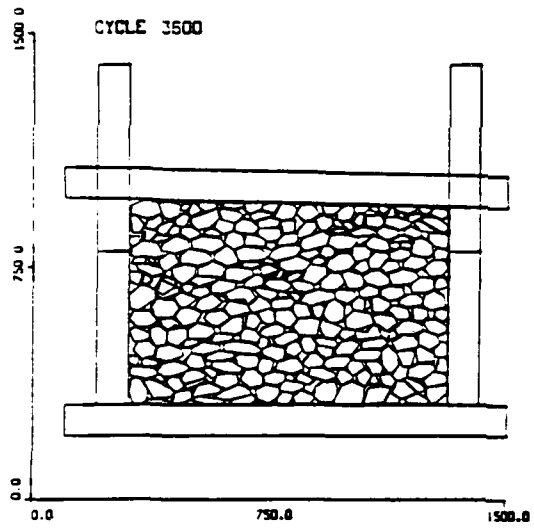
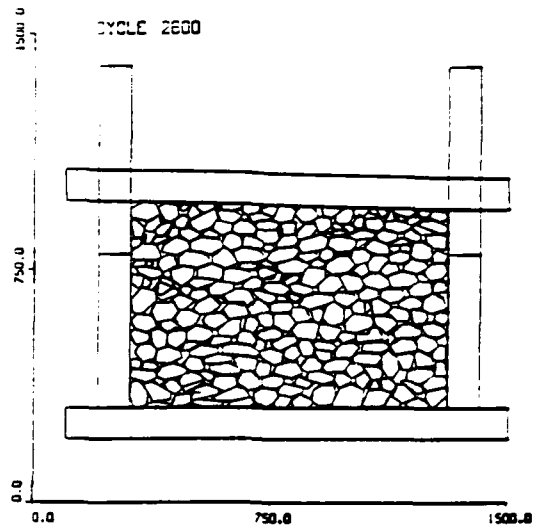
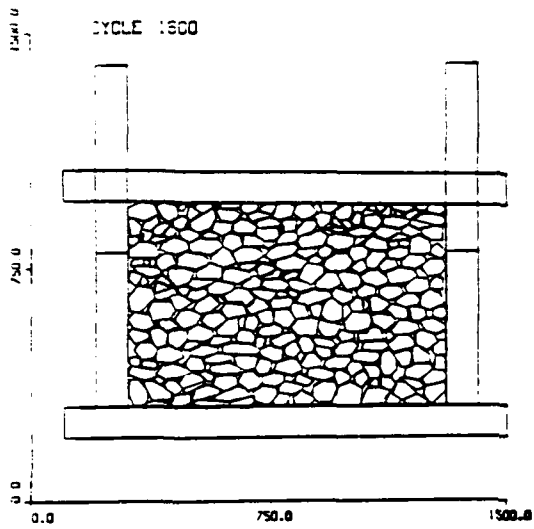
II.10 Uniaxial test simulation, $2 \text{ bar} < \sigma_1 < 10 \text{ bar}$



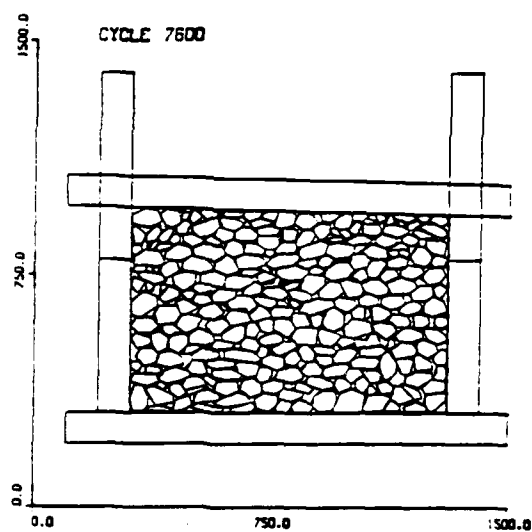
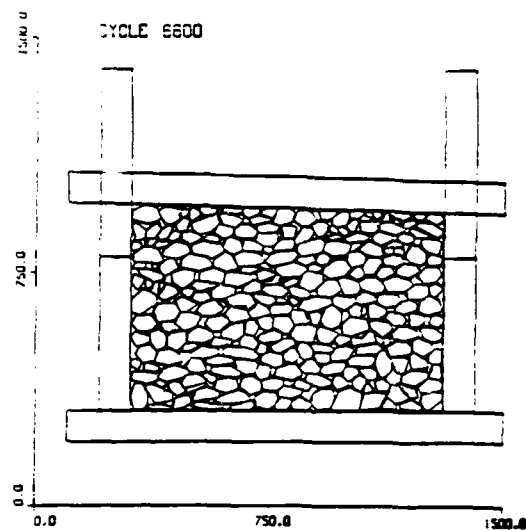
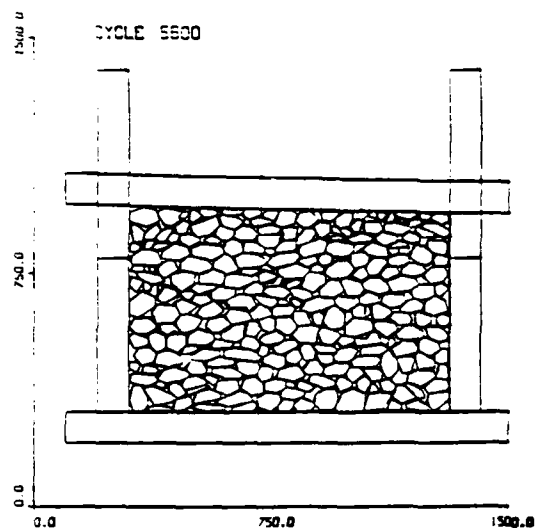
II.11 Uniaxial test simulation, $15 \text{ bar} < \sigma_1 < 80 \text{ bar}$



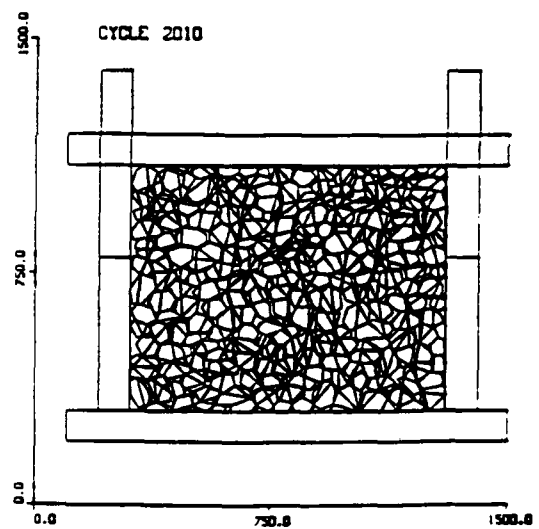
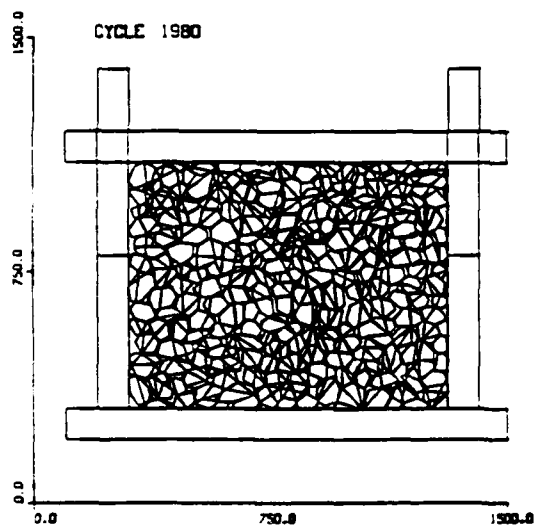
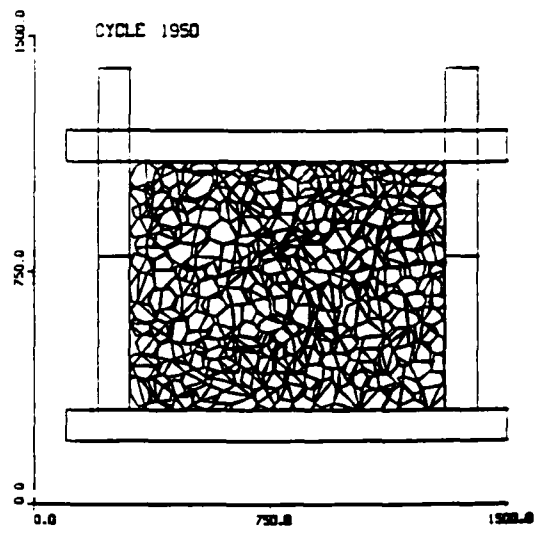
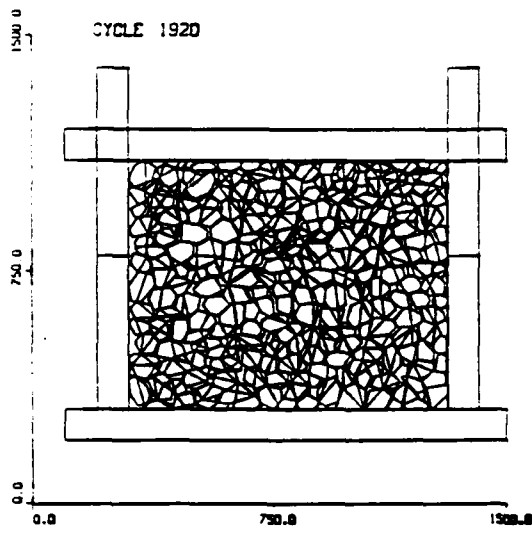
II.12 Uniaxial test simulation, $90 \text{ bar} < \sigma_1 < 150 \text{ bar}$



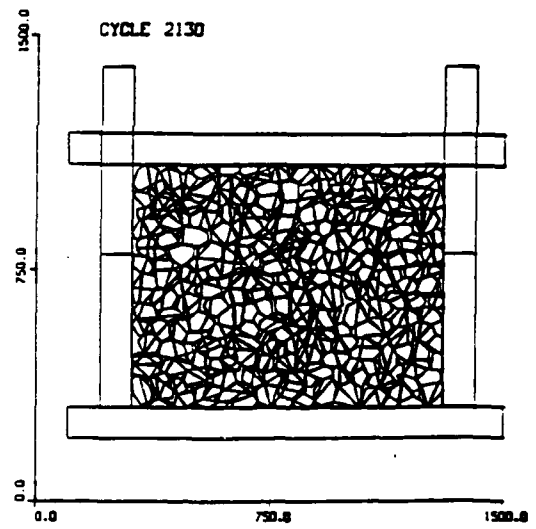
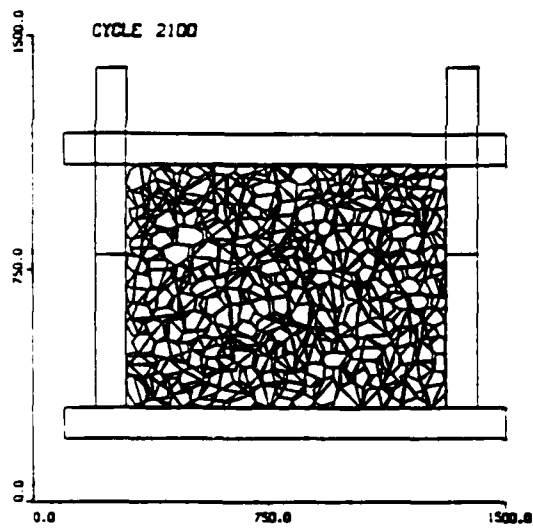
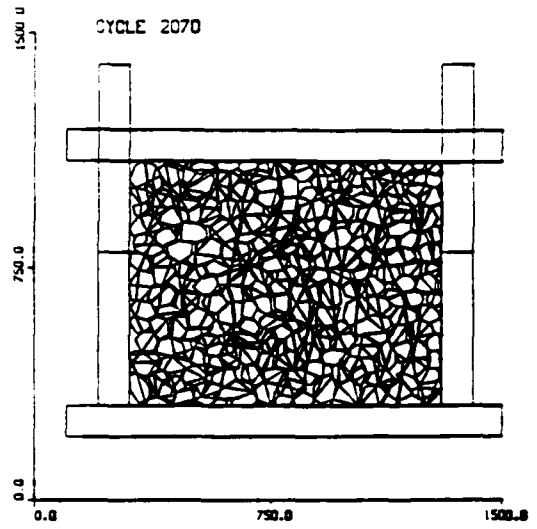
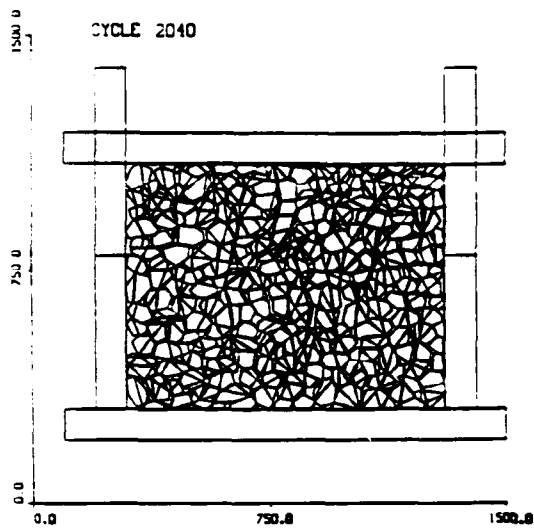
II.13 Uniaxial test simulation, $90 \text{ bar} < \sigma_1 < 120 \text{ bar}$



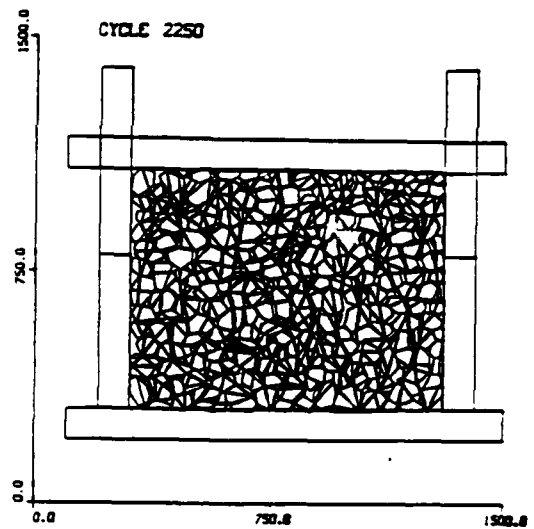
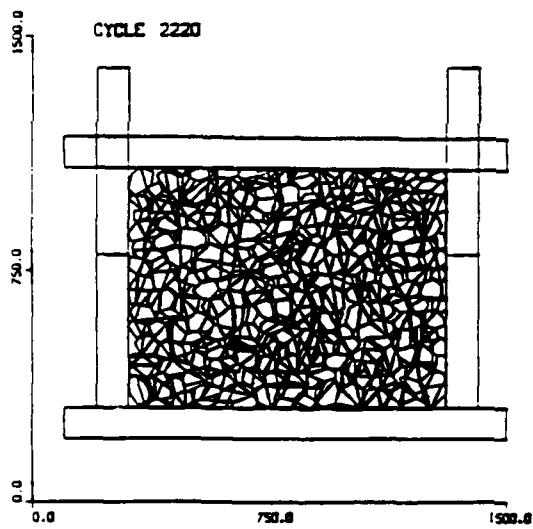
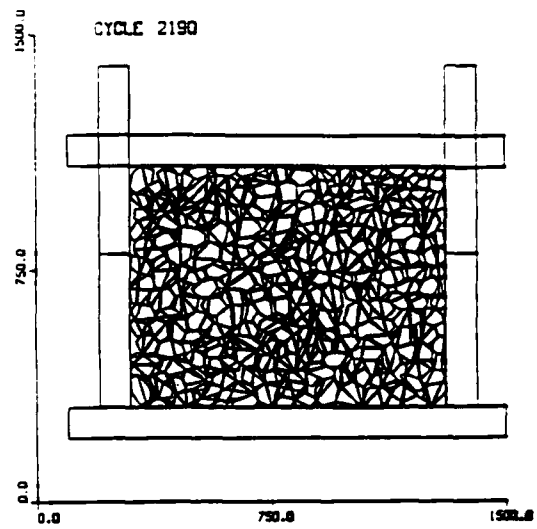
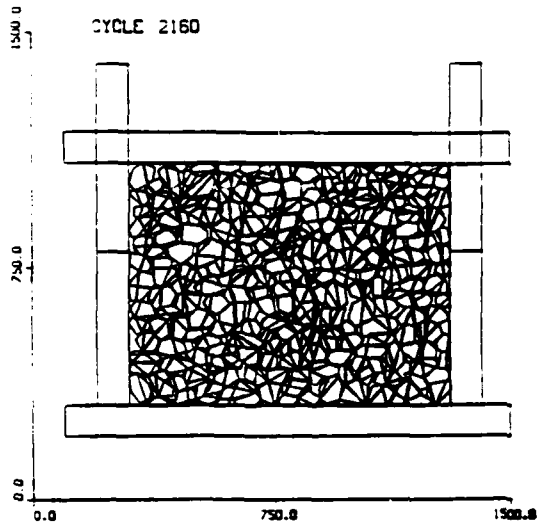
II.14 Uniaxial test simulation, $30 \text{ bar} < \sigma_1 < 70 \text{ bar}$



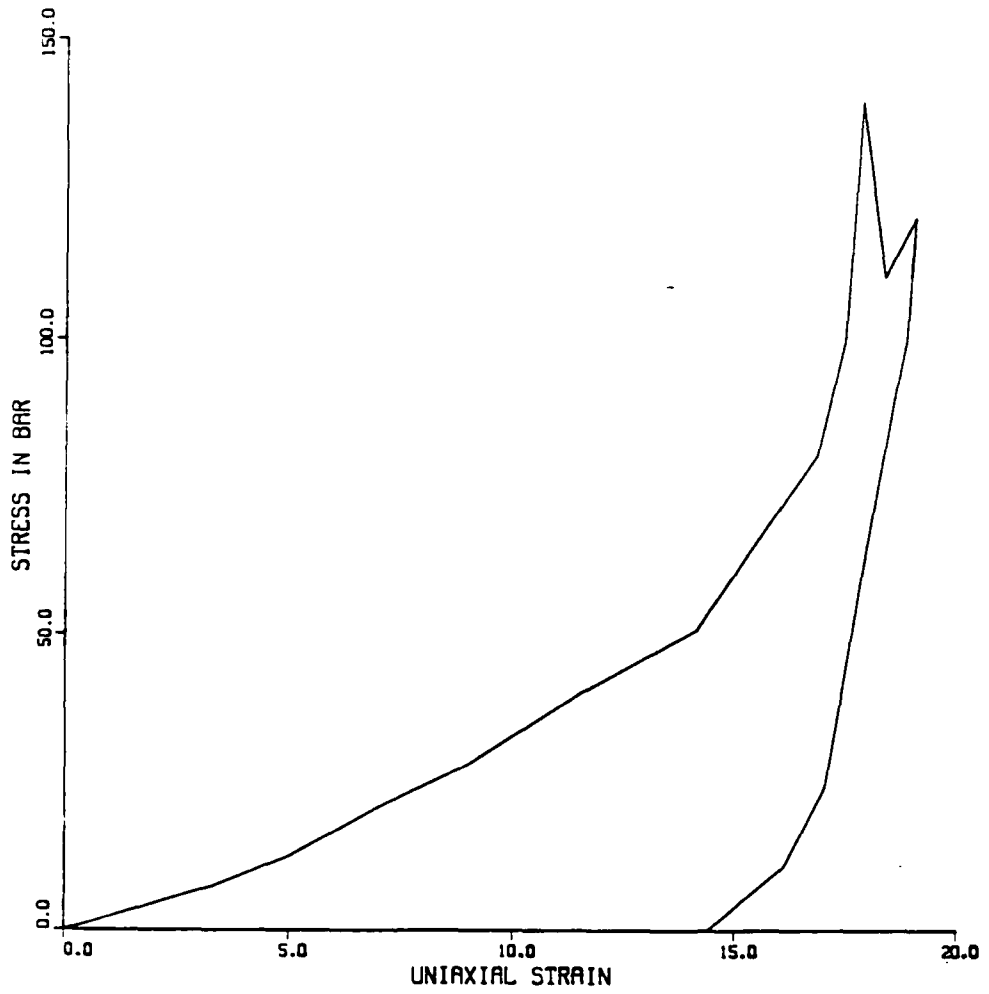
II.15 Uniaxial test simulation. Contact force display
cycle 1920-2010



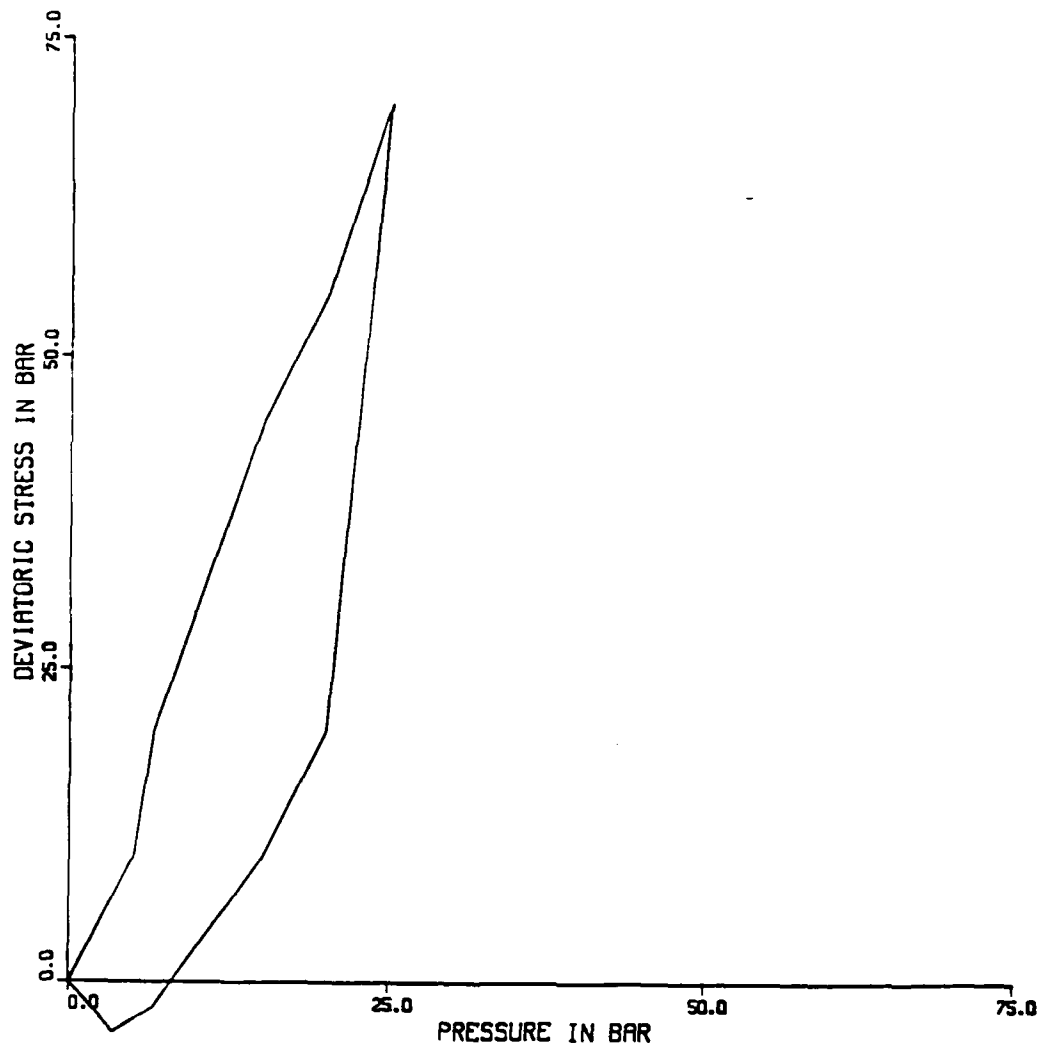
II.16 Uniaxial test simulation. Contact force display
cycle 2040-2130



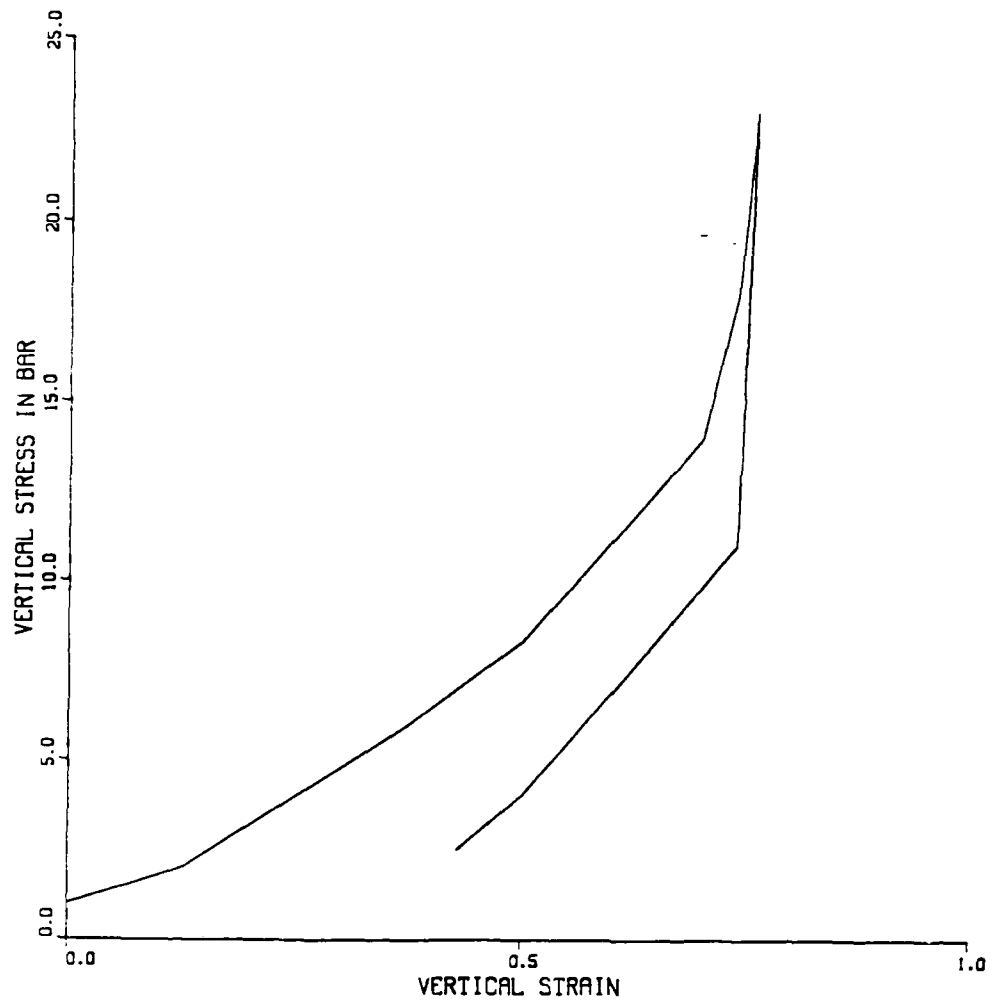
II.17 Uniaxial test simulation. Contact force display
cycle 2160-2250



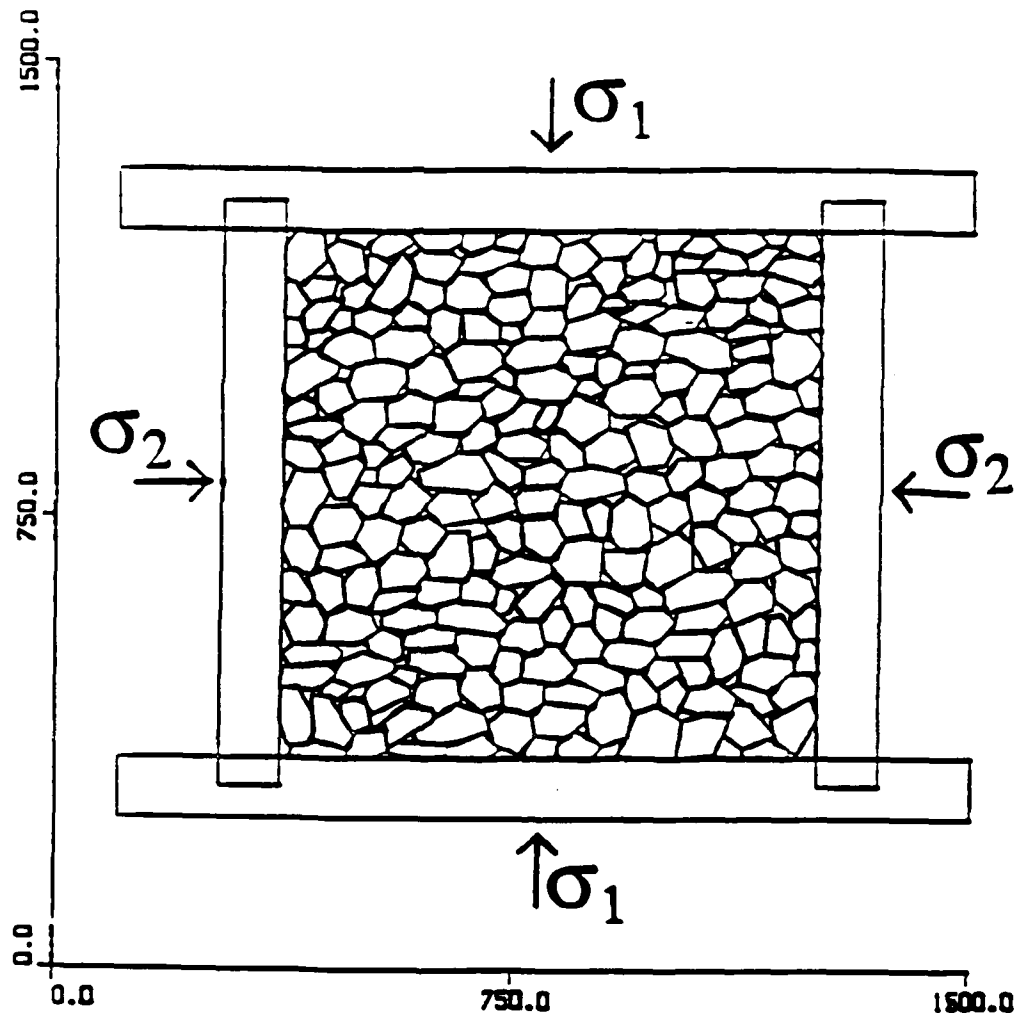
II.18 Uniaxial test with fracture. Vertical stress versus uniaxial strain.



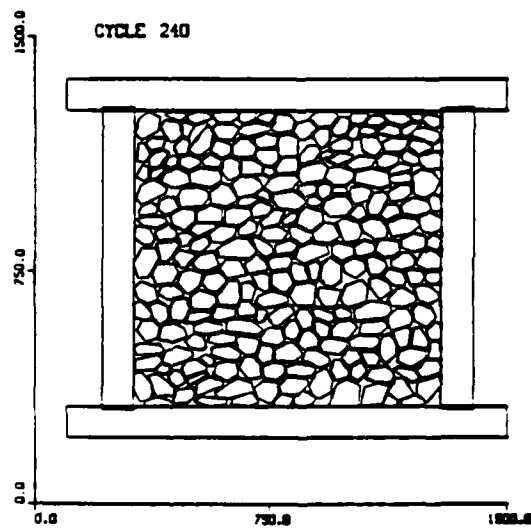
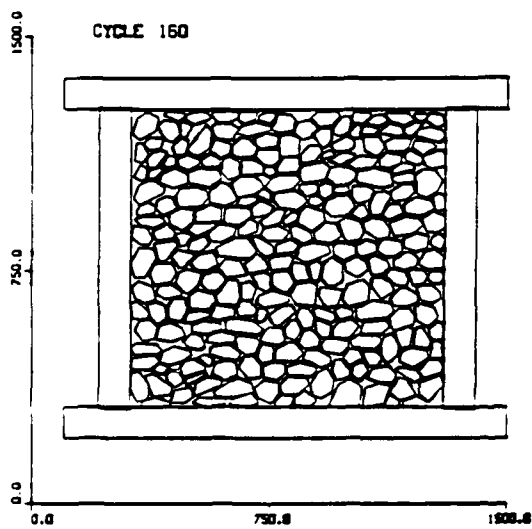
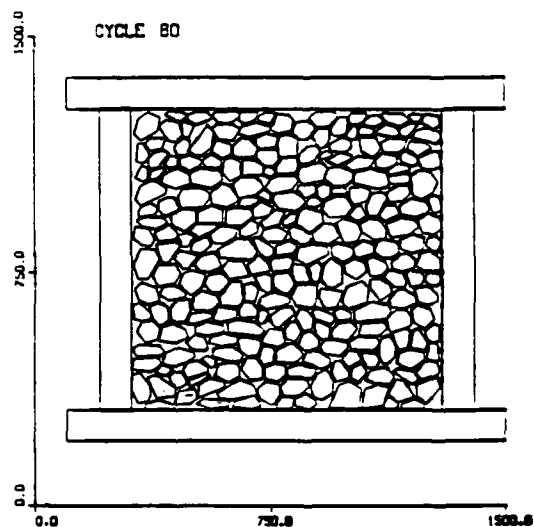
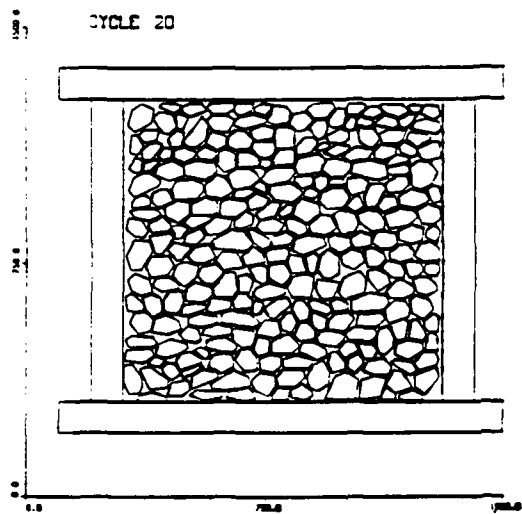
II.19 Uniaxial test with fracture. Deviatoric stress versus pressure.



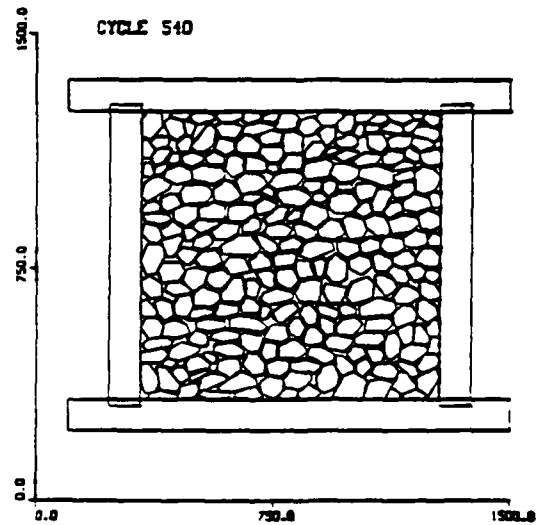
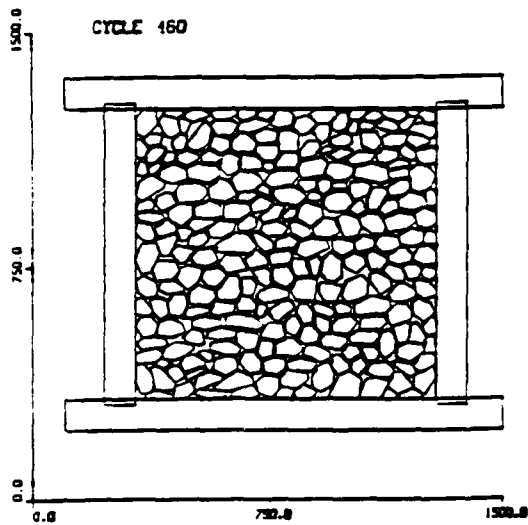
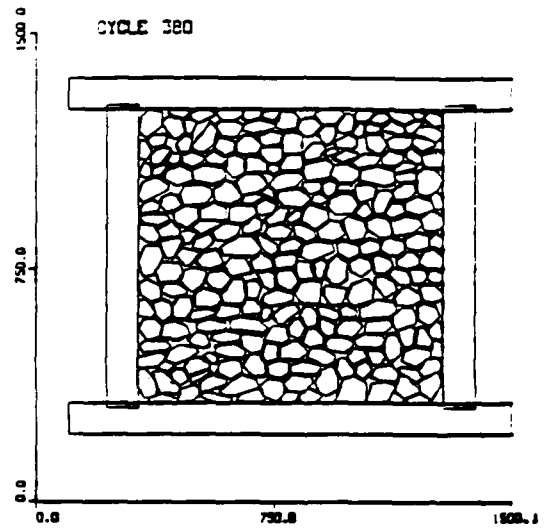
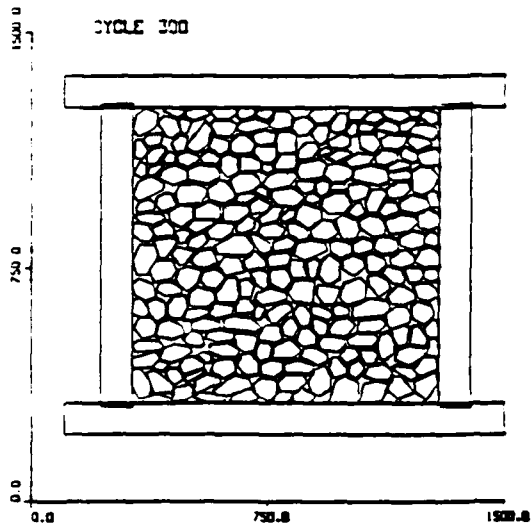
II.20 Uniaxial test (Lab Experiment). Vertical stress versus vertical strain.



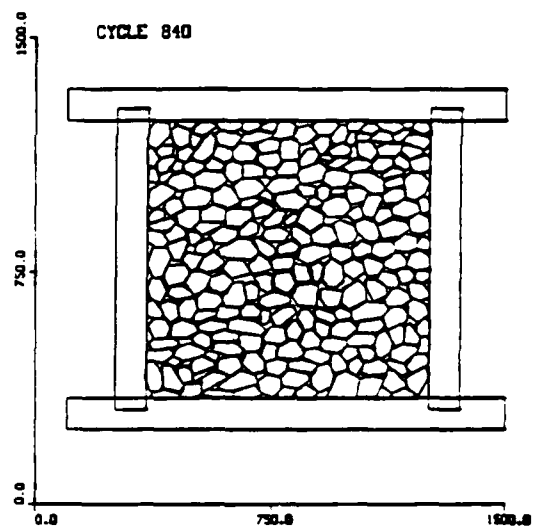
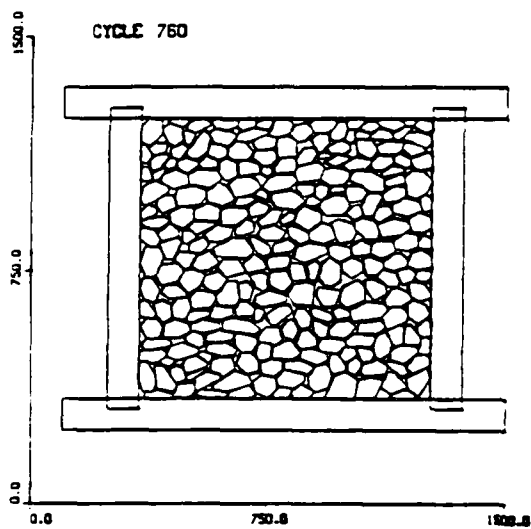
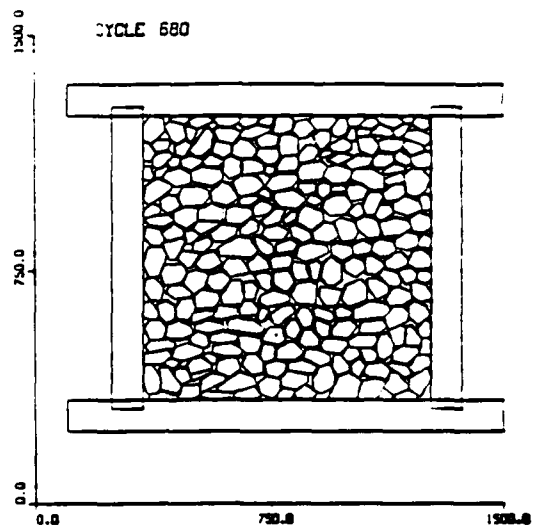
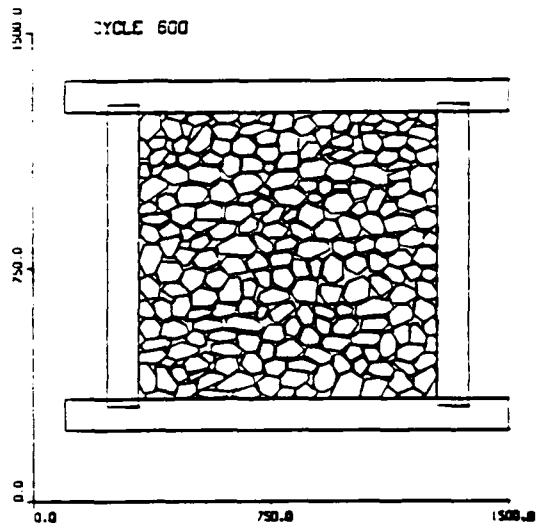
II.21 Triaxial test simulation. Computer model.



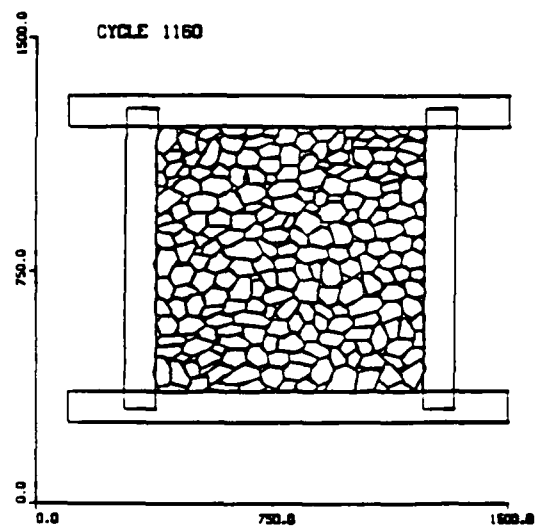
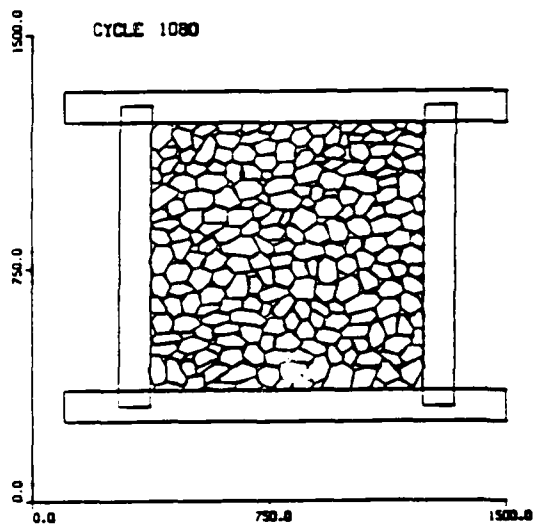
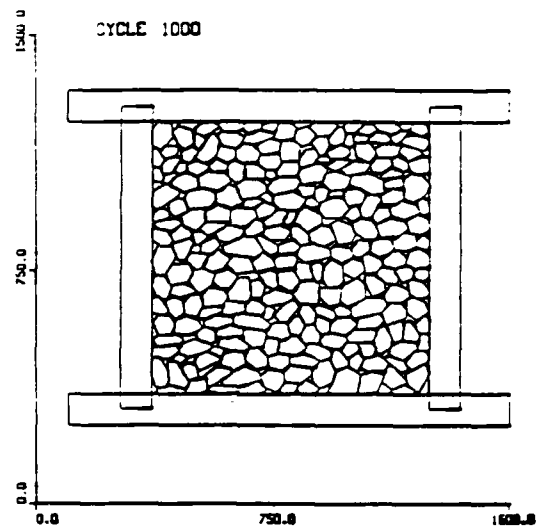
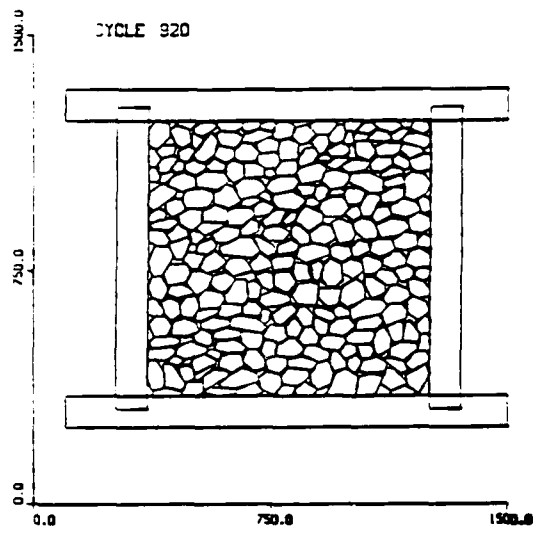
II.22 Triaxial test simulation, $0 \text{ bar} < \sigma_1 < 5 \text{ bar}$, $0 \text{ bar} < \sigma_2 < 5 \text{ bar}$



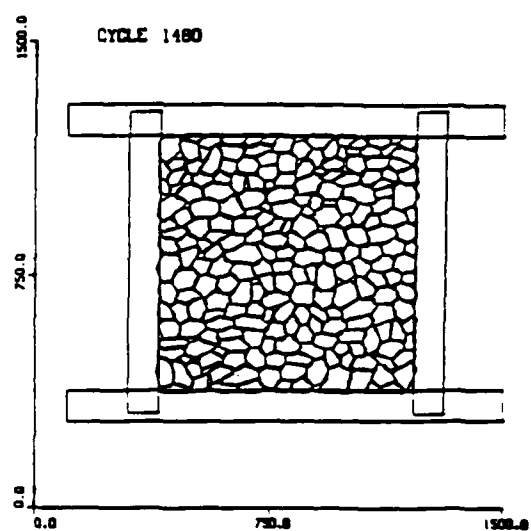
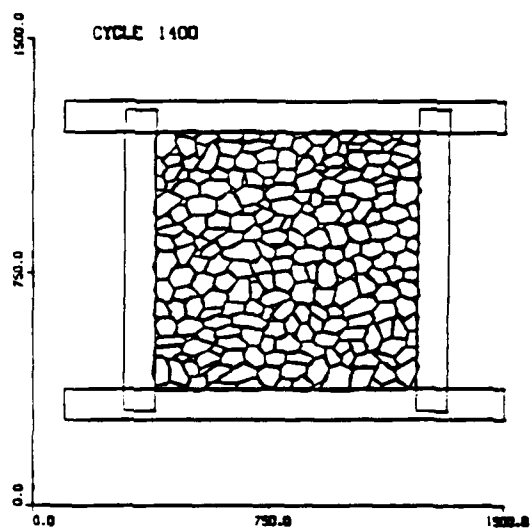
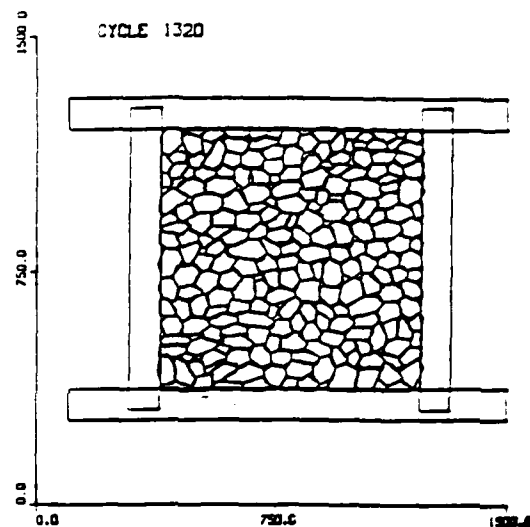
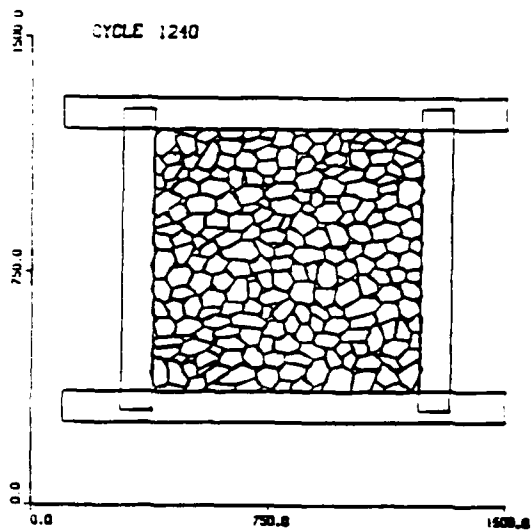
II.23 Triaxial test simulation, $5 \text{ bar} < \sigma_1 < 10 \text{ bar}$, $5 \text{ bar} < \sigma_2 < 10 \text{ bar}$



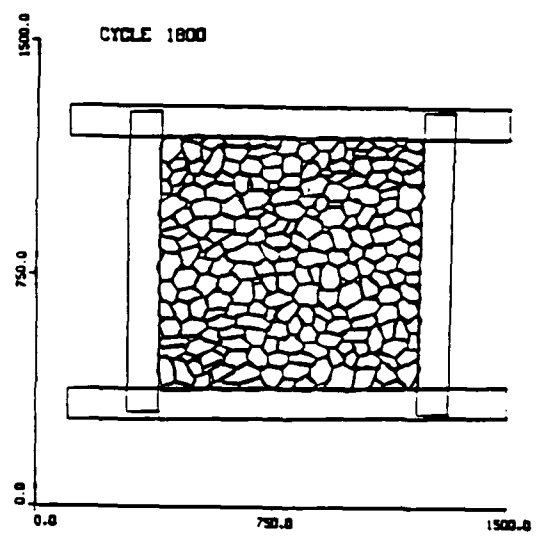
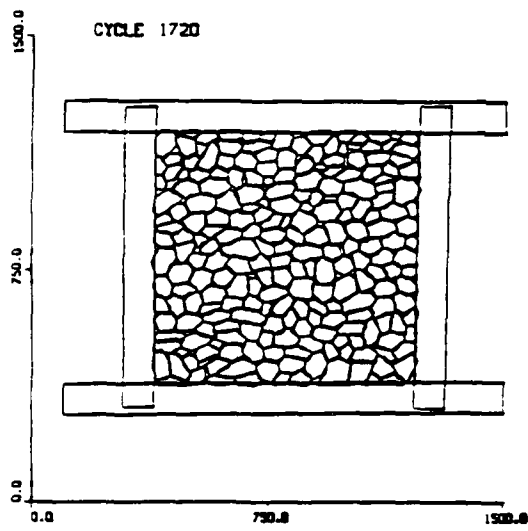
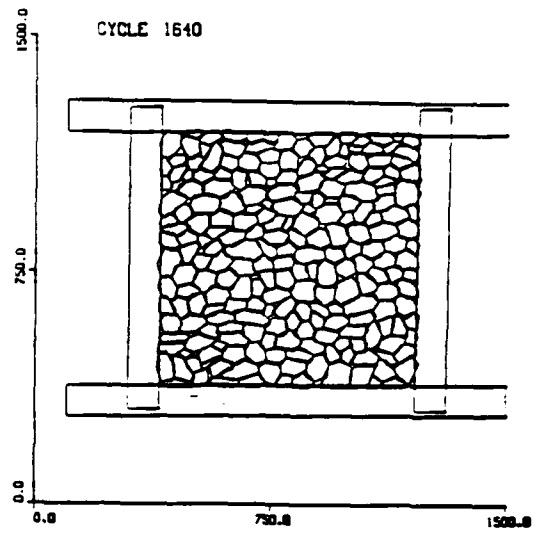
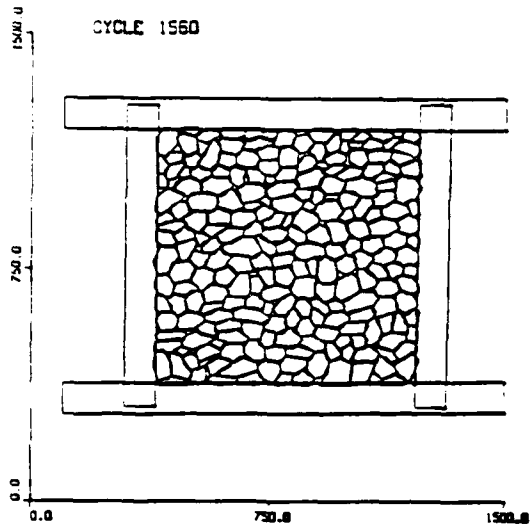
II.24 Triaxial test simulation, $10 \text{ bar} < \sigma_1 < 20 \text{ bar}$, $10 \text{ bar} < \sigma_2 < 20 \text{ bar}$
bar



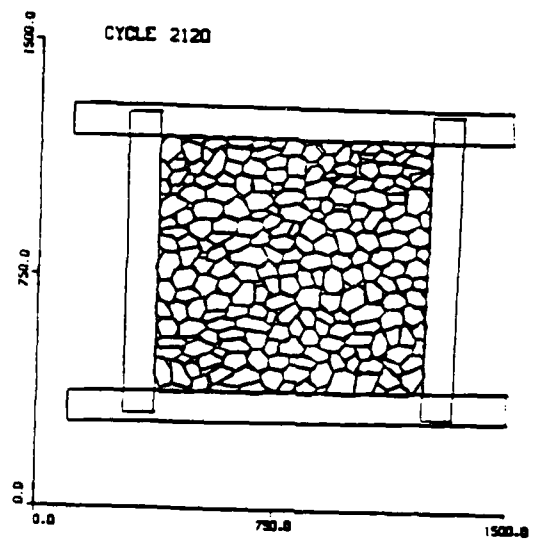
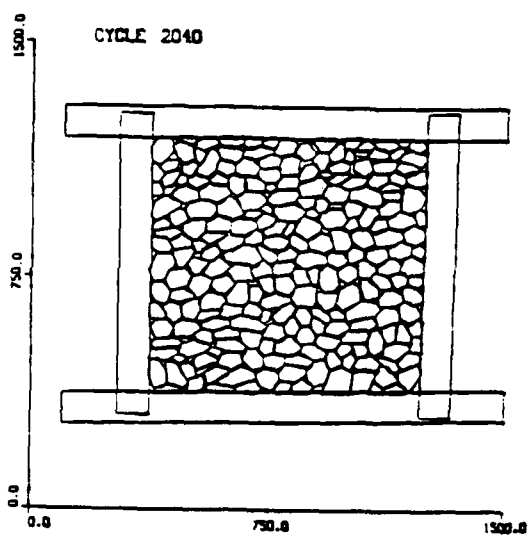
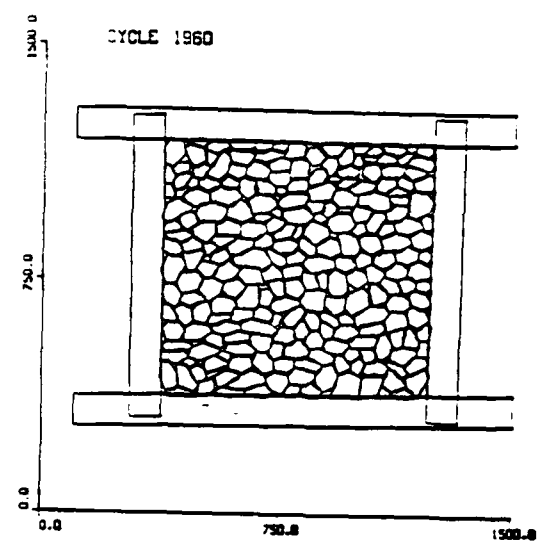
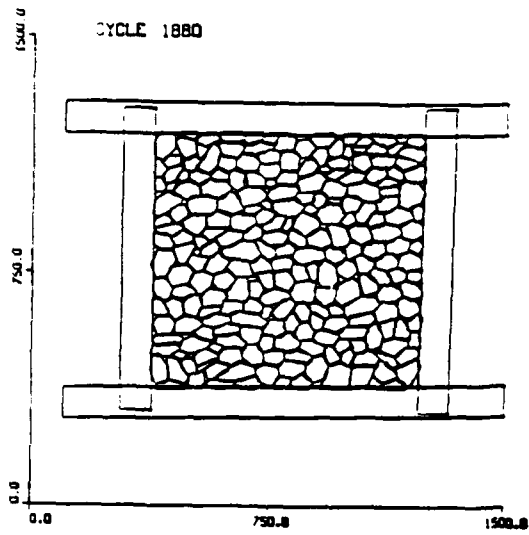
II.25 Triaxial test simulation, $20 \text{ bar} < \sigma_1 < 30 \text{ bar}$, $20 \text{ bar} < \sigma_2 < 30 \text{ bar}$
bar



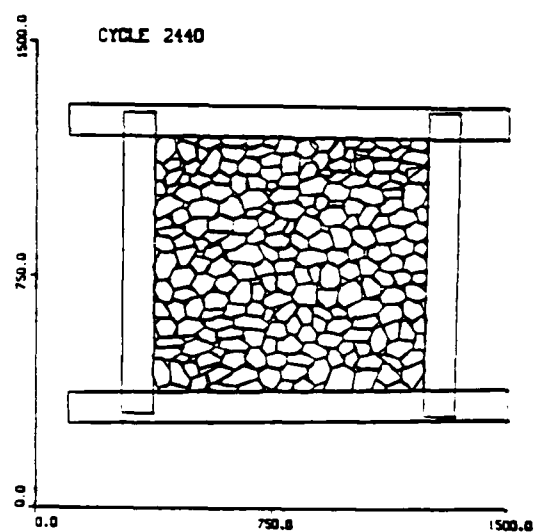
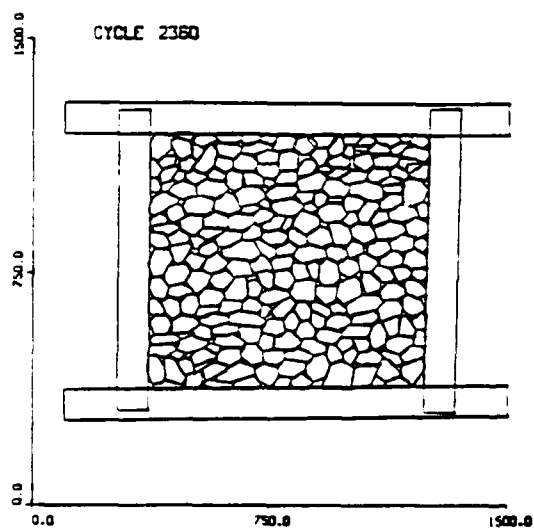
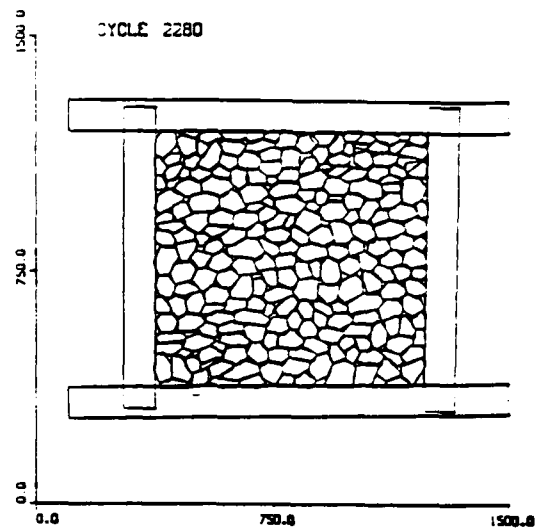
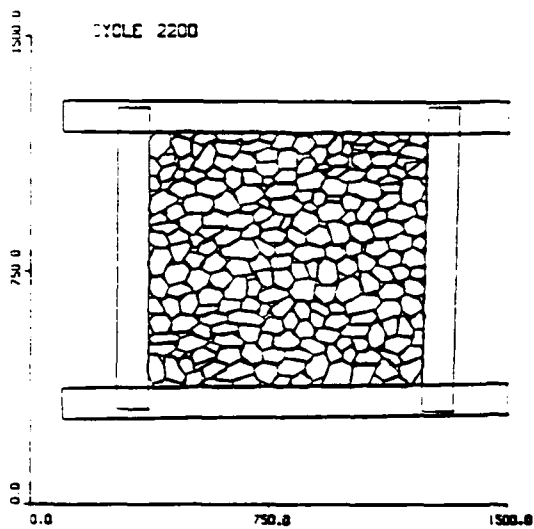
II.26 Triaxial test simulation, $30 \text{ bar} < \sigma_1 < 50 \text{ bar}$, $30 \text{ bar} < \sigma_2 < 50 \text{ bar}$



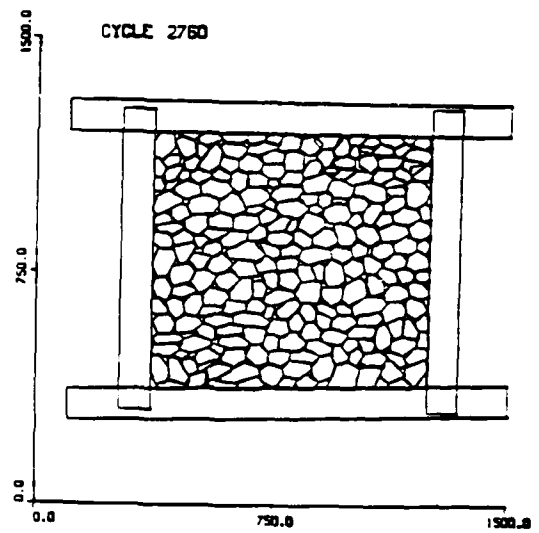
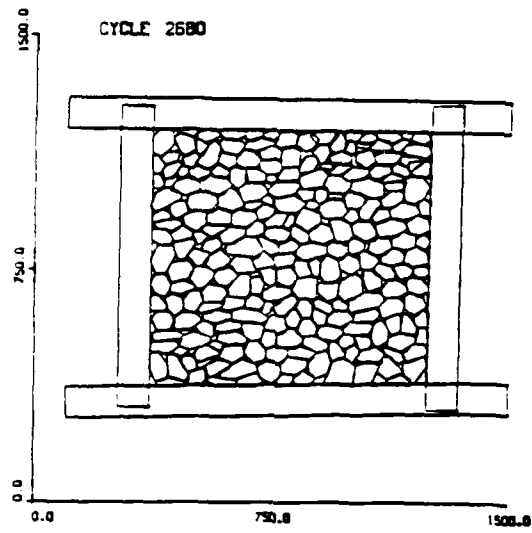
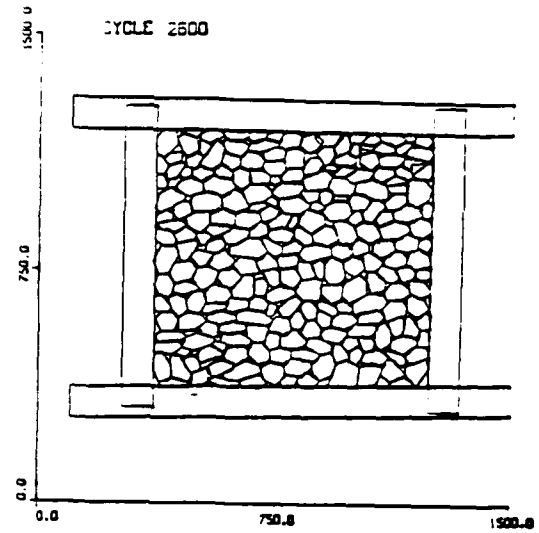
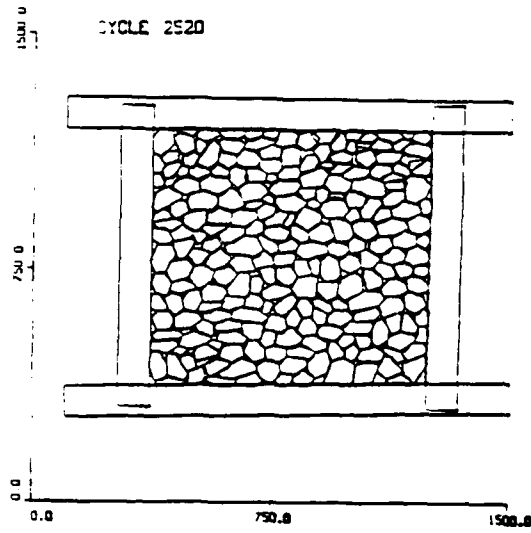
II.27 Triaxial test simulation, $50 \text{ bar} < \sigma_1 < 70 \text{ bar}$, $\sigma_2 = 50 \text{ bar}$



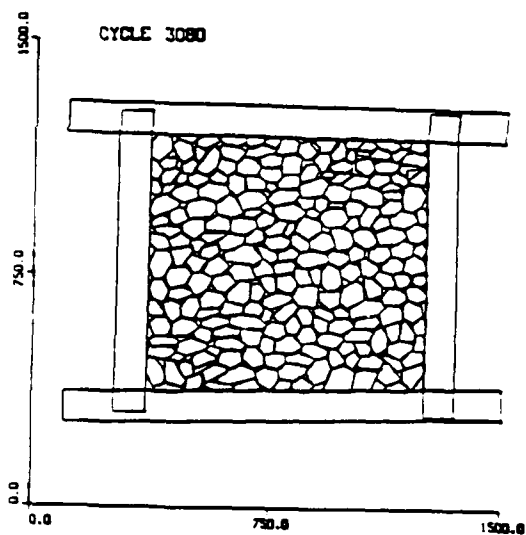
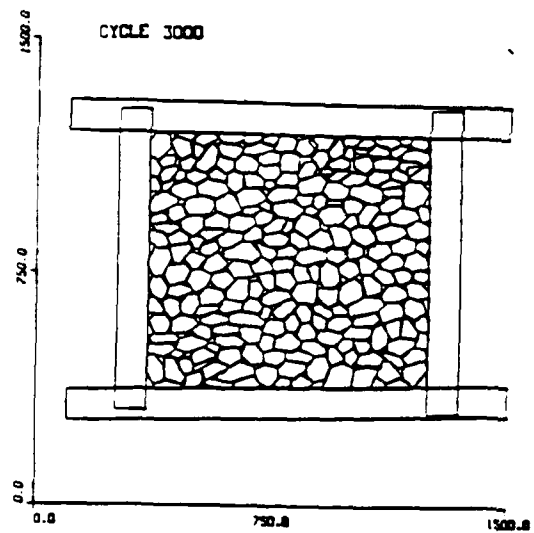
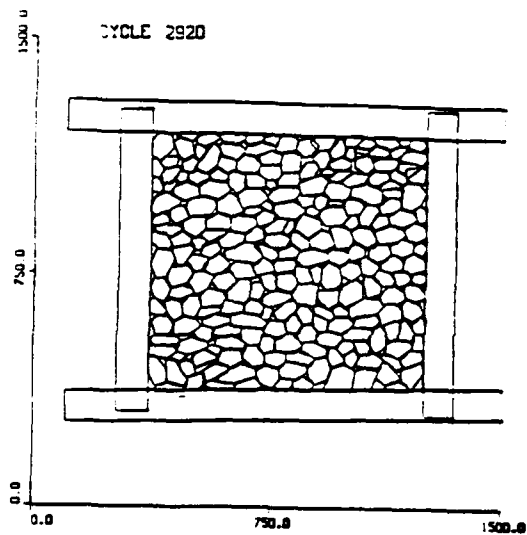
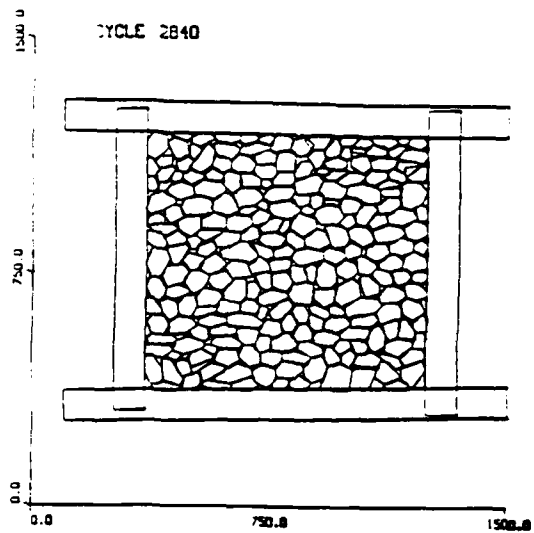
II.28 Triaxial test simulation, $70 \text{ bar} < \sigma_1 < 90 \text{ bar}$, $\sigma_2 = 50 \text{ bar}$



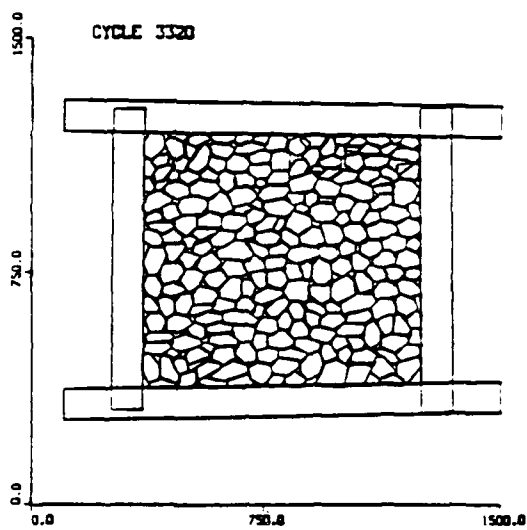
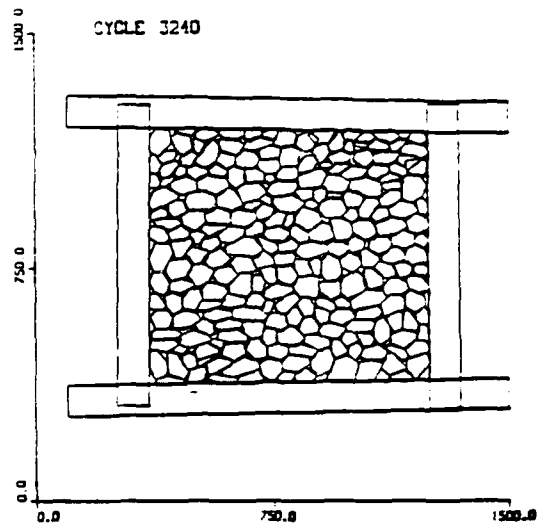
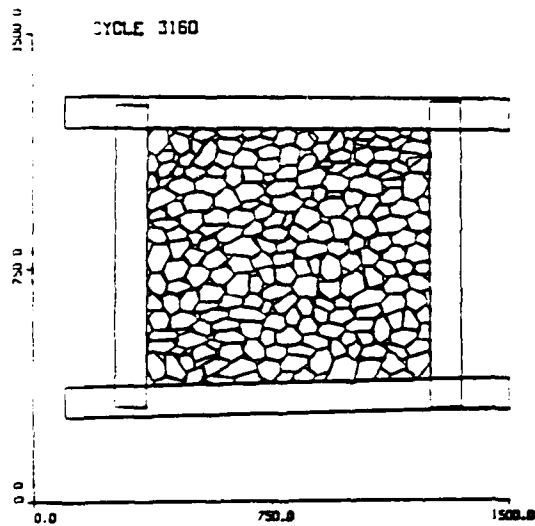
II.29 Triaxial test simulation, $90 \text{ bar} < \sigma_1 < 110 \text{ bar}$, $\sigma_2 = 50 \text{ bar}$



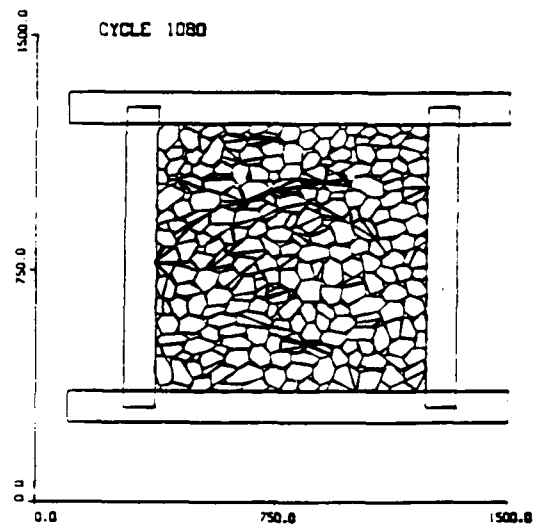
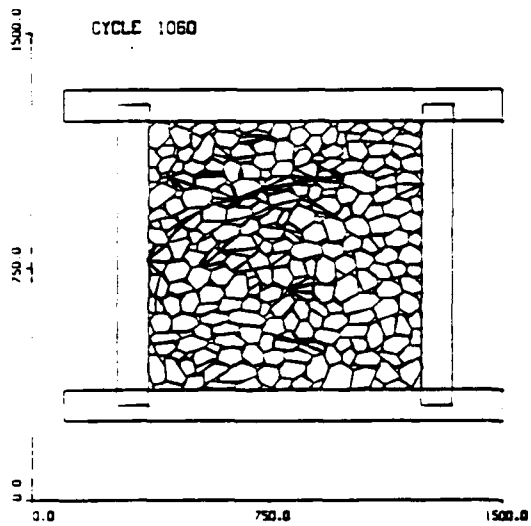
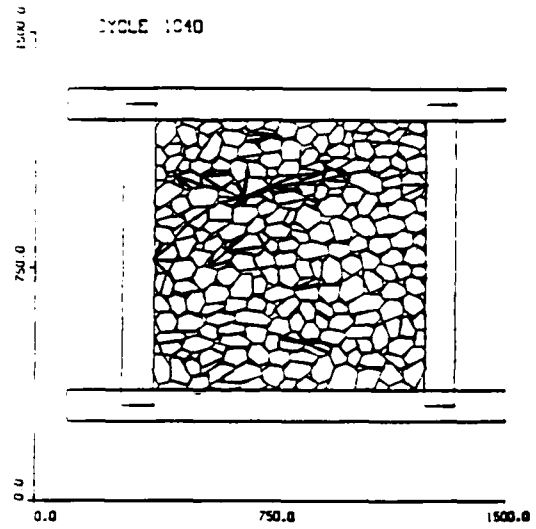
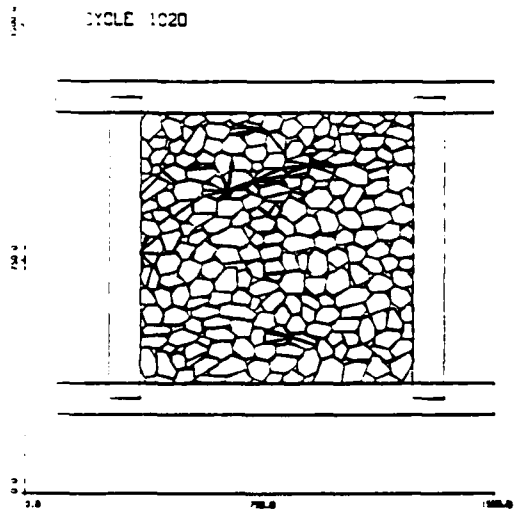
II.30 Triaxial test simulation, $110 \text{ bar} < \sigma_1 < 150 \text{ bar}$, $\sigma_2 = 50 \text{ bar}$



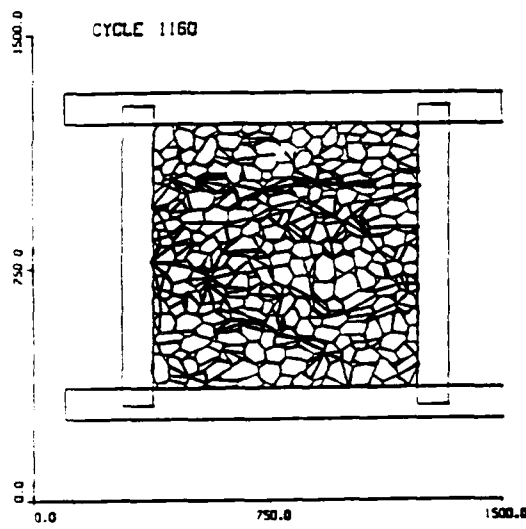
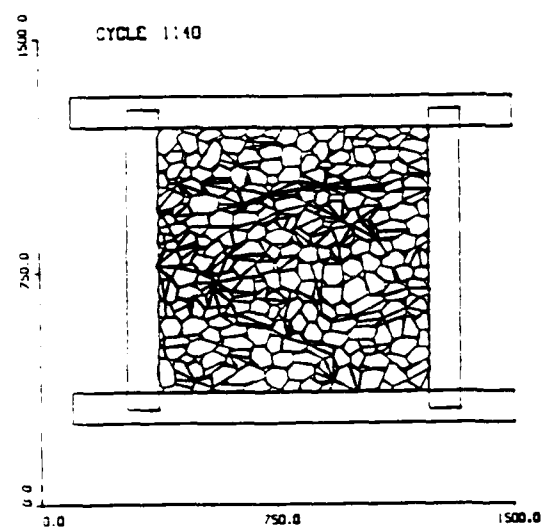
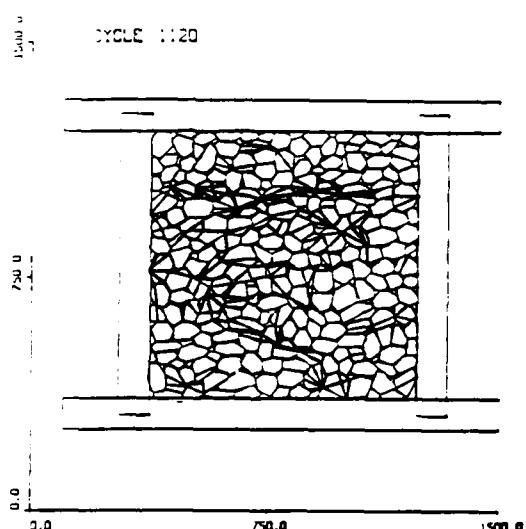
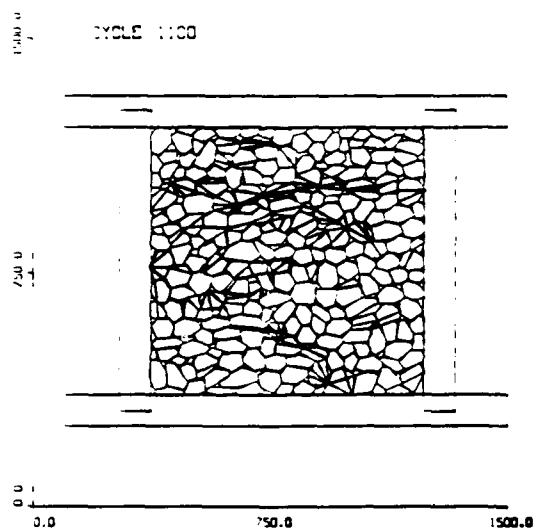
II.31 Triaxial test simulation, $130 \text{ bar} < \sigma_1 < 150 \text{ bar}$, $\sigma_2 = 50 \text{ bar}$



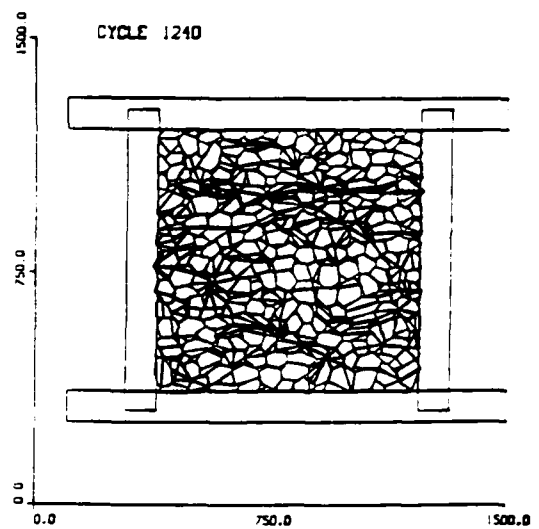
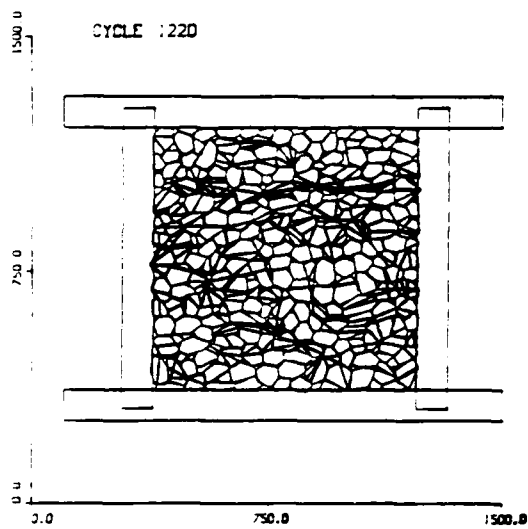
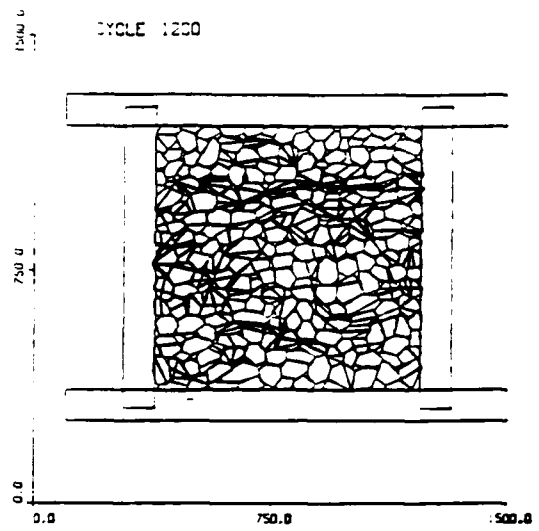
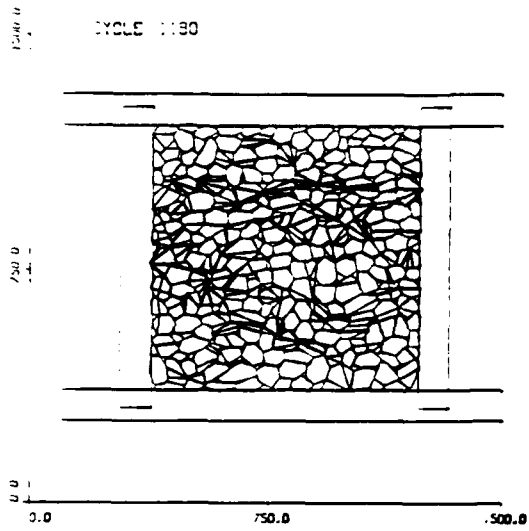
II.32 Triaxial test simulation, $120 \text{ bar} < \sigma_1 < 130 \text{ bar}$, $\sigma_2 = 50 \text{ bar}$



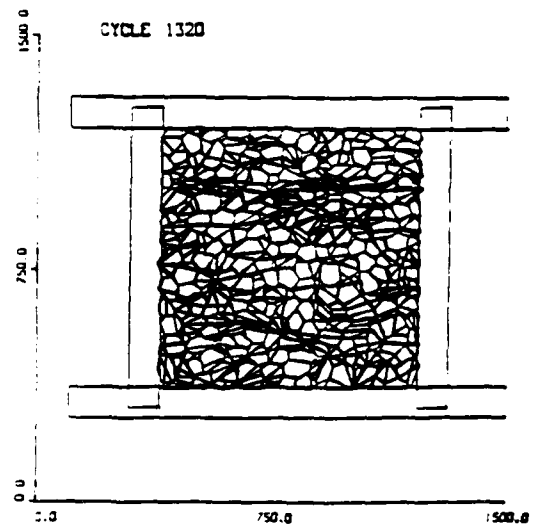
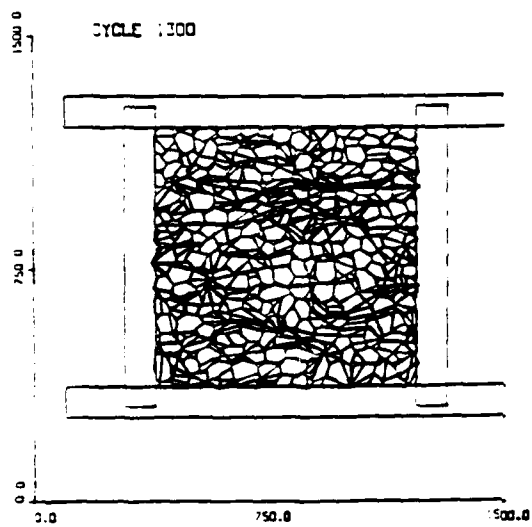
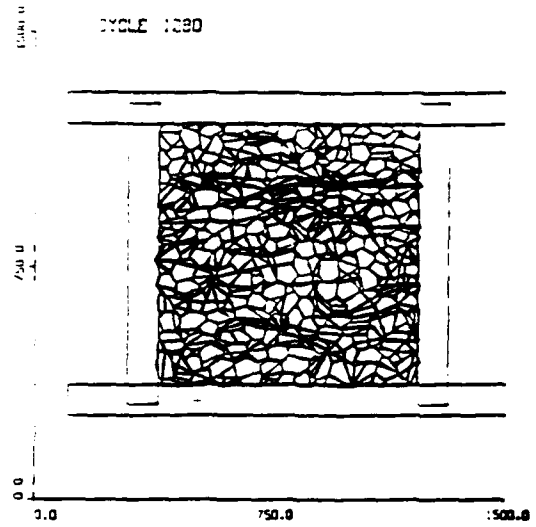
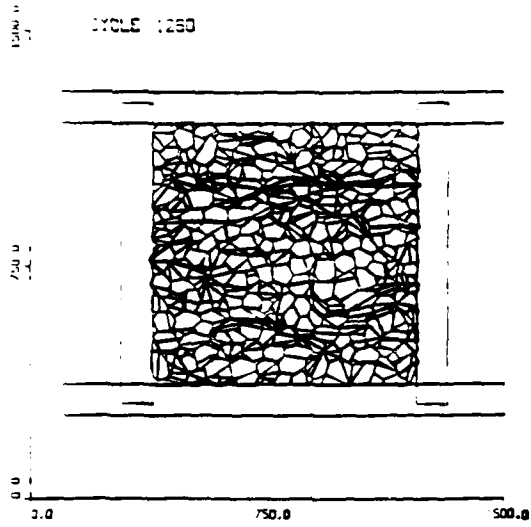
II.33 Triaxial test simulation. Contact force display
cycle 1020-1080



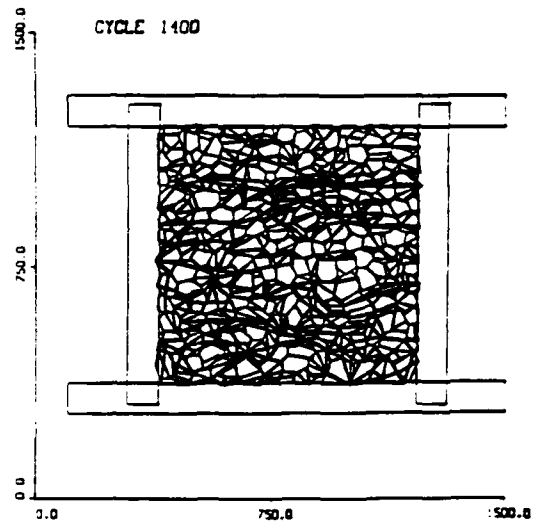
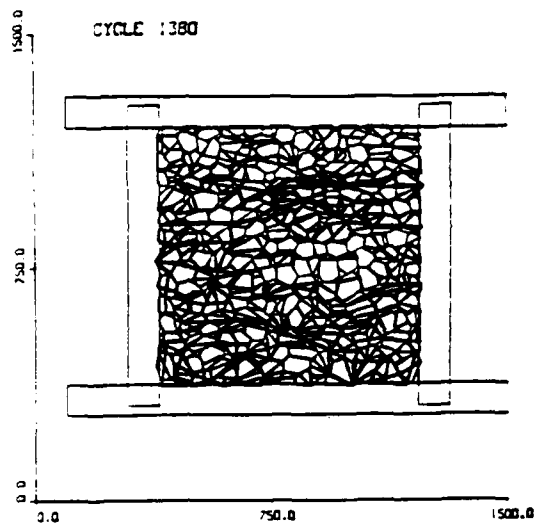
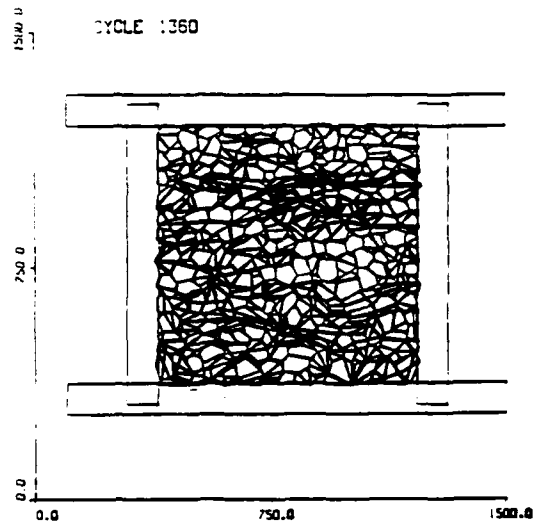
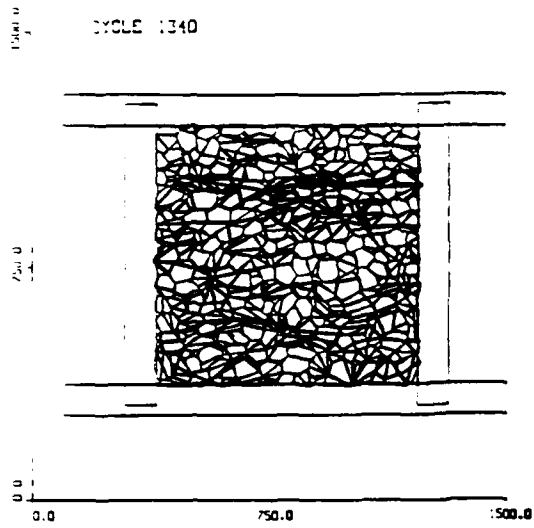
II.34 Triaxial test simulation. Contact force display cycle 1100-1160



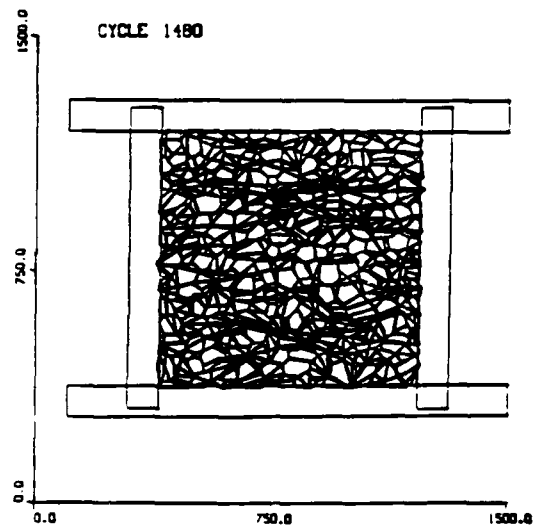
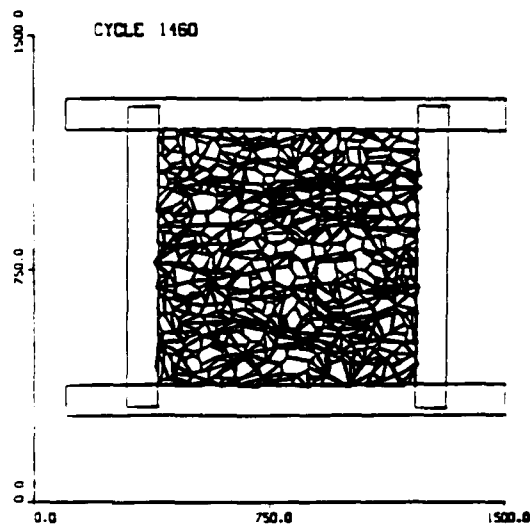
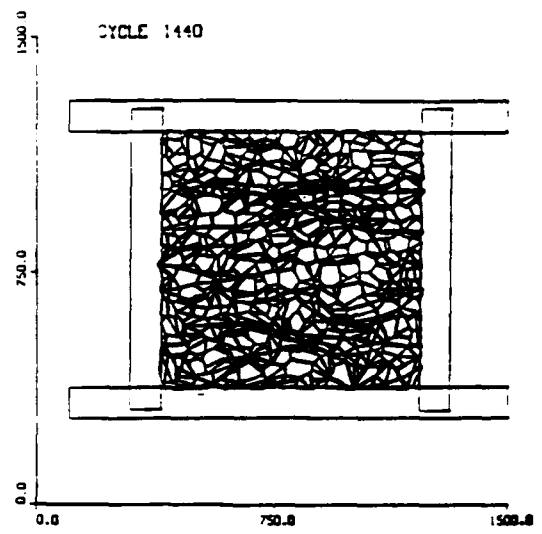
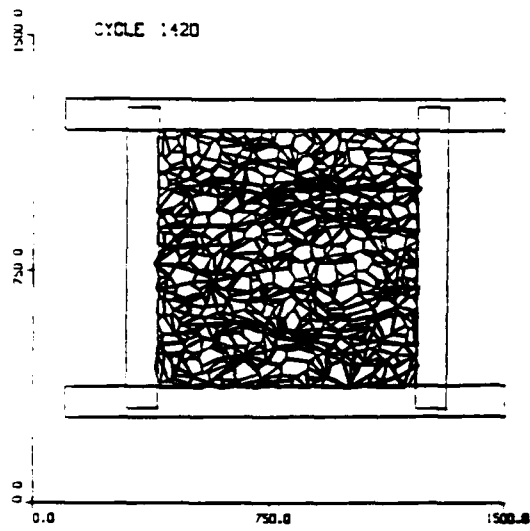
II.35 Triaxial test simulation. Contact force display
cycle 1180-1240



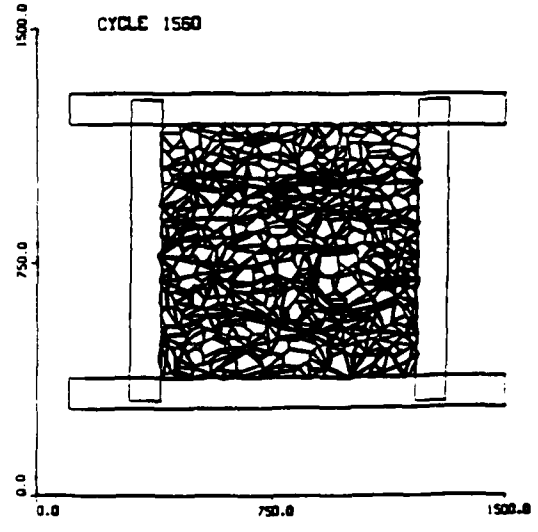
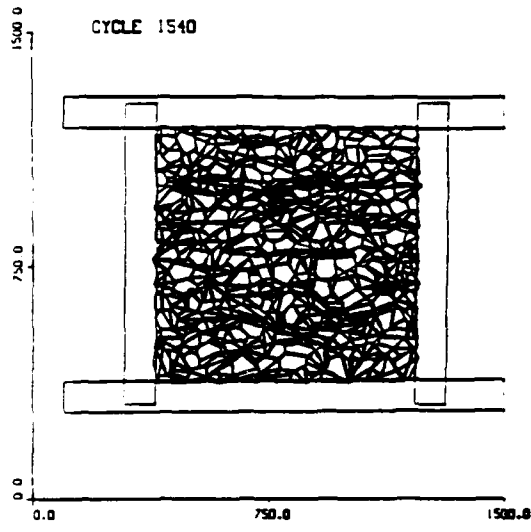
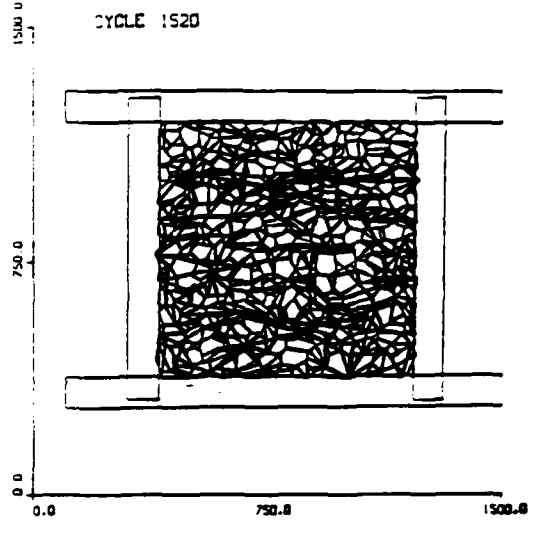
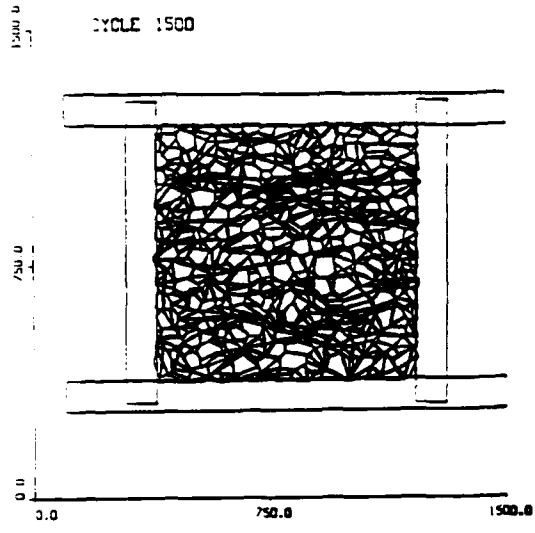
II.36 Triaxial test simulation. Contact force display
cycle 1260-1320



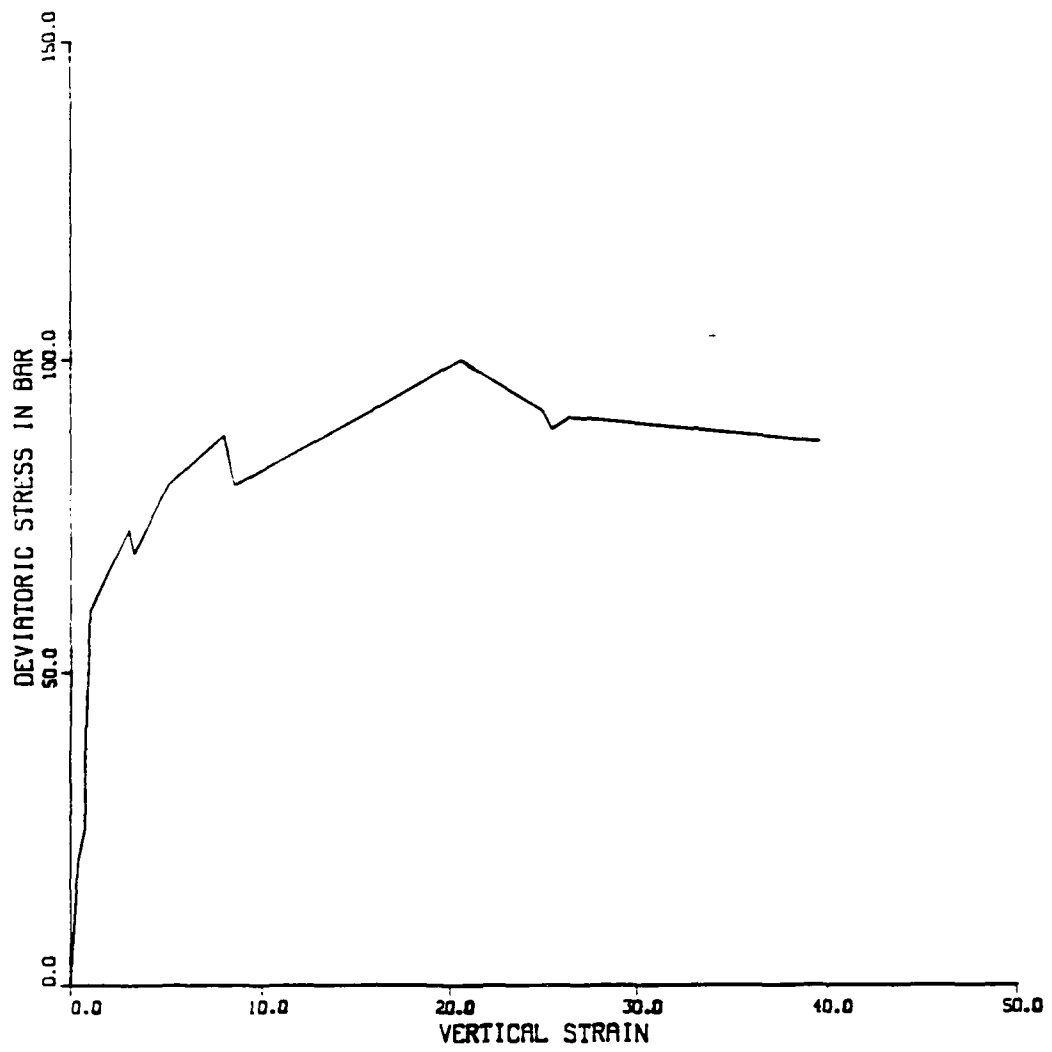
II.37 Triaxial test simulation. Contact force display
cycle 1340-1400



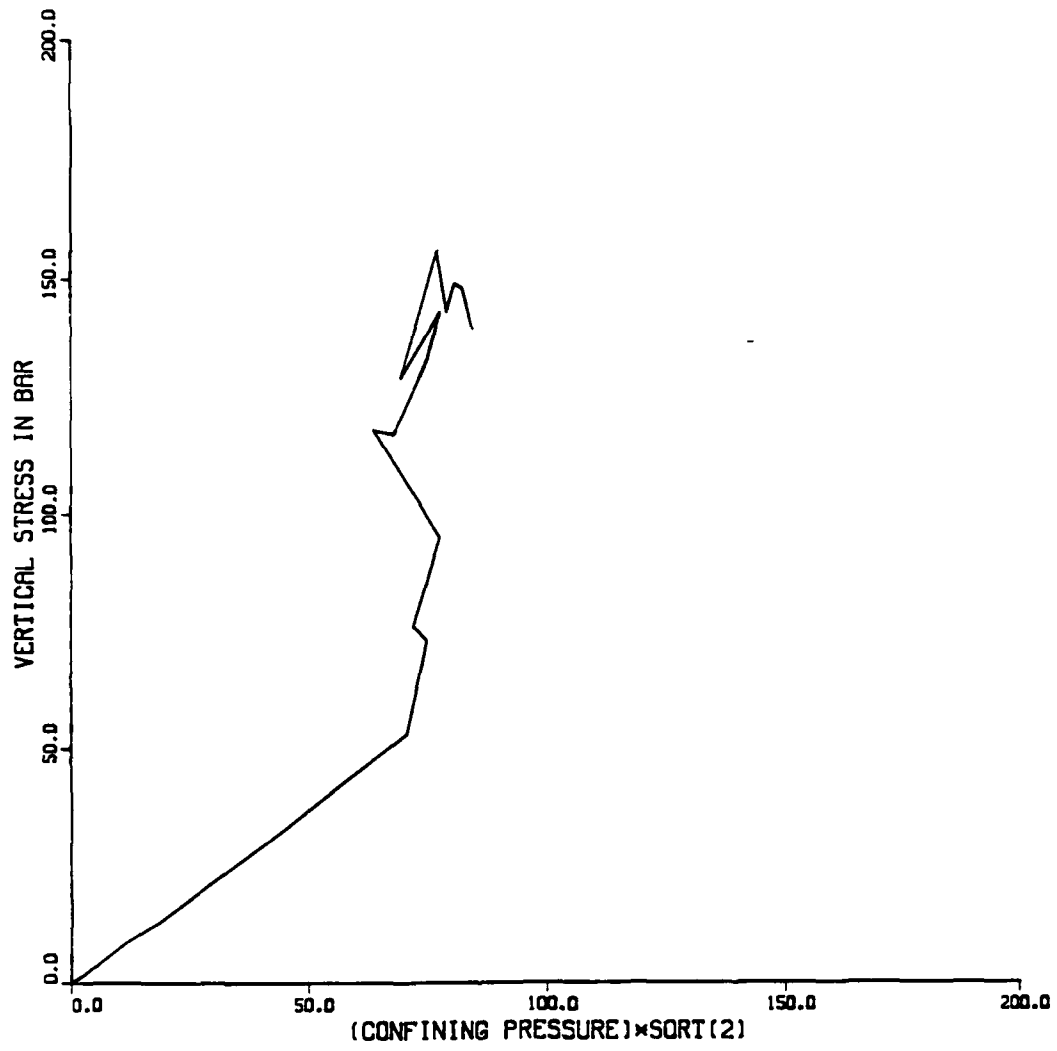
II.38 Triaxial test simulation. Contact force display
cycle 1420-1480



II.39 Triaxial test simulation. Contact force display
cycle 1500-1560



II.40 Triaxial test. Deviatoric stress versus vertical strain.



II.41 Triaxial test. Vertical stress versus confining pressure.

III. DEVELOPMENT OF THE EXPERIMENTAL EQUIPMENT

III.1 Introduction

The experimental equipment for triaxial testing at high pressures has been assembled and is suitable to performance of triaxial tests as originally envisioned. The equipment consists of a large frame with a hydraulic cylinder for vertical loading, and pressure supply units for lateral as well as vertical loading. An integral portion of the testing equipment consists of a dedicated computer which is used for datalogging and for control of the experiments. Any conceivable stress-path or strain-path possible in the triaxial apparatus can be followed under stress control or strain control. Figure 1 shows a schematic diagram of the experimental setup.

As described in previous progress reports, the first as well as the second design of a loading frame both turned out to be prohibitive in terms of cost. Alternative solutions were sought. Several used loading frames came on the market in the Spring of 1987, and one of these fulfilled the requirements for this project. This loading frame was first inspected (by Lade) in June at General Electric in Schenectady, N.Y., and subsequently purchased and transported to UCLA where it arrived in August of 1987.

The loading machine was fabricated by Gilmore (in Cleveland, Ohio) and purchased as one of three by General Electric in 1972. It has a capacity of 200 kips, and it is relatively stiff, an important requirement for controlled descent along the strain softening branch of any force-deflection curve. This loading frame, which came with a hydraulic cylinder for vertical loading, was substantially cheaper than any frame that could be designed and produced for this project. Further, the machine does not appear to have been used heavily, and all parts have been checked and are in good working condition.

While the loading frame was being acquired, the equipment to produce pressurized oil and cell fluid (water) was purchased. The pressure required in the hydraulic cylinder as well as the confining pressure in the triaxial cell are generated by step motors which act on ball screws through gears to compress oil and water in smaller hydraulic cylinders. In addition, a pressure booster pump to produce constant high pressure in water (from a low input air pressure) may be used for conventional triaxial tests performed at constant pressure. The actually achievable maximum cell pressure is 15,000 psi, as desired.

Both the vertical load and the triaxial cell pressure are controlled by the step motors to achieve any desirable stress path or strain path. This is accomplished using an integrated data acquisition system run by the same computer that controls the step motors.

The test data is collected from pressure transducers, LVDTs and load cells. In addition, quantities such as pressures and deformations will be monitored visually on pressure gages, and dial gages. All high pressure lines are provided with relief valves for safety.

A considerable amount of work including purchasing of computer hardware and software, as well as programming for test control, data logging and processing has been performed by two graduate students. The high levels of quality and sophistication in this high pressure testing equipment is well supported by the acquisition of the professionally built, but inexpensive loading machine.

The triaxial cell in which the specimens are tested has been constructed. This cell is designed for a maximum cell pressure of 15,000 psi (1000 bars). The maximum vertical load supplied by the loading machine (200,000 lbs) is more than sufficient to produce failure in a 3.0 inch diameter triaxial specimen under undrained conditions at the maximum cell pressure.

Each of the major components of the experimental equipment is described in further details in the following chapter. This includes the loading frame, the high pressure triaxial apparatus, the pressure sources, and the test control panel. The computerized datalogging and test control system is explained in a separate chapter below. Finally the results of a drained test and an undrained test produced by the newly developed equipment are presented to demonstrate its capabilities.

III.2 Details of Experimental Setup

III.2.1 Description of the Loading Frame

The loading frame is a "Gilmore model 426-200". It is designed to withstand 200 Kips static loads and 100 Kips dynamic loads. The frame consists of a base, four guide columns, and a crosshead.

The base is a 51"W × 35"D × 42"H welded steel fabrication. It serves as an anchor for the guide columns and a housing for the actuator. Four guide columns are anchored in the base. Each column is five inches in diameter and is of sufficient length to allow the test zone to be adjusted from zero to 77 inches. Maximum overall height of the columns, including base, is 161 inches. The crosshead is guided on the four columns. It is a 52"W × 33"D × 15"H welded steel fabrication. The crosshead is clamped to the columns by 14 clamp studs. It is lifted into position by two hydraulic cylinders mounted centrally on each side of the machine.

The actuator used in the loading frame is a "Gilmore model L433A-180" hydraulic actuator. It is of the double acting type with a double ended piston rod. The rating of the actuator is 200,000 lb static or 180,000 lb dynamic at an operating pressure of 3000 psi. The total stroke of the piston is 6 inches. The pressure in the actuator is measured by a "HBM" pressure transducer located outside the piston and by a "Heise" dial gage on the control panel.

Fixed on the crosshead is a 20 Ton "HBM model C3H2" load cell that is used to measure vertical loads. At higher loads, a 50 Ton "HBM model C3H2" and a 100 Ton "Interface model 1240-AF" load cells are used.

Two 500 lb "DUFFLYNX" electrical wire rope hoists were installed to lift the high pressure triaxial apparatus up on the pedestal on the loading machine. The hoists are mounted on the crosshead and slides on two 6 feet long I beams.

III.3 Description of the High Pressure Triaxial Apparatus (HPTA)

The HPTA when assembled stands 23 in. high, is 12 in. in diameter, and weights approximately 450 lb. It has four major components: the upper cap plate, the loading piston, the base plate, and the cylinder wall. All four pieces are fabricated from steel AISI 4340. They were heat treated to a yield strength of 180 Ksi with a Rockwell hardness of 40/43.

III.3.1 Upper Cap Plate and Loading Piston

The upper cap plate houses a linear bearing "Boston LBB-3000 extra-precision". The linear bearing guides a 17 in. long loading piston with 3 in. diameter.

The piston is dense chromed with a surface finish of 4 RMS to provide a sufficiently smooth surface against which to seal. A reciprocal seal made by "Ball Seal Engineering" is used to seal 15,000 psi of fluid pressure inside the triaxial cell. It is made from graphite fiber-reinforced PTFE and is activated by a medium-load spring. A backup ring made from high strength polymer is placed behind the seal to reduce extrusion during high pressure operation. The seal is held in place by an aluminum ring attached to the upper plate by 6 screws. It can be removed for replacement.

The upper cap plate has one groove that houses an O-ring which seals the fluid inside the cylinder wall.

The top cap incorporates a single drainage line used to vent any air trapped inside the cell prior to testing. The drainage line is closed by a high pressure valve located at its port outside the cap.

III.3.2 The Cylinder Wall

The cylinder wall has an inner diameter of 5 in. and a thickness of 1 in. The triaxial cell is designed for a pressure of 15,000 psi with a factor of safety of 2.5.

III.3.3 The Base Plate

The lower base plate incorporates a single chamber fluid line and two specimen drainage lines. The fluid line is used to pressurize the cell, and the fluid pressure is measured by an "HBM" pressure transducer installed at the outside port of the line. The two drainage lines are connected to the soil specimen top and bottom end plates. When opened, they conduct fluid from the specimen to the volume change device. A pressure transducer located on the drainage line outside the cell is used to measure the pore pressure in undrained tests.

The lower base plate has three grooves machined into it. The outer groove is used to house an O-ring which seals the fluid inside the chamber. The middle groove contains an O-ring that seals the lower end plate of the specimen to the base plate. The inner groove seals the lower cap drainage line to the base plate. The lower end plate of the soil specimen is 3 in. in diameter and detachable. Different sizes of end plates can be fixed on the base plate.

The apparatus is assembled with eight 1-1/2 in. diameter steel bolts. A specified torque, depending upon the cell pressure, is applied to tighten each bolt. Thick steel washers (0.2 in.) are used under each bolt.

III.3.4 Pressure Sources

Description of the components used to generate the high hydraulic pressures.

III.3.5 Pressure Source for Vertical Loading

The pressure source is generated by the linear motion of a piston in a hydraulic actuator. The piston is pushed by a 20 ton ball screw jack driven by a step motor. A reduction gear, manufactured by Sumitomo SM-Cyclo model H3090, has a 1:43 gear ratio. It is connected between the step motor and jack. The ball screw jack is manufactured by "Action Jack". The worm gear driven ball screw jack is highly efficient. It uses 1/3 the input torque of a machine screw jack. As a result less horsepower is required. The ball screw jack used has a 24 in. travel. This computer controlled system can generate pressures up to 3000 psi.

III.3.6 Cell Pressure Sources

Two pressures generating systems are used. One is computer controlled, the other is manual.

The first system is very similar to the one described above. The Sumitomo gear, model H3090, has a 1:17 ratio. It is coupled with a 10 ton ball screw action jack. The ball screw jack has a 10 in. travel distance and pushes an "Enerpack RD 910" hydraulic cylinder. A controllable cell pressure of 10,000 psi is generated using this system.

The second system uses an air operated booster pump. Manufactured by "SC Pumps model SC40-500-10", constant pressures up to 20,000 psi can be generated using 100 psi input air pressure. The pressure developed by the SC booster pump is delivered to a "Tescom series 54-2000" hydraulic pressure regulator with venting capabilities. The pressure regulator has a maximum working pressure of 15,000 psi. It is manually adjusted using the 160 MPa "Heise" Bourdon tube dial gauge.

III.3.7 Control Panel and Pressure Lines

All the valves are made by "Snotrik" and have a capacity of 45,000 psi. Two relief valves are used: one, made by "Snotrik" has a range from 0 to 6,000 psi, the other made by "HIP" has range from 0 to 20,000 psi. All high pressure fittings (0 to 20,000 psi) were manufactured by Snotrik, the low pressure fittings (0 to 3,000 psi) are made by Swagelok.

Two high precision pressure gauges are used to measure the hydraulic pressure. A "Heise model CM-12" with a range of 0 to 160 MPa measures the chamber pressure. It has an accuracy of 0.2 MPa. The other gauge "Heise model CMM-12" has a range of 0 to 40 MPa, and it is used to measure the vertical pressure with an accuracy of 0.025 MPa.

A high pressure flexible hose is used in pressurizing the cell. It has a working pressure of 25,000 psi. The pressure lines are made from stainless steel. They are 1/4 in. O.D. with a 0.065 in. thickness.

III.4 Computerized Datalogging and Test Control Systems

III.4.1 Typical Process Flow for Controlling a Test

A typical test, whether drained or undrained, or whether under strain control or stress control, has very similar process flow to control the test. Below is described in a simplified way the interfacing between instrumentation, signal conditioning, A/D conversion, processing raw data, the control algorithm, stepping motor control, and the hydraulic system.

A. Instrumentation

The instrumentation consists of the load cell, which measures the vertical load on the triaxial cell during any type of test, the LVDT, which measures the vertical deflection of the specimen during any type of test, the volume change device, which measures the amount of

water squeezed from the specimen under load during a drained test, the pressure transducers, which measure the cell pressure during any type of test, the vertical load hydraulic cylinder pressure during any type of test, and the specimen pore pressure under load during an undrained test. These are all electrical devices whose output voltage changes as either the load, displacement or pressure changes. The output from these devices are connected to the signal conditioning through shielded data cabling. All of the instrumentation is physically located on or near the triaxial cell on the loading frame.

B. Signal Conditioning

The signal conditioning performs several functions. It provides the excitation voltage to drive the instrumentation. The excitation voltage is 10 VDC for the load cells and pressure transducers, and it is about 5.1 VAC at about 6.3 kilohertz for the LVDT and volume change device. The signal conditioning also applies a gain to the output voltage from the instrumentation so it can more fully occupy the input voltage range of the A/D converter. This maximizes the resolution of the A/D converter. The output of the load cell and pressure transducers are a maximum of 20 mV, so a large gain must be applied to occupy the input voltage range, ± 10 VDC, of the A/D converter. The signal conditioning system also filters the incoming signal to reduce the random higher frequency noise level. The output of the signal conditioning system is connected with ribbon cables to the A/D converter in the microcomputer. The signal conditioning is physically located in a separate chassis near the microcomputer.

C. A/D Converter

The A/D converter converts the analog DC voltage signals to a digital format that can be used by the microcomputer. It scans the six different channels used by the instrumentation and is connected to them through the signal conditioning. A multiplexer changes the channels of the A/D converter and then measures the voltages. The data acquisition software that con-

trols the A/D converter, which is in the control program, then stores these values in variable numerical arrays in the microcomputer's RAM memory. These values are accessible by the control software to use for control of the test.

D. Processing Data and Control Algorithm

The software converts the raw data, which are voltages from the instrumentation, to real values by subtracting the reference voltage and multiplying by the calibration factor as determined from the instrument calibration.

Under strain control the theoretical strain or vertical displacement of the specimen is known throughout the test. This theoretical value is compared to the real value measured by the instrumentation. The control algorithm computes a new speed for the stepping motor that controls the vertical movement to keep as close to the theoretical value of displacement as possible. Under stress control the theoretical vertical stress and theoretical cell pressure are known throughout the test. These theoretical values are compared with the real values as measured by the instrumentation. The control algorithm computes new speeds for the stepping motors that control the vertical stress and the cell pressure to keep as close to the theoretical values as possible. The control algorithm computes the new stepping motor speeds. For a more detailed description of the software, see III.8 SOFTWARE DESCRIPTION.

E. Stepping Motor Control

The control algorithm computes new speeds for the stepping motors. To communicate this new speed, which is in a higher-level computer language, to the stepping motors, a series of steps must be involved. First, if the speed change of the stepping motor between the current speed and the prior speed is large enough or if there is a directional change, the motor may have to be ramped up or down (make the total speed change in discrete increments).

This is performed in the higher-level computer language. The actual hardware calls are performed here. Second, the hardware calls are performed through an assembly language interface, which ensures that the calls are compatible with the higher-level language calling conventions and the peripheral interface device. Third, the above hardware calls access an assembly language object file with subroutines that control the stepping motor driver card within the microcomputer. The stepping motor driver card sends out digital signals to the stepping motor driver pack that control stepping motor direction, speed and number of steps to move. The stepping motor driver pack interprets these signals and provides DC power to the stepping motors in the proper polarities and amounts. For a more detailed description of the software, see III.8 SOFTWARE DESCRIPTION.

F. Hydraulic System

Each stepping motor is connected to the hydraulic system through a reduction gear. The reduction gear drives a ball-screw jack, which also has some reduction effect. The action jack converts rotational motion into linear motion. The action jack pushes or pulls on a hydraulic cylinder, which injects or withdraws hydraulic fluid into the hydraulic system.

One stepping motor/hydraulic system injects or withdraws hydraulic fluid from the loading frame's vertical load cylinder. The vertical load cylinder is located in the base of the loading frame and actuates a piston that moves in the vertical direction. This hydraulic cylinder piston has a small platform on which the triaxial cell rests. The triaxial cell piston is pressed against the loading frame's stationary crosshead and moves relative to the hydraulic cylinder piston. Therefore, this stepping motor/hydraulic system controls the vertical movement or vertical load of the specimen in the triaxial cell.

The other stepping motor/hydraulic system injects or withdraws hydraulic fluid from the triaxial cell to directly increase or decrease the cell pressure on the specimen in the triax-

ial cell. The system instrumentation is connected to the triaxial cell, so the process flow would go back to A. INSTRUMENTATION and loop indefinitely until the end of the test.

The above description of the hydraulic system does not describe all of the piping, shutoff and isolation valving, and gages.

III.5 System Performance and Control Capabilities

The software limits the speed of the stepping motors to a maximum value of 2,500 steps per second in half-step mode. This is equivalent to 6.25 revolutions per second. The limit is intended to prevent motor stalling under maximum loads. This maximum speed translates into a maximum deformation rate of about 3 inches per hour. The maximum stress rate for the cell pressure stepping motor/hydraulic system is 7.46 MPa per minute, assuming that the motor speed is 2,500 steps per second and that the specimen has the same stiffness as the system. The maximum stress rate for the deviator stress/hydraulic system is 2.35 MPa per minute, assuming that the motor speed is 2,500 steps per second and that the specimen has the same stiffness as the system.

The random noise level varies depending on the instrumentation involved and the gain applied to the output voltage from the instrumentation. They are:

1. *Load Cell* - 0.008% error. The gain is the same for the 20 ton and the 50-ton load cells. Therefore, the 0.008% error represents 1.6 kilogram for the 20-ton load cell and 4.0 kilograms for the 50-ton load cell.
2. *Pressure Transducers* - 0.06% error. The gain will vary depending on the pressure range selected. The current range is at 8 MPa. Therefore, this error represents a value of 0.005 MPa or 0.7 pounds per square inch.

3. *Volume Change Device* - 0.003% error. The gain will not change on this device. Therefore, its error is equivalent to 0.003 cubic centimeters.
4. *LVDT* - 0.004% error. The gain will not change on this device. Therefore, its error is equivalent to 0.0001 inch.

The above values for random noise in the system do not reflect the true total error in the instrumentation, because each piece of instrumentation has its own accuracy. See III.7 EQUIPMENT DESCRIPTION for hardware instrumentation tolerances. In most cases the accuracy of the system will be the hardware accuracy, since the random noise level is much less than the hardware tolerance.

The control program's ability to control the hydraulic pressures and deformations in the system are based more on the random noise level than the overall accuracy of the system, since the random noise represents the repeatability of the data. The overall system accuracy is based more on the hardware tolerance, since it represents the deviations of measured data and reality. Therefore, the following values representing the ability for controlling parameters are based upon the random noise levels, rather than the hardware tolerance. The overall system accuracy is still the hardware tolerance. This is emphasized to allow the control software to be evaluated independently of the instrumentation hardware. This is important, because if the current instrumentation is replaced by higher-accuracy instrumentation, then the control software has the ability to improve the overall system accuracy to a level of the values shown below.

The control algorithm for strain control with constant cell pressure can control the strain rate to within 0.1% of the strain rate and control the cell pressure to a level of about 0.2% of the cell pressure when it is at full scale voltage, 10 VDC. The control algorithm for stress control can control the cell pressure and deviator stress to about the same level, but

there is an additional factor to consider: the triaxial cell piston seal friction. The triaxial cell piston seal friction appears to be a function of cell pressure. For the standard triaxial tests under constant cell pressure, the dynamic friction can be easily determined by the software, since its direction of motion is only in one direction and the test is performed at constant cell pressure. However, for a constantly varying cell pressure with changes of direction in vertical motion, it is more difficult. The model used in the control software can add an additional maximum error of approximately 0.4%, based on the maximum deviator stress for the type of soils currently used. This error occurs at vertical motion changes in direction. Points that are not located near vertical motion changes in direction appear to have a much lower additional error of about 0.1% to 0.2%. The selection of points in the stress path is crucial to keep this additional error to a minimum. If the user can keep the areas of the stress path he wishes to examine away from the vertical motion changes in direction, he can generally keep this additional error to a level of about 0.1%.

III.6 System Safety

Obviously, operating under such high pressures presents significant safety hazards to the operators in the event of equipment failure. Therefore system safety is designed with several levels of protection, both in hardware and software.

III.6.1 Hardware Safety Features

The hardware is comprised of the following:

1. *Limit Switches* - Both hydraulic cylinders driven by the stepping motors have limit switches installed to limit the maximum length of travel. The limit switches switch off the power to the stepping motor driver pack, which stops the stepping motors.
2. *Pressure Relief Valves* - Both high pressure stepping motor/hydraulic systems have

pressure relief valves installed to limit the maximum pressure in each system. They are preset to 16,500 pounds per square inch for the cell pressure system and 3,600 pounds per square inch for the vertical load system. There is also a pressure relief valve on the volume change device/backpressure system preset to 100 pounds per square inch.

3. *Physical Shield* - There is a one-inch thick steel plate measuring 18 inches by 47 inches mounted on the loading frame to help protect the operator, if the triaxial cell fails.
4. *Monitoring Devices* - There are direct manual monitoring devices to allow the operator to monitor system parameters during the test. They consist of precision pressure gages and dial gages. If the parameters reach levels beyond the system ratings, the operator can manually stop the test.
5. *Emergency Stop Switch* - There is an emergency stop switch that directly issues an uninterruptible stop order to the stepping motor driver card, which controls the stepping motors. The physical location of the emergency stop switch is on the signal conditioning chassis located next to the microcomputer.

III.6.2 Software Safety Features

1. *Control Program* - The control program monitors the system instrumentation and has software routines checking the vertical load, the cell pressure, and the loading frame vertical load hydraulic cylinder pressure to ensure that they remain within the system ratings. If not, the software will issue a visual and audible warning and terminate the test.

The test software constantly monitors the test progress and displays four plots on the screen in real time to aid the operator in monitoring the test progress. During the test, the operator can stop the test at any time by pressing a special function key on the microcomputer keyboard.

III.7 Equipment Description

A. Instrumentation

1. *Pressure Transducers* - HBM, Model P 3MA, 1000 bar and 500 bar capacities, 2 mV/V sensitivity, 0.15% tolerance.
2. *Load Cells* - HBM, Model C3H2, 20 metric ton and 50 metric ton capacities, 2 mV/V sensitivity, 0.1% tolerance.
3. *LVDT* - Schaevitz Engineering, Model 2000 E, linearity 0.56%, 2 inch.
4. *Volume Change Measuring Device* - Custom made device using a double-acting piston, which alternately pushes or expels water from one of two chambers through a four-way valve. An LVDT is attached to the piston to measure movement.
5. *Cabling* - Shielded, 4 - wire, stranded type.

B. Signal Conditioning

1. *System* - Analog Devices, 3B Series Signal Conditioning Subsystem, AC/DC power supply, terminal connections for 8 separate channels of inputs.
2. *Signal Conditioning Modules* - Analog Devices, Model 3B16 for strain gage input, adjustable gain, adjustable zero, 10 VDC excitation voltage, module modified to allow calibration grade potentiometer to vary gain. Model 3B17 for LVDT input, adjustable

zero, adjustable span, adjustable gain, adjustable AC excitation voltage, adjustable excitation frequency.

3. *Signal Conditioner/AD Converter Interface Board* - Prototype board to interface the signal conditioning system, which is a single-ended input type to the AD converter, which is a differential-input type.

C. A/D Converter

Data Translation, Model DT2801/5716, 16 bit resolution, 2.5 kilohertz maximum conversion speed, 8 input channel capacity, differential input, +-10 VDC maximum voltage input.

D. Microcomputer

IBM, Model AT, 512 kilobytes of RAM, 6 megahertz clock speed, 1.2 megabyte flexible disk drive, 20 megabyte fixed disk drive.

E. Stepping Motor Driver Card

Rogers Labs, Model I 432 I/O, 4-axis motion stepping motor capability.

F. Stepping Motor Interface Board

Termination board between stepping motor driver card and stepping motor driver pack.

G. External Relay Board

Relay board which allows external devices such as switches to provide direct input to the stepping motor driver card. Three DC relays and AC/DC power supply.

H. Stepping Motors

Superior Electric, Model M111-FD12, 4 phase, 2.26 VDC, 6.1 amps per phase.
Anaheim Automation, Model 42D112-12AR, 4 phase, 3.6 VDC, 6.1 amps per phase.

I. Stepping Motor Driver Pack

Anaheim Automation, Model DPB05, 4 phase, 6.5 amps per phase capacity, bilevel type, two motor output.

J. Power Conditioner

Topaz, Model Peak 2, 02406-01P3, 120 VAC, 1000 VA capacity.

K. Surge Protector

Inmac, Model 8207, 4 outlet, 120 VAC, 15 amp rating, zener diode, MOV, gas-tube protection levels.

III.8 Software Description

There are several programs that were written for different purposes. All the higher-level language programs were written using Microsoft QuickbasicR Version 3.0. All low level language programs were written in Assembly Language and assembled using the MicrosoftR Macro Assembler Version 5.0.

The programs fall into two general groups, utility programs and testing programs.

A. Utility Programs

1. *MENU.EXE* - This program provides a user interface for inputting all of the data relevant to run the desired test. It is fully menu driven and prompts the user for infor-

mation and also has error checking routines. The test data is written into an ASCII file for access by the test programs. The program length is approximately 1,300 lines.

2. *DATAOUT.EXE* - This program provides the user with the amplified instrumentation voltages on the different data channels, whenever it is triggered. The voltages are written to an ASCII file. This is used when calibrating the instrumentation. The program length is approximately 200 lines.
3. *STEPPER.EXE* - This program allows the user to independently operate the two stepping motors in either direction and at any speed. The program length is approximately 200 lines.
4. *QT5DATA.EXE* - This program provides the user with the amplified instrumentation voltages on the different data channels, whenever it is triggered and is similar to *DATAOUT.EXE*, except it is utilized with the stepping motor operating. This allows the user to calibrate in a continuous running mode, so hysteretic behavior of instrumentation can be checked. Voltages are written to an ASCII file. The program length is approximately 400 lines.
5. *FRICT.EXE* - This program allows the user to measure the triaxial cell piston seal static and dynamic friction forces. Its method of operation is to increase the triaxial cell pressure to a series of desired values and then run the piston both up and down, while keeping the cell pressure constant. The friction force is the difference between the converted values of the load cell and the cell pressure multiplied by the piston area. Therefore, this program measures both the static friction (when the piston first starts to move) and dynamic friction(after the piston has moved several thousandths of an inch) force. All values are written to an ASCII file. The program length is approximately 700 lines.

6. *FRICT1.EXE* - This program allows the user to measure the piston seal dynamic friction force. This program is different from *FRICT.EXE*, because it does not stop at a series of cell pressures. It continuously increases the cell pressures up and down to desired values and takes continuous readings of the friction force. Since the cell pressure is increasing continuously, the value that is measured is the dynamic friction force. All values are written to an ASCII file. The program length is approximately 500 lines.
7. *FRICT2.EXE* - This program is similar to *FRICT1.EXE* except it has incorporated within it the subroutine that predicts triaxial cell seal friction, so the real friction can be compared to the estimated friction from the friction model used in the test programs. The program length is approximately 600 lines.

B. Test Programs

1. *TEST.EXE* - This program is the access program for all the different test programs. The user executes this program and it checks the data file created by the menu program and automatically executes the correct test program. The program length is approximately 20 lines.
2. *CU_CD_S3.EXE* - This program controls two different types of tests. They are the drained and undrained triaxial compression tests with constant cell pressure performed under constant strain rate. Isotropic and anisotropic consolidation are also included. See below for more detailed description of program elements. The program length is approximately 2,400 lines.
3. *CU_CD_S1.EXE* - This program controls two different types of tests. They are the drained and undrained triaxial compression tests with constant vertical stress performed under constant strain rate. Isotropic and anisotropic consolidation are included. See

below for more detailed description of program elements. The program length is approximately 1,800 lines.

4. *GENSTRSS.EXE* - This program controls a general stress path type of test performed under stress control. See below for more detailed description of program elements. The program length is approximately 1,900 lines.
5. *GENSTRN.EXE* - This program controls a general strain path type of test performed under strain control. See below for more detailed description of program elements. The program length is approximately 2,100 lines.

C. Test Program Elements

The different test programs are composed of several different elements. The major elements are data acquisition, data reduction, storing data, control, actuation of stepping motors, and graphic display of test data.

1. *DATA ACQUISITION ELEMENT* - The data acquisition element is written in the basic computer language, since the A/D converter is designed to accept commands using the "memory mapped I/O" concept, which uses different RAM memory addresses as Command, Data and Error registers. The basic computer language is adept at this function. Commands are sent to the Command register's memory address in specified bit patterns. Data is read from the Data register address in two-byte increments and converted from binary to decimal. Error messages are read from the Error register address and their meaning is translated by their bit patterns. This program element samples data at a rate of approximately 2 kilohertz. Six channels are monitored, which correspond to the vertical load cell, the specimen pore pressure, the triaxial cell pressure, the loading frame's vertical load hydraulic cylinder pressure, the volume change, and the vertical motion LVDT. The data received from the A/D converter is a DC

signal voltage from the different pieces of instrumentation. Fifty samples on each channel are taken and then averaged to act as a low-pass data filter, which tends to reduce the random noise level.

2. *STORING DATA* - The above data is stored onto the fixed disk in an ASCII file called *VOLTAGE.PRN*. The individual channel voltages are then converted into their real instrumentation values by subtracting the reference voltage and multiplying by the calibration factor for that piece of instrumentation. These "real" values are then stored onto fixed disk in an ASCII file called *DATA.PRN*. When the actual shearing portion of the test starts, these values from the instrumentation are converted to actual engineering parameters for axial strain, volumetric strain, deviator stress, stress ratios, and P and Q, which are stress path parameters. Control is accomplished using these values. These engineering parameters are then stored onto fixed disk in an ASCII file called *FINAL.PRN*. Since the three above listed data files are ASCII files, they can be imported directly into LOTUS 1-2-3R for post-test plotting of results or further data analysis.

If the measured value from the instrumentation exceeds specified values for maximum load or pressure, the program stops execution and automatically starts unloading the specimen.

3. *CONTROL* - There are two general types of control elements. One for strain control and one for stress control.

Under strain control, at any time during the shearing portion of the test there should be a specific vertical displacement of the specimen. This can be calculated from the elapsed time of the test and the strain rate. This theoretical value is compared with the real value given from the LVDT and if it is less or greater than this

value, a new speed for the vertical direction stepping motor is computed. The control algorithm uses the method of proportional response. In other words it adjusts the change in stepping motor speed relative to the amount of continuing divergence from the theoretical displacement value. It also buffers this proportional response so that if the difference between the theoretical and real values of displacement is closing at an acceptable rate it does not change the stepping motor speed. The effect of this is to eliminate overshooting the theoretical value and help keep the control algorithm stable.

Some of the tests require constant cell pressure. Since the piston is descending into the triaxial cell, fluid needs to be removed from the triaxial cell to keep a constant cell pressure. The other stepping motor bleeds off this excess fluid, however, it is controlled by using the measured value of cell pressure, comparing it to the desired cell pressure. This control algorithm is very similar to the above one for strain control.

Under stress control, at any time during the test there should be a specific vertical stress and a specific cell pressure on the specimen. This can be calculated from the elapsed time of the test and the vertical and horizontal stress rate. These theoretical values are compared with the real values given from the cell pressure transducer and a calculated value involving the load cell, cell pressure, seal friction, and membrane stiffness. If the real values are less or greater than these theoretical values, new speeds for the vertical direction stepping motor and the cell pressure stepping motor are computed. The control algorithm also uses the method of proportional response. In other words it adjusts the change in stepping motor speed relative to the amount of continuing divergence from the theoretical vertical stress and cell pressure values. It also buffers this proportional response so that if the difference between the theoretical and real values of vertical stress and cell pressure are closing at an acceptable rate, it does not change the stepping motor speed. The effect of this is to eliminate

overshooting the theoretical values and helps keep the control algorithm stable.

4. *ACTUATION OF STEPPING MOTORS* - This program element operates the stepping motors. It is composed of three parts. They are the higher-level language part, the assembly language interface, and the vendor-supplied proprietary object file.

The vendor-supplied proprietary object file is a series of assembled assembly language subroutines, which can be called from higher-level languages through an interface. Some of the different subroutines are *FREQ1N2* and *FREQ3N4*, which set the desired speed of up to four stepping motors, *MOT1*, *MOT2*, *MOT3*, and *MOT4*, which set the direction of rotation of the stepping motors and the number of steps to travel in that direction. There are some limits to the control of the stepping motors. Of particular importance is the limitation that the stepping motor speed must be above 40 steps per second and that a motor can only be commanded to move between 1 and 32767 steps in one subroutine call. The significance of the 40 steps per second limitation is that if the constant stepping motor speed is directed to fall below 40 steps per second by the control algorithm, then the only way to approximate this low speed is to operate the motor in an intermittent (on/off) mode instead of at a continuous speed. The significance of the 1 to 32767 steps limitation is that when it is desired to run the motor continuously, the motor must be called repeatedly before the number of steps from the last subroutine call runs out and stalls the stepping motor.

The assembly language interface, called *QB1*, was written to provide a bridge between the higher-level language and the vendor-supplied assembly language subroutines. This is necessary to accommodate the calling conventions of the particular higher-level language, which is Microsoft QuickbasicR Version 3.0.

The higher-level language portion consists of two elements. They are a subroutine called STEPMOT and a subprogram called STEPPER. They perform several necessary functions that cannot be performed directly by the vendor-supplied assembly language subroutines. STEPMOT maintains a record of the last and current stepping motor directions and speeds, which is used by STEPPER to ramp up or ramp down (make the total speed change in smaller discrete steps) the stepping motor speeds to the desired level. Ramping is required because stepping motors cannot change speeds in large increments without stalling. STEPPER makes the actual calls to the vendor-supplied assembly language object file.

5. *GRAPHIC DISPLAY* - This portion is composed of two separate elements. They are the background screen generation element and the line plotting element. Together they display in real-time the engineering parameters calculated earlier. Both elements were written for an Enhanced Graphics Adapter type of display. The background element splits the screen into four separate graphics windows. Each window is for an X-Y graph plot of deviator stress versus axial strain, effective stress ratio versus axial strain, stress path (Cambridge P versus Cambridge Q), and either volumetric strain versus axial strain or pore pressure versus axial strain depending on whether the test is drained or undrained. The vertical scale is auto-scaling as a function of the confining pressure. Window borders, axes, grid lines and labels are plotted on the screen. The background element is generated only once, so when the test is running only lines between data points will need to be plotted on the existing background.

The line plotting element plots lines between the last data point and the current data point. Also, the current numerical values of the calculated engineering parameters are printed on the screen within the window boundaries.

III.9 Results of Two Experiments

Triaxial equipment already available in the Soil Mechanics Laboratory has been used to perform a series of baseline tests in triaxial compression and extension. Drained tests were performed with constant cell pressures up to 600 psi in compression and extension. The granular material used for these tests and the tests in the high pressure triaxial apparatus is Cambria Sand of similar composition to that used in two previous research projects. This is the same sand that is being modeled in the numerical investigation being conducted using the PROBS computer program.

The results of two tests performed in the high pressure triaxial apparatus are shown in the diagrams on the following pages. One test is a consolidated - drained test (CD Test), and the other is a consolidated - undrained test (CU Test). The specimens were isotropically consolidated to 1200 psi (8.277 MPa) in both tests before shearing was initiated.

The results of the drained test are shown in Figs. 2,3,4 and 5. Figure 2 indicates the effective stress-path on a Cambridge p - q diagram. For a drained test at constant confining pressure the stress-path is a straight line at a slope of 1 horizontal on 3 vertical. The deviator stress - axial strain curve is shown in Figure 3 and the max. deviator stress is indicated at 19.79 MPa corresponding to an effective friction angle of 33.0° . The variation of the effective stress ratio is shown in Figure 4, and the volume change curve is shown in Figure 5. At this confining pressure, the initially dense soil specimen is highly compressive, and this compression is directly related to the crushing of the soil grains.

The results of the undrained test are shown in Figures 6,7,8 and 9. The effective stress-path in Figure 6 is controlled by the variation in pore pressure as the deviator stress is increased. The deviator stress-axial strain variation shown in Figure 7 and Figure 8 indicates the variation of the effective stress ratio. The maximum effective stress ratio of 3.26 is

reached at about 18% axial strain. This corresponds to a friction angle of 32.0° . The pore pressure variation is shown in Figure 9.

The diagrams of test results shown in Figures 2-9 indicate the capability of the experimental equipment to perform tests of the types required for this investigation.

III.10 Microphysical Characteristics of Granular Materials

Part of the experimental study focuses on an investigation of the microphysical properties of granular materials and their changes during shear tests. This will have important bearing on the development of realistic computer models of granular materials, and provide another basis for comparing experiments and numerical studies. In essence this work involves counting the number of contact points and their orientation at various points of a shear test. In particular, the evolution of microphysical geometry of the granular materials is being studied by examining triaxial specimens at several stages of a test, including before, during and after failure of the specimen. Parameters such as shape, size distribution, breakage, and orientation of particles as well as the number and orientation of particle contacts are being measured. By "freezing" the specimens at different stages, these parameters may be measured and their evolution can be followed during the tests.

It was originally planned that this part of the project would be performed on the same Cambria Sand as used in the other parts of the project. However, it quickly became clear that the particles were too small (in the range from 1.0 to 2.0 mm) for observation of contact points and their directions. This portion of the study is therefore being performed on another size range of Cambria Sand. The grain sizes in this material range from 2.0 mm to 5.0 mm. The grain shapes, distribution, etc. in this range have already been studied and adjusted (where possible) to match the original Cambria Sand.

The experimental equipment for the study of grain contact angles and their evolution has been constructed and refined for use on a routine basis. Several specimens have been studied. Approximately 200 grains (40 grains in each of five layers) located near the middle in each of 5-7 specimens are sheared in triaxial compression to different amounts of vertical deformation, "frozen" (using a paint technique), and taken apart, grain by grain, noting position, orientation, grain contact numbers and directions. By combining the results from the 5-7 specimens it is possible to follow the evolution of these microphysical characteristics.

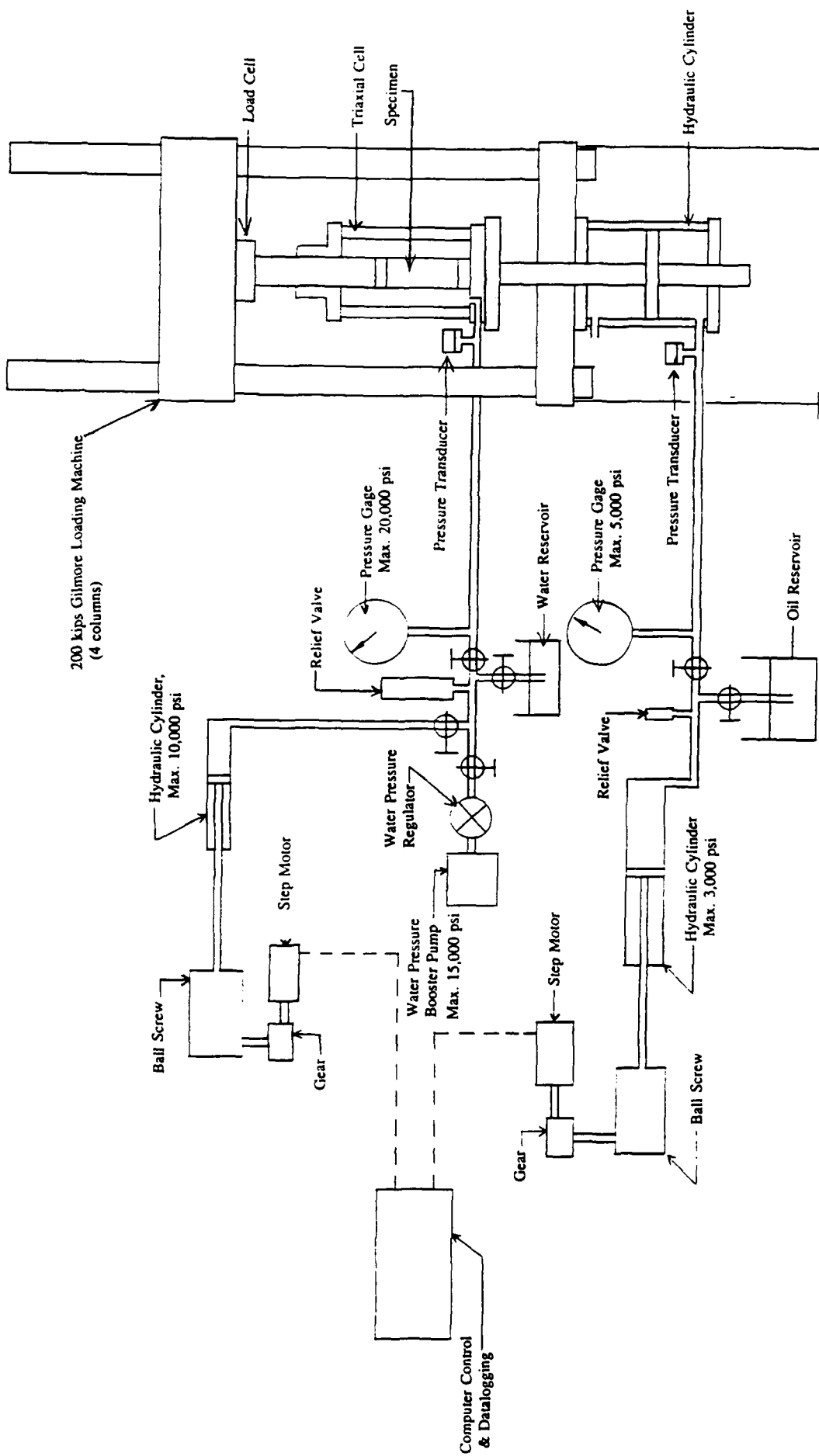
This study is being performed on specimens sheared at a low confining pressure of 1.0 kg/cm². Thus, particle breakage is unlikely to occur in these tests. Particle breakage, consequent variation in size distribution and possibly the variation in shape (due to breakage) will be studied in tests at very high confining pressures as explained above.

III.11 Summary and Conclusions

It took approximately the first year of the two year contract to obtain a loading machine for the high pressure triaxial testing to be performed on this project. The reasons for this time delay have been explained in the progress reports and in the present report. However, at this time, i.e. at the end of the two-year period, the experiment facility for high pressure triaxial testing has been constructed and it is in excellent working condition. The capabilities of the equipment meets or exceeds the originally intended levels of performance, and it has been constructed within the original budget. The major cost has been the extra time spent in reaching the point where the loading frame was in house at UCLA.

High pressure triaxial testing is progressing according to a regular schedule set up to provide data to be analyzed in relation to stability/instability of granular soils at high pressures. It is anticipated that the results of these tests and their analyses will be presented in addendums to the present final report. Along with these results will also be more detailed

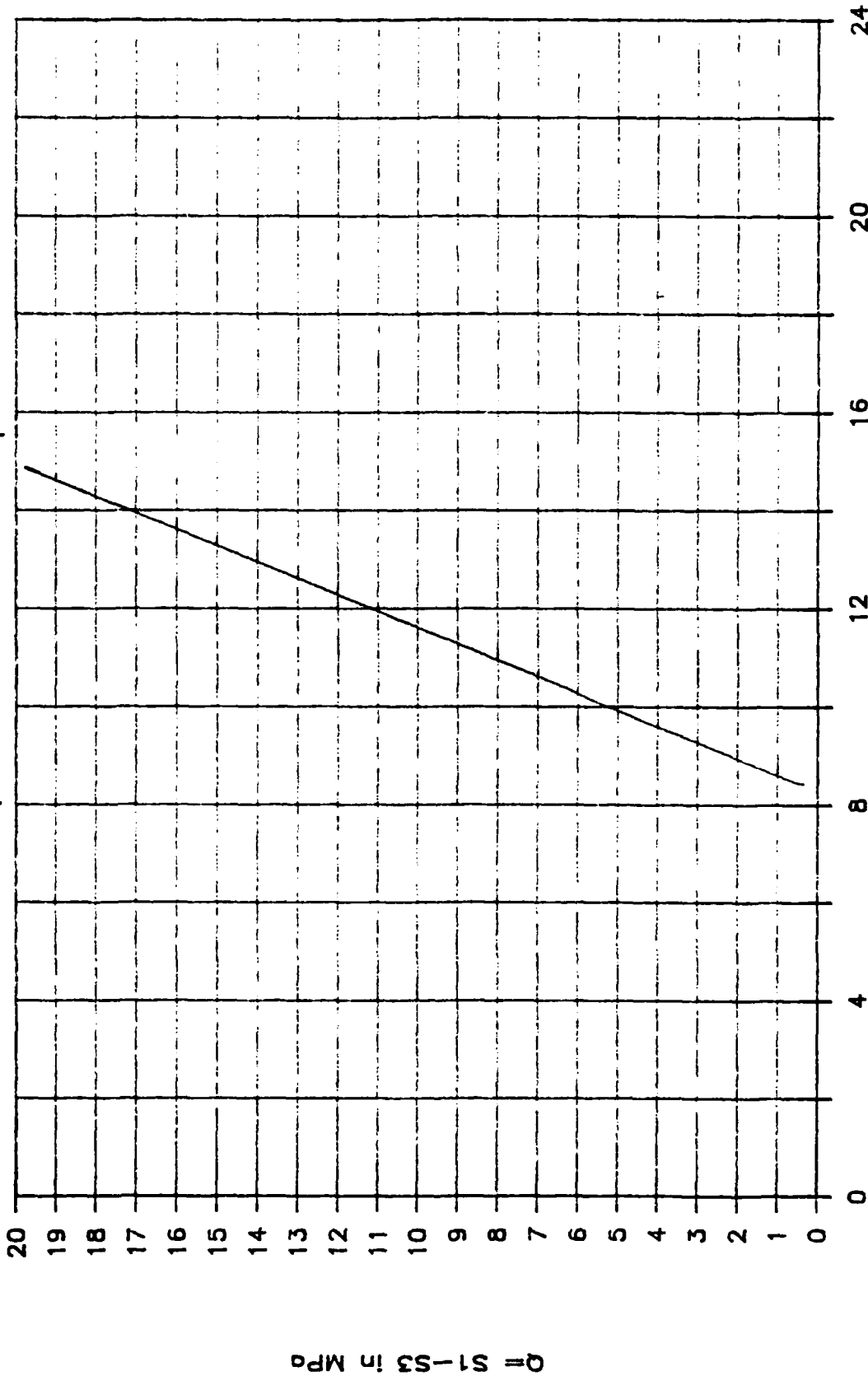
presentations of the experimental equipment as well as the study of micromechanical characteristics of granular materials initially proposed to AFOSR.



III.1. Schematic Diagram of Experimental Setup for High Pressure Triaxial Testing.

Triaxial Compression of Cambria Sand

CD Test; Eff. Conf. Pressure = 1200 psi

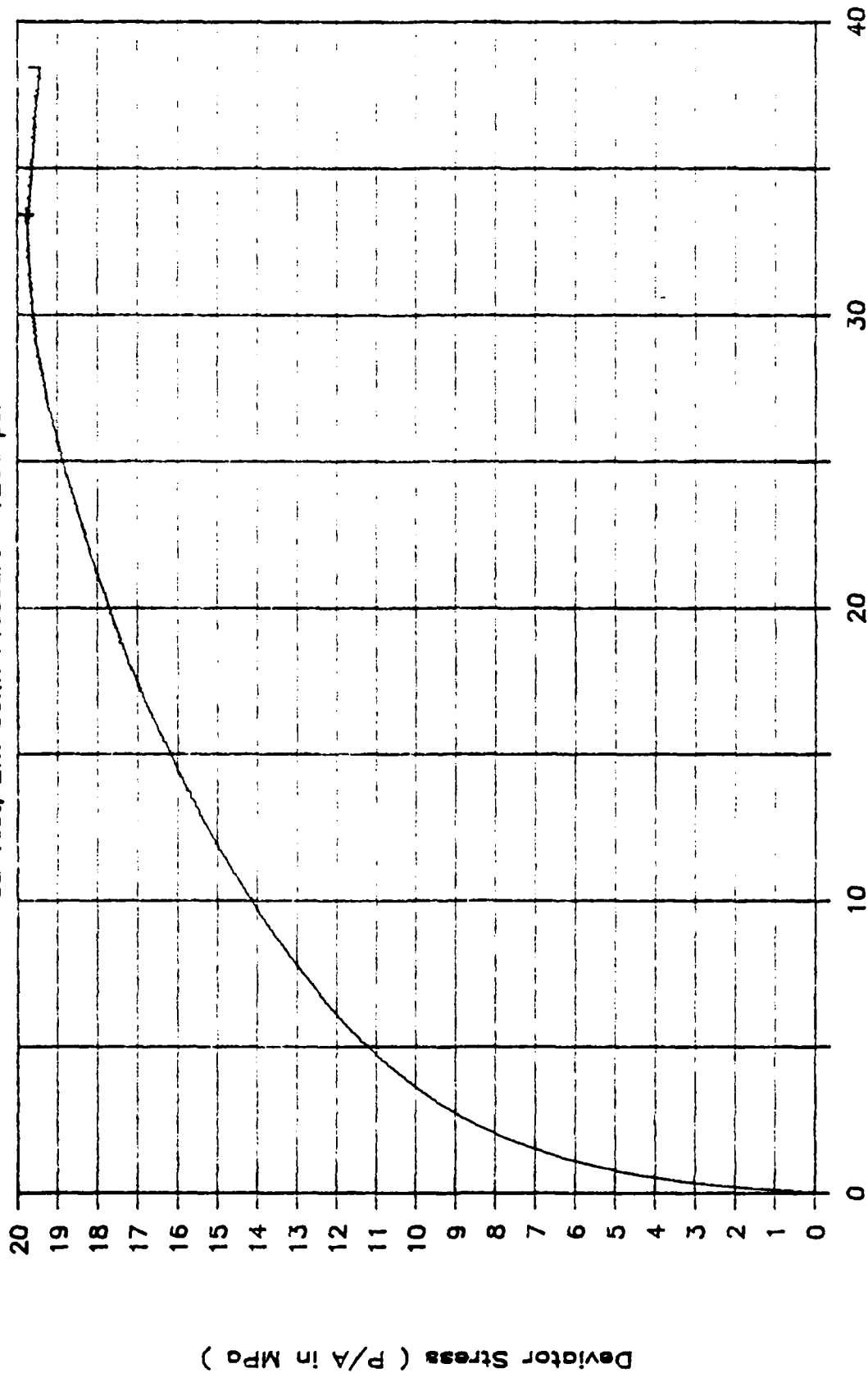


$$P = (S1+2S3)/3 \text{ in MPa (Test\#4)}$$

III.2 Effective Stress-Path for Drained Test on Cambria Sand.

Triaxial Compression of Cambria Sand

CD Test; Eff. Conf. Pressure = 1200 psi

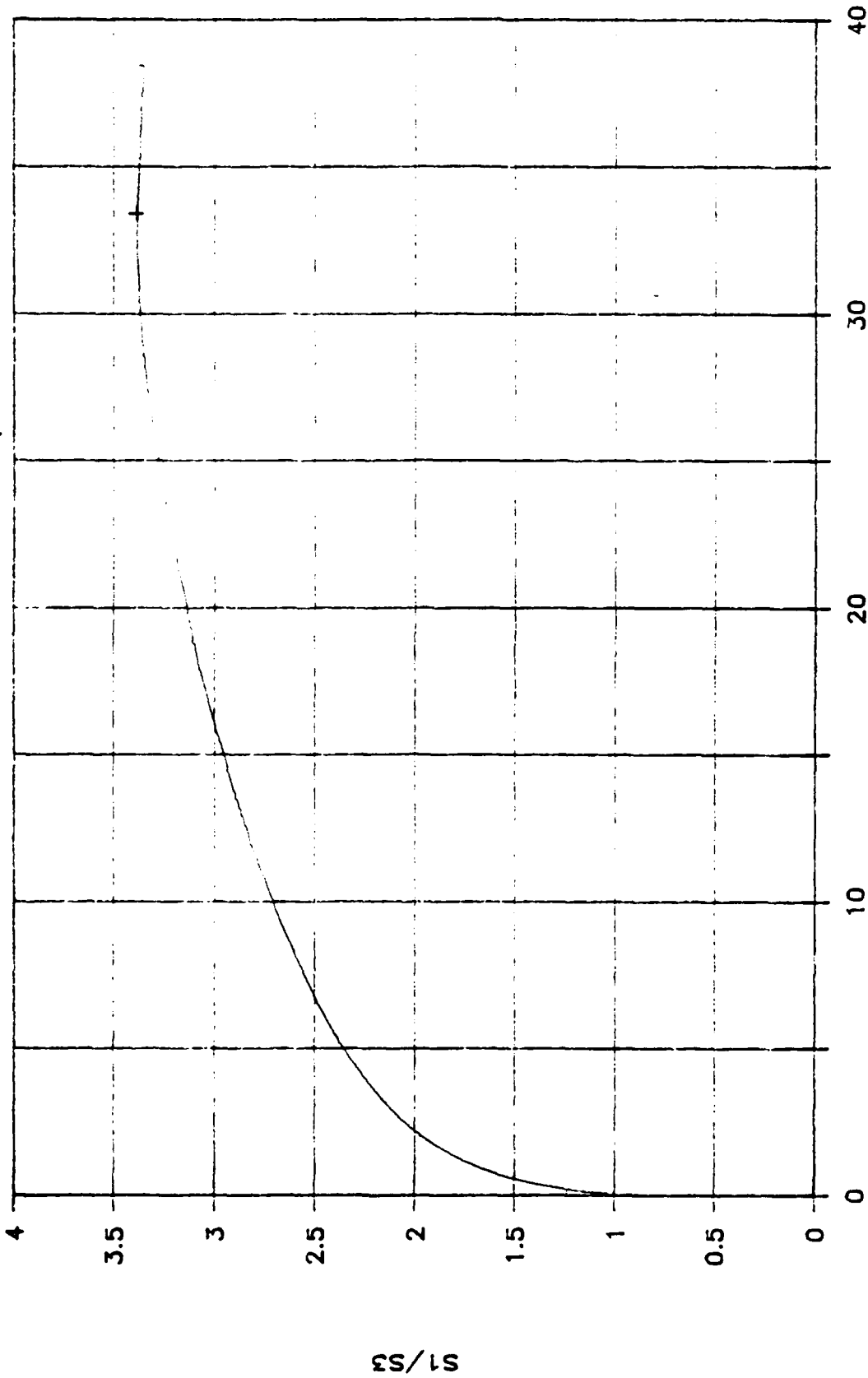


+ Axial Strain in % (Test#4)
max 19.79MPa @ 33.4%

III.3 Deviator Stress-Axial Strain Relation for Drained Test on Cambria Sand.

Triaxial Compression of Cambria Sand

CD Test; Eff. Conf. Pressure = 1200 psi

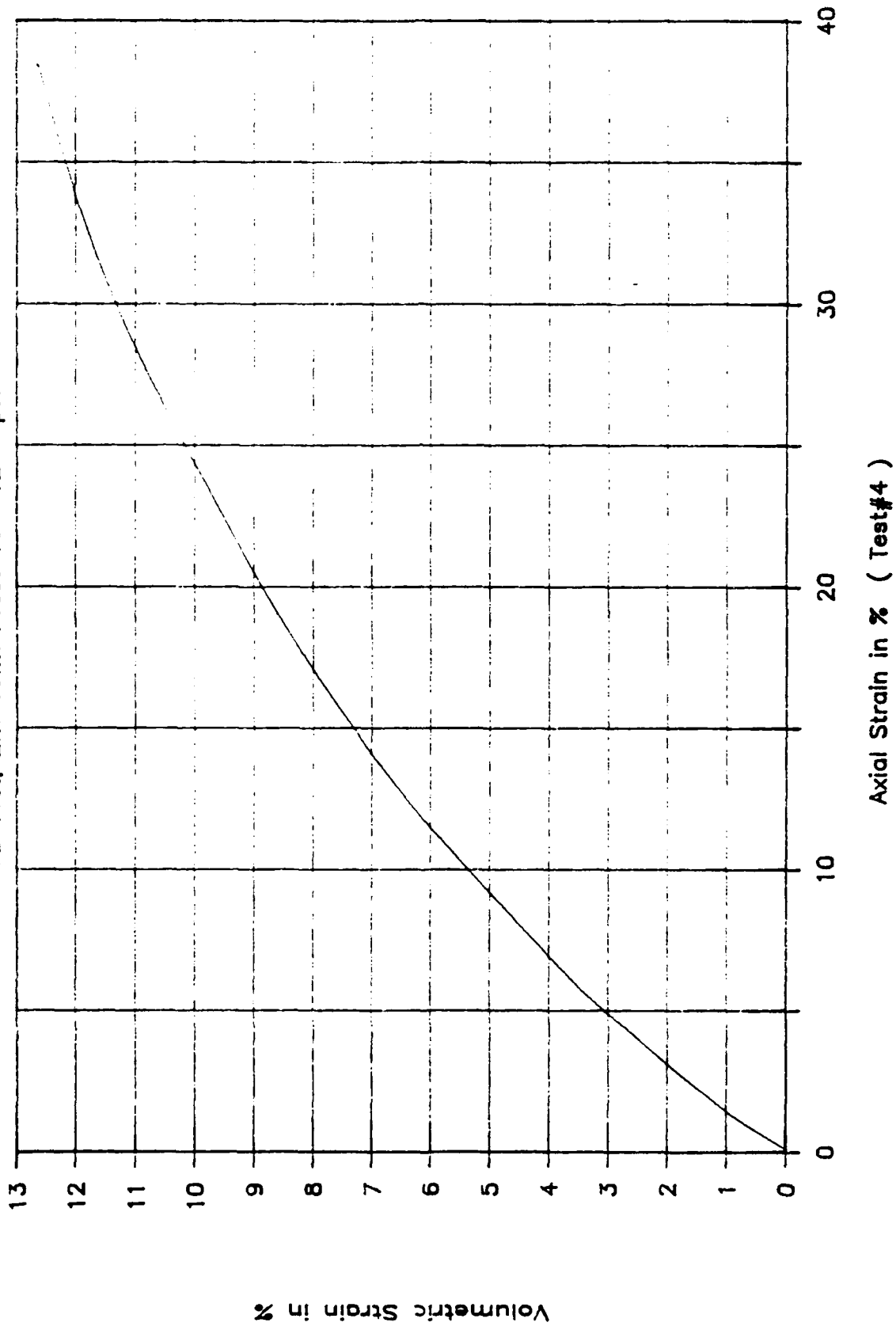


+ Axial Strain in % (Test #4)
 @ 33.38% S1/S3 = 3.39

III.4 Effective Stress Ratio-Axial Strain Relation for Drained Test on Cambria Sand.

Triaxial Compression of Cambria Sand

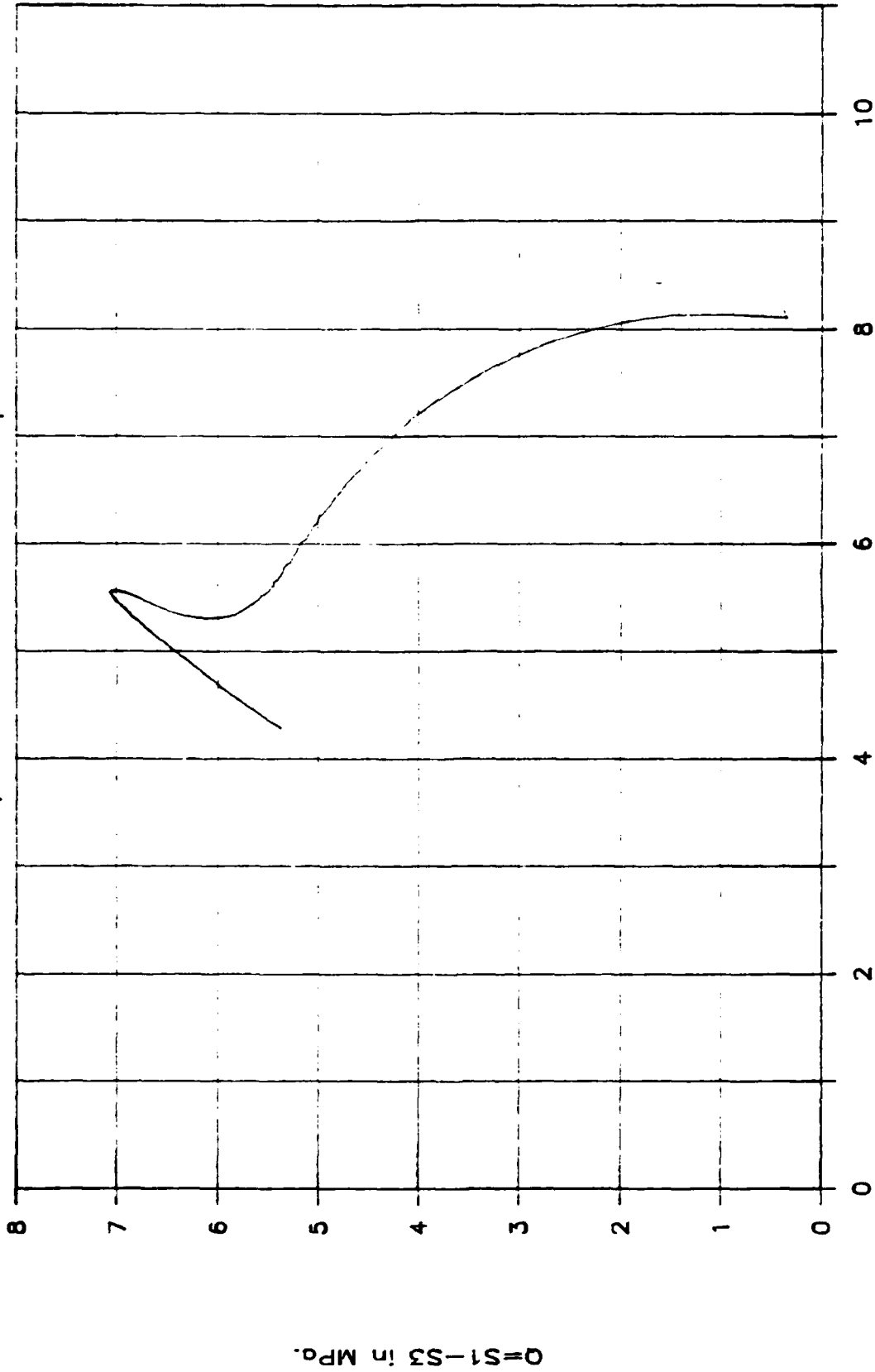
CD Test; Eff. Conf. Pressure = 1200 psi



III.5 Volume Change Variation in Drained Test on Cambria Sand.

Triaxial Compression of Cambria Sand

CU Test; Eff. Conf. Pressure = 1200 psi

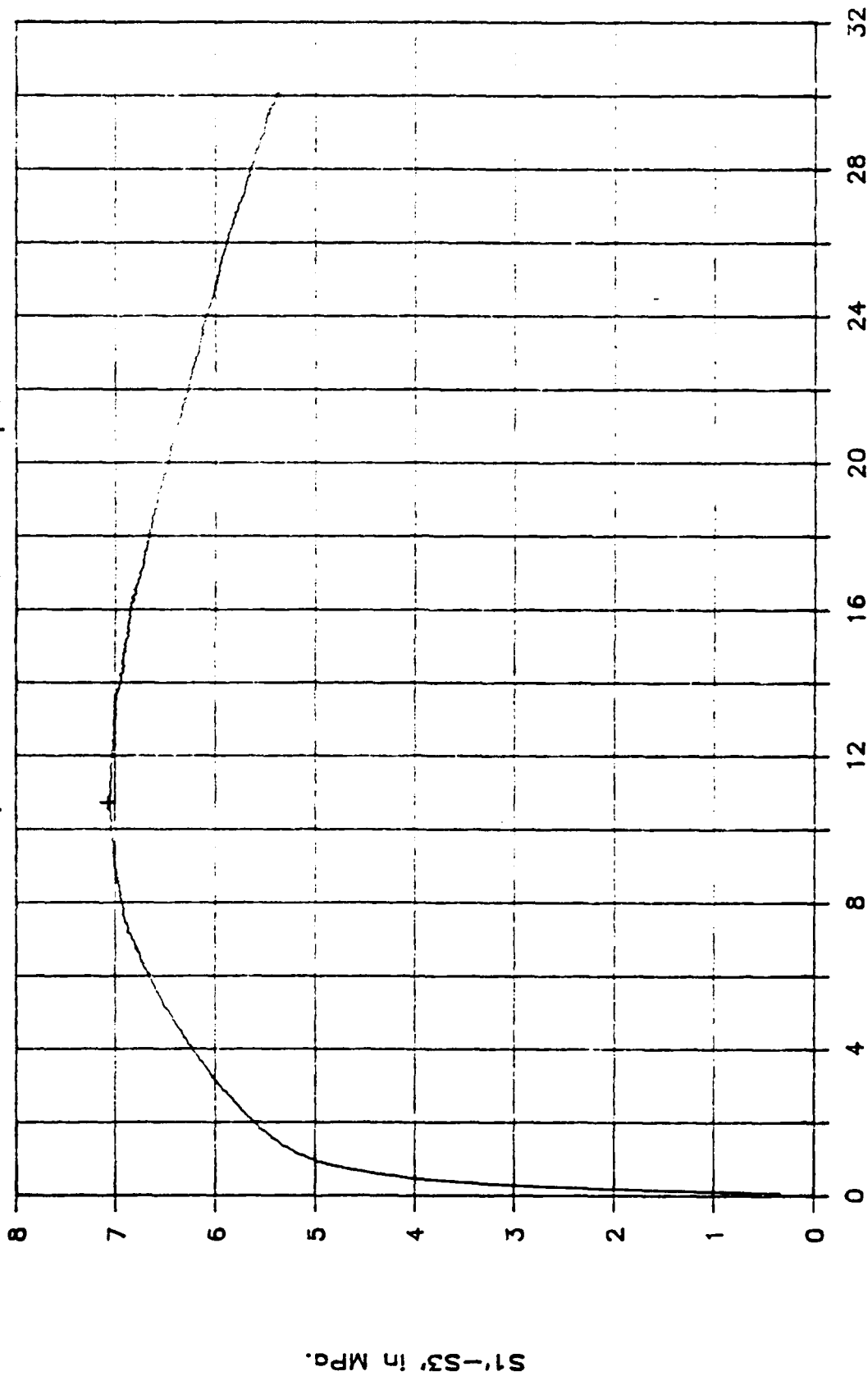


$P = (S1' + 2S3') / 3$ in MPa. ; Test #3

III.6 Effective Stress-Path in p' - q Undrained Test on Cambria Sand.

Triaxial Compression of Cambria Sand

CU Test; Eff. Conf. Pressure = 1200 psi

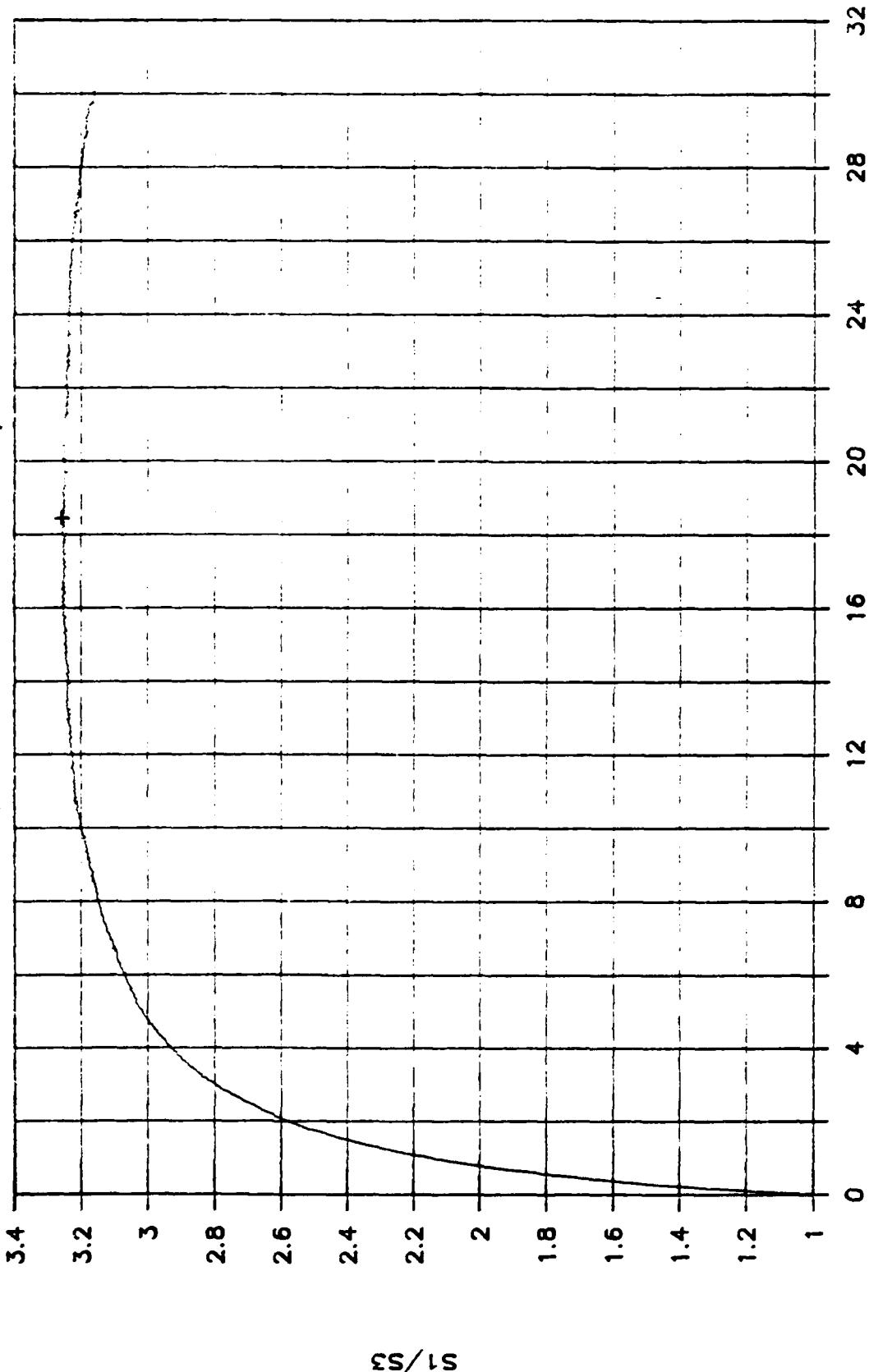


+ Axial Strain in % (Test#3)
 max(10.75%, 7.08MPa)

III.7 Deviator Stress-Axial Strain Relation for Undrained Test on Cambria Sand.

Triaxial Compression of Cambria Sand

CU Test; Eff. Conf. Pressure = 1200 psi

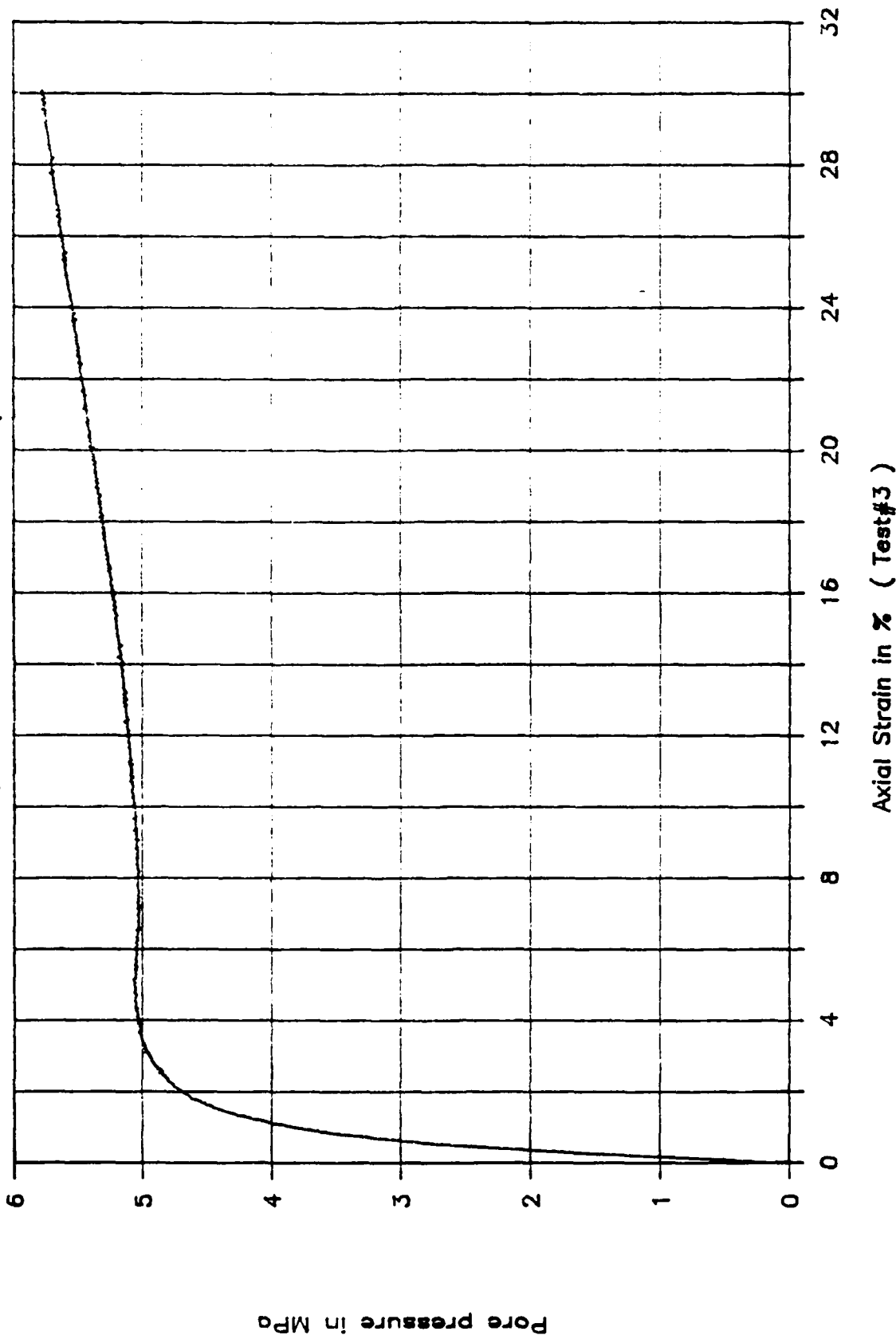


+ Axial Strain in % (Test#3)
 ○ 18.44% S1/S3=3.26

III.8 Effective Stress Ratio Variation in Undrained Test on Cambria Sand.

Triaxial Compression of Cambria Sand

CU Test; Eff. Conf. Pressure = 1200 psi



III.9 Pore Pressure Variation in Undrained Test on Cambria Sand.

IV. REFERENCES

1. Nelson, R.B., Wagner, M.H., and Ito, Y.M., "Materials Models and Numerical Calculations in Support of Ground Shock Predictions." *Response of Geological Materials to Blast Loading and Impact*, John C. Cizek, Ed., AMD, Vol. 69, American Society of Mechanical Engineers, New York, N.Y., 1985, pp. 1-26.
2. Nelson, I., Baron, M.L., and Sandler, I., "Mathematical Models for Geological Materials for Wave Propagation Studies," *Shock Waves and the Mechanical Properties of Solids*, Syracuse University Press, Syracuse, N.Y., 1971, Chapter 13, pp. 289-351.
3. Lade, P.V., and Nelson, R.B., "Incrementalization Procedure of Elasto-Plastic Constitutive Model with Multiple, Intersecting Yield Surfaces," *International Journal of Numerical and Analytical Methods in Geomechanics*, Vol. 8, 1984, pp. 311-323.
4. DiMaggio, F.L., and Sandler, I.S., "Materials Model for Granular Soils," *Journal of the Engineering Mechanics Division*, ASCE, Vol. 97, June 1971, pp. 935-950.
5. Sandler, I.S., DiMaggio, F.L., and Baladi G.Y., "Generalized Cap Model for Geological Materials," July 1976. *Journal of the Geotechnical Engineering Division*, ASCE, Vol. 102, No. GT7, Proc. Paper 12243, pp. 683-699.
6. Wright, J.P., Baron, M.L., and Nelson, I., "Air Induced Ground Shock Effects on Alluvium-Playa Material," Paul Weidlinger, Consulting Engineer, Defense Atomic Support Agency, July 1968.
7. Lade, P.V., "Elasto-Plastic Stress Strain Theory for Cohesionless Soil with Curved Yield Surfaces," *International Journal of Solids and Structures*, Vol. 13, Nov. 1977, pp. 1019-1035.

8. Hara, G., "Theorie der Akustischen Schwingungsansbreitung in gekorneten Substanzen und experimentelle Untersuchungen an Kohlepulver," *Elektrische Nachrichten-Technik* 12, pp. 191-200 (1935).
9. Gassman, F., "Elastic Waves Through a Packing of Spheres," *Geophysics* 16, pp. 673-685 (1951).
10. Brandt, H., "A Study of the Speed of Sound in Porous Granular Media," *J. of Appl. Mech.*, Vol. 22, pp. 479-485 (1955).
11. Mindlin, R.D., "Mechanics of Granular Media," Proc. Second U.S. Nat. Cong. Appl. Mech., Ann Arbor, pp. 13-20 (1954).
12. Mindlin, R.D., and Deresiewicz, H., "Elastic Spheres in Contact Under Varying Oblique Forces," *J. Appl. Mech.*, Vol. 20, pp. 327-344 (1953).
13. Verruijt, A., and De Josselin de Jong, G., "Etude Photoelastique d'un Empilement de Disques," *Cah. grpe Fr. Rheologie* 2- pp. 73-86 (1969).
14. Oda, M., and Konishi, J., "Microscopic Deformation Mechanism of Granular Materials in Simple Shear," *Soil and Foundations*, Vol. 14, No. 4, pp. 25-38 (1974).
15. Biarez, J., "Contribution a l'Etude des Proprietes Mecaniques des Sols et des Materiaux Pulverulents," These de Doctorat es Sciences - Grenoble, France (1962).
16. Wiendieck, K., "L'anisotropie des Milieux Prilverulants et son Influence sur les Tassements," These Docteur Ingenieur - Grenoble, France (1964).
17. Matsuoka, H., "A Microscopic Study on Shear Mechanism of Granular Materials," *Soils and Foundations*, Vol. 14, No. 1, pp. 29-43 (1974).

18. Oda, M., Nemat Nasser, S., and Mehrabadi, M., "A Statistical Study of Fabric in a Random Assembly of Spherical Granules", *Int. Journal of Num. and Anal. Methods in Geomechanics*, Vol. 6, pp. 77-94 (1982).
19. Chapuis, R.B., "De la Structure des Milieux Granulaires en Relation avec leur Comportement Mecanique," These de Doctorat es Sciences - Montreal, Canada (1976).
20. Christofferson, J., Mehrabadi, M., and Nemat Nasser, S., "A Micromechanical Description of Granular Materials Behavior," *J. of Appl. Mech.*, Vol. 48, pp. 339-344 (1981).
21. Cambou, B., "Orientational Distributions of Contact Forces as Memory Parameters in a Granular Material," Symposium on Deformation and Failure of Granular Materials, Ed. Vermar, PA, and Luger, H.J. Delft pp. 3-12 (1982).
22. Matsuoka, H., "A Stress-Strain Model for Granular Materials Considering the Mechanism of Fabric Change," *Mechanics of Granular Materials: New Models and Constitutive Relations*, Edited by Jenkins, J.T. and Satake, M., pp. 99-115 (1983).
23. Massal, R.J., "Stochastic Processes in the Grain Skelton of Soils," Proc. 6th ICSMFE, Vol. 1, Div. 1-2, pp. 303-307 (1965).
24. Kitamura, R., "A Mechanical Model of Particulate Material Based on a Stochastic Process," *Soils and Foundations*, Vol. 21, No. 2, pp. 63-72 (1981).
25. Chikwendu, S.C., "Probabilistic Stresses in Granular Media," Proc. Abs. 19th SESI Conf., Rolla, MO, pp. 309-317 (1982).
26. Ogawa, S., Omemura, A., and Oshihira, N., "On the Equations of Fully Fluidized Granular Materials," *ZAMP*, Vol. 31, pp. 483-493 (1980).
27. Savage, S.B., and Jeffry, D.J., "The Stress Tensor in a Granular Flow," *J. Fluid Mech.*,

Vol. 110, pp. 255-272 (1982).

28. Serrano, A.A., and Rodriguez-Ortiz, J.M. "A Contribution to the Mechanics of Heterogeneous Granular Media," Proc. Symp. Plasticity and Soil Mech., Cambridge (1973).
29. Cundall, P.A., "A Computer Model for Rock-Mass Behavior Using Interactive Graphics for the Input and Output of Geometrical Data," Report MRD-2-74, Missouri River Division, US Army Corps of Engineers, (1974).
30. Cundall, A.A., and Strack, O.D., "A Discrete Numerical Model for Granular Assemblies," *Geotechnique*, Vol. 29, No. 1, pp. 47-65 (1979).
31. Zubelewicz A., and Bazant, Z.P., "Interface Element Modeling of Fracture in Aggregate Composites," *Journal of Engineering Mechanics, ASCE*, Vol. 113, No. 11 (1987).
32. Ito, Y.M., Nelson, R.B., and Burks, D.E., "Numerical Method for Rock Rubble Fortification Analysis," DNA 58679F, Defense Nuclear Agency, Washington, D.C., (1981).
33. Nelson, R.B., Ito, Y.M., Burks, D.E., and Muki, Y., "Numerical Analysis of Projectile Penetration into Boulder Screens," CRT 5410F, California Research and Technology, Inc., Chatsworth, CA, April (1982).
34. Nelson, R.B., Ito, Y.M., Burks, D.E., and Muki, Y., "Numerical Analysis of Projectile Penetration into Boulder Screens, II" CRT 5420F, California Research and Technology, Inc., Chatsworth, CA, December (1982).
35. Mandel, J., "Conditions de Stabilité et Postulat de Drucker," Symposium de Rheologie et Mécanique des sols, Springer, Grenoble (1964).
36. Maini, T., Cundall, P., Marti, J., Beresford, P., Last, N., and Asgian, M., "Computer

Modelling of Jointed Rock Masses", U.S. Army Engineer Waterways Experiment Station, Technical Report N-78-4, August 1978.

37. Roddy, D.J., Schuster, S.H., Grant, L.B., and Kreyenhagen, K., "Computer Simulations of Large Asteroid Impacts Into Oceanic and Continental Sites ... Preliminary results on Atmospheric, Cratering, and Ejecta Dynamics," California Research and Technology, Chatsworth, California, 1986.